Title

Noninvasive Pressure Gradient Measurement in the Coronary Arteries using Phase Contrast Magnetic Resonance Imaging

Author

Deng, Zixin

Publication Date

2017

Peer reviewed|Thesis/dissertation

UNIVERSITY OF CALIFORNIA

Los Angeles

Noninvasive Pressure Gradient Measurement in the Coronary Arteries using Phase Contrast Magnetic Resonance Imaging

A dissertation submitted in partial satisfaction of the requirements for the degree Doctor of Philosophy in Bioengineering

by

Zixin Deng

2017

ABSTRACT OF THE DISSERTATION

Noninvasive Pressure Gradient Measurement

in the Coronary Arteries using

Phase Contrast Magnetic Resonance Imaging

by

Zixin Deng

Doctor of Philosophy in Bioengineering

University of California, Los Angeles, 2017

Professor Debiao Li, Chair

Heart Disease, including Coronary Artery Disease, Hypertension, and Stroke, is the number one cause of death in the United States. Coronary artery disease (CAD) or ischemic heart disease (IHD) kills over 360,000 people per year, make up for 1 in 7 deaths in the United States. In current clinical diagnosis and management of patients with suspected CAD, various noninvasive methods including personal history, stress electrocardiogram (ECG) tests, and advanced imaging techniques are normally performed in patients with intermediate risk of CAD. If any combination of the noninvasive results suggests high-risk coronary lesion(s), the patient is then suggested to undergo invasive catheterization where invasive coronary angiography (ICA)

and/or fractional flow reserve (FFR) or instantaneous wave-free ratio (iFR) are performed as the final steps of a diagnostic work-up.

Studies have shown that over 50% of patients who undergo invasive catheterization were found to have non-obstructive (<50% degree stenosis) or functionally nonsignificant (FFR > 0.80) coronary lesions, resulting in unnecessary invasive procedures. This suggests that better noninvasive methods are needed to help increase the diagnostic yield for invasive catheterization. An emerging noninvasive technique based on coronary computed tomographic angiography (CTA) in combination with computational fluid dynamics simulations to measure the functional significance of a coronary lesion, FFR_{CT}, has shown promise. However, the method requires exposure to ionizing radiation, uses an anatomical model to simulate the hemodynamic behaviors in the coronary arteries, and may be hindered by blooming artifacts caused by densely calcified plaques which could reduce the accuracy of the overall technique.

This dissertation introduces the development of a magnetic resonance (MR) based noninvasive functional assessment for the diagnosis and management of stable CAD. The developed noninvasive technique mimics the invasive FFR and iFR methods to calculate an index using pressure. The proposed noninvasive pressure measurement framework utilizes flow velocity information obtained using phase-contrast magnetic resonance imaging (PC-MRI) in conjunction with the Navier-Stokes (NS) analysis to derive a pressure gradient across the coronary lesion of interest. Validation studies of PC-MRI velocity measurements and NS derived pressure gradient measurements were assessed in a small-caliber stenotic flow phantom at different degrees of narrowing, in healthy coronary arteries, and in a pilot patient study with diseased coronary arteries. In patient studies, noninvasive pressure gradient measurements were compared with invasive FFR and iFR to evaluate the potential of the proposed method for

noninvasive functional assessment in patients with stable CAD. In addition, the method was further improved using a stack-of-stars MR acquisition approach with compressed sensing image reconstruction to allow for shorter scan time, compared to Cartesian acquisition. The approach was tested in phantoms and healthy volunteers to assess feasibility.

The success of the proposed noninvasive pressure gradient measurement method discussed in this dissertation may serve as a complementary approach to current clinical diagnostic tools, providing added information to better risk-stratify and manage patients with stable CAD. In addition, the method has the potential to serve as a gatekeeper for patients who are unlikely to benefit from invasive catheterization, hence, decrease the number of unnecessary invasive procedures.

The dissertation of Zixin Deng is approved.

Daniel B. Ennis

Peng Hu

Michael Albert Thomas

Zhaoyang Fan

Debiao Li, Committee Chair

University of California, Los Angeles

2017

Dedicated to my mother

TABLE OF CONTENTS

LIST OF ABBREVIATIONS

General

T – Tesla

mT – militesla

m – meter

Statistics

ICC – intra-class correlation coefficient

r – inter-class correlation coefficient or Pearson correlation coefficient

p – statistical significance coefficient

Medicine

CVD – cardiovascular disease

CAD - coronary artery disease

IHD – ischemic heart disease

LAD - left anterior descending coronary artery

pLAD – proximal left anterior descending coronary artery

mLAD – middle left anterior descending coronary artery

dLAD – distal left anterior descending coronary artery

LM – left main coronary artery

RCA - right coronary artery

ICA - invasive coronary angiography

CFR - coronary flow reserve

FFR - fractional flow reserve

iFR - instantaneous wave-free ratio

CTA - computed tomography angiography

PET – positron emission tomography

SPECT – single-photon emission computed tomography

ECG – echocardiography

HR – heart rate

BMP – beats per minute

BMI – body mass index

General Magnetic Resonance Imaging

MRI – magnetic resonance imaging

2D/3D – two/three dimensions

FOV – filed-of-view

TE – echo time

TR – repetition time

Cardiac Magnetic Resonance Imaging

CMR - cardiac magnetic resonance

PC-MRI - Phase-contrast magnetic resonance imaging

MR-iFR - magnetic resonance instantaneous wave-free ratio

cMRA – coronary magnetic resonance angiography

VENC – velocity encoding

Vz – through-plane velocity in the z direction

Vx/Vy – in-plane velocity in the x / y directions

Others

ΔP – pressure gradient

NS – navier-stokes

Pa – arterial pressure

Pd – distal pressure

ROI – region-of-interest

CFD – computational fluid dynamics

CT-FFR – compute tomography derived fractional flow reserve

LIST OF FIGURES

LIST OF TABLES

ACKNOWLEDGEMENTS

Firstly, I would like to express my sincere gratitude to my mentor and advisor Dr. Debiao Li for his continuous support of my PhD study and research, for his motivation, guidance, encouragement, and immense knowledge. I could not have imagined having a better advisor and mentor.

Besides my advisor, I would also like to thank my thesis committee: Dr. Daniel B. Ennis, Dr. Peng Hu, Dr. Albert Thomas, and Dr. Zhaoyang Fan for their insightful suggestions, guidance, and encouragement, which helped widen my research from various perspectives.

I would also like to thank my mentor Dr. Zhaoyang Fan for his patience and guidance throughout the years.

My sincere thanks also go to our onsite Siemens scientists for all their help and support, Dr. Xiaoming Bi, Dr. Yutaka Natsuaki, and Dr. Gerhard Laub.

I would also like to give a special thank you to Dr. Daniel Berman and Dr. Saibal Kar for sharing their clinical knowledge and for their motivation and guidance.

I am grateful to all the collaborators that I have worked with at Yonsei University, University of California, Los Angeles, and Cedars-Sinai Medical Center. I would like to thank Dr. Hyuk-Jae Chang for the collaborative clinical studies that have made the evaluation of the initial clinical feasibility of this dissertation work possible. I would also like to thank Dr. Daniel Ennis and Dr. Michael Loecher for sharing their expertise on flow imaging and sharing the stack of stars flow sequence, which is the foundation of the coronary 4D flow work. In addition, I would like to thank Dr. Wensha Yang for her continuous guidance in my 4D abdominal imaging work for radiation therapy planning.

I would also like to thank the current and previous staff members at the Biomedical Imaging Research Institute: Laura Smith, Ed Gill, Lawrence St. John, Eileen Shinn, Maggie Huang,

Karen Gutierrez, Camille Rogacion-Labao, Rhona Littman, Christy Woo, Johanna Kim for all your help and support throughout the years.

I would like to thank the National Institute of Health for awarding me the F31 pre-doctoral fellowship to fund my research.

Special thanks also to my fellow graduate students, the postdocs, and the project scientists for making graduate life and conference trips exciting: Christopher Nguyen, Zhengwei Zhou, Jaime Shaw, Yibin Xie, Randy Yang, Anthony Christodoulou, Jianing Pang, David Chen, and Yuhua Chen. In addition, for their work on contributing to the thoughts and ideas presented in *Chapters 3-6*.

I would also like to thank my 2016-2017 engineering graduate student association (eGSA) family for making my last year at UCLA memorable.

In addition, I would like to thank my KQVZ family (K. C., Q. H., and V. C.), L.P.C., K.M., A.K., MG. S., B.V., M.C., and S.H. for your continuous encouragement and friendship throughout the years.

Furthermore, I would like to thank D. C. for your moral support and motivation, and making my boring weekends fun.

Last but not the least, I would like to thank everyone in my family for your unconditional love throughout my graduate studies and my life in general.

VITA

EDUCATION

University of California, Los Angeles
Doctoral Candidate in Biomedical Engineering — 2017

University of California, Irvine
Bachelor of Science in Biomedical Engineering — 2012

AWARDS

F31 Pre-doctoral Fellowship
National Institute of Health (NIH) — 2016–2018

RESEARCH EXPERIENCES

UCLA, Department of Bioengineering & — 2012 – Present
Cedars-Sinai Medical Center, Biomedical Imaging Research Institute
Graduate Student Researcher – Professor Debiao Li's lab

UCI, Department of Biomedical Engineering — 2010 – 2012
Undergraduate Researcher – Professor Gultekin Gulsen's lab

OTHER EXPERIENCES

UCLA, Engineering Graduate Student Association (eGSA)
President — 2016 – 2017
Professional Development Director — 2015 – 2016

MANUSCRIPT PUBLICATIONS

1. **Deng Z**, Loecher M, Nguyen C, Christodoulou A.G, Zhou Z, Shaw J.L, Xie Y, Bi X, Fan Z, Ennis D.B, Li D, Coronary 4D-Flow MRI using Stack-of-Stars Acquisition: towards noninvasive pressure gradient measurement in the coronary arteries, {in preparation}.
2. **Deng Z*,** Lee SE*, Xie Y, Nguyen CT, Bi X, Zhou Z, Shaw JL, Yang Q, Choi BW, Kim JS, Berman DS, Li D, Chang, HJ, Noninvasive Functional Evaluation of Coronary Stenosis using MR Instantaneous wave-Free Ratio (MR-iFR): Initial Patient Study, {submitted}.
3. **Deng Z**, Yang W, Pang J, Bi X, Tuli R, Li D, Fan Z, Improved vessel-tissue contrast and image quality in 3D radial sampling-based 4D-MRI, *Journal of Applied Clinical Medical Physics*, 2017, DOI: 10.1002/acm2.12194
4. **Deng Z,** Fan Z, Lee S, Nguyen C, Yang Q, Bi X, Choi BW, Kim JS, Berman D, Chang HJ, Li D, Noninvasive Measurement of Pressure Gradient Across a Coronary Stenosis Using Phase Contrast (PC)-MRI: A Feasibility Study, *Magnetic resonance in medicine* 77.2 (2017): 529-537.
5. Xie, Y., Kim, Y.J., Pang, J., Kim, J.S., Yang, Q., Wei, J., Nguyen, C.T., **Deng, Z.**, Choi, B.W., Fan, Z. and Merz, C.N.B., 2017. Coronary Atherosclerosis T1-Weighed Characterization with Integrated Anatomical Reference: Comparison With High-Risk Plaque Features Detected by Invasive Coronary Imaging. *JACC: Cardiovascular Imaging*, *10*.6 (2017), 637-648.
6. Yang Q*, **Deng Z***, Bi X, Song S, Schlick K, Gonzalez N, Li D, Fan Z, Intracranial Vessel Wall MRI: A Parameter Tune-up Solution to Improve the Scan Efficiency 3D Variable-Flip-Angle Turbo Spin-Echo. *Journal of Magnetic Resonance Imaging (2017)*. Doi:10.1002/jmri.25611
7. Fan, Z, Yang Q, **Deng Z**, Li Y, Bi X, Song S, Li D, "Whole-brain intracranial vessel wall imaging at 3 Tesla using cerebrospinal fluid–attenuated T1-weighted 3D turbo spin echo." *Magnetic resonance in medicine* 77.3 (2017): 1142-1150.

8. Jin, J., McKenzie, E., Fan, Z., Tuli, R., **Deng, Z**., Pang, J., Fraass, B., Li, D., Sandler, H., Yang, G. and Sheng, K., Guo S., Yang W., Nonlocal means Denoising of self-gated and k-space sorted 4-dimensional magnetic resonance imaging using block-matching and 3-dimensional filtering: implications for pancreatic tumor registration and segmentation. *International Journal of Radiation Oncology* Biology* Physics*, *95*(3) (2016), pp.1058-1066.
9. **Deng Z*,** Pang J*, Yang W, Yue Y, Sharif B, Tuli R, Li D, Fraass B, and Fan Z, 4D MRI Using 3D Radial Sampling with Respiratory Self-Gating to Characterize Temporal Phase-Resolved Respiratory Motion in the Abdomen. *Magnetic Resonance in Medicine,* 75.4 (2016): 1574
10. Yang W, Fan Z, Tuli R, **Deng Z**, Pang J, Wachsman A, Reznik R, Sandler H, Li D, Fraass B, Four-dimensional Magnetic Resonance Imaging with 3D Radial Sampling and Self-gating based K-space Sorting: Early Clinical Experience on Pancreatic Cancer Patients, *International Journal of Radiation Oncology*Biology*Physics,* 93.5 (2015): 1136-1143.
11. Yong Y, Fan Z, Yang W, Pang J, **Deng Z**, McKenzie E, Tuli R, Wallace R, Li D, Fraass B, Geometric Validation of Self-gating k-Space-sorted 4D-MRI vs. 4D-CT Using a Respiratory Motion Phantom, *Medical Physics* 42.10 (2015): 5787-5797.

*co-first authors

SELECTED CONFERENCE ABSTRACTS

1. **Deng Z**, Christodoulou A, Yang W, Bi X, Shaw J, Fraass B, Tuli R, Li D, Fan Z, T2-Weighted 4D-MRI using an Isotropic 3D Data Acquisition and Retrospective K-Space Binning, *59th Annual Meeting & Exhibition of the American Association of Physicists in Medicine (AAPM, MRI session, Oral Presentation) TU-D-601-6 (2017)*
2. **Deng Z**, Lee S, Fan Z, Nguyen C, Xie Y, Pang J, Bi X, Yang Q, Choi B.W, Kim J.S, Berman D, Chang H.J., Li D, Noninvasive functional evaluation of coronary stenosis using MR instantaneous wave-free ratio (MR-iFR): initial patient study, *Society of Cardiovascular Magnetic Resonance (SCMR) 20th annual conference, Early Career Award: clinical session candidate, oral presentation, 2017*.
3. **Deng Z**, Lee S, Fan Z, Nguyen C, Cho I, Yang Q, Bi X, Choi BW, Kim JS, Berman D, Chang HJ, Li D, Pressure Gradient Measurement in the Coronary Artery Using Phase Contrast (PC)-MRI: Initial Patient Results Towards Noninvasive Quantification of Fractional Flow Reserve, *International Society of Magnetic Resonance in Medicine (ISMRM) 24th annual conference, Oral presentation in Velocity & Flow Quantification Scientific Session*.
4. **Deng Z**, Yang Q, Bi X, Fan Z, and Li D, Reproducibility of Phase-Contrast MRI in the Coronary Artery: Towards Noninvasive Pressure Gradient Measurement and Quantification of Fractional Flow Reserve. *International Society of Magnetic Resonance in Medicine (ISMRM, Let it Flow session, Oral)* (June 2015)
5. **Deng Z**, Fan Z, Xie G, He Y, Yang Q, Natsuaki Y, Jin N, Bi X, Li K, Fan Z, Zhang Z, and Li D, Pressure Gradient Measurement in the Coronary Artery Using 4D PC-MRI: Towards Noninvasive Quantification of Fractional Flow Reserve. *Journal of Cardiovascular Magnetic Resonance (17th Annual SCMR Scientific Sessions, oral)* 16, O55 (2014).

PATENT

Fan, Z., Pang, J., **Deng, Z**. and Li, D., Cedars-Sinai Medical Center, 2015. Characterization of respiratory motion in the abdomen using a 4d mri technique with 3d radial sampling and respiratory self-gating. U.S. Patent Application 14/707,647.

CHAPTER 1 – Dissertation Motivation

1.1 Clinical significance

Cardiovascular disease (CVD) is the most common underlying cause of death, accounts for approximately 1 of every 3 deaths in the United States (US). It is estimated that roughly every 40 seconds, 1 American die of CVD. One category of CVD, coronary heart disease (CHD), known as coronary artery disease (CAD) or ischemic heart disease (IHD), is the leading cause of CVD related deaths, contributing to 45.1% or 1 in 7 deaths in the US (1,2). Patients with CAD may be asymptomatic or symptomatic and can present with stable angina pectoris (chest pain during exertion), unstable angina pectoris (unexpected chest pain at rest), or Myocardial Infarction (MI, or heart attack). In approximately 50% of CAD patients, angina pectoris is the initial manifestation of CAD (3). It has been estimated that there are approximately 30 patients with stable angina for every patient hospitalized with MI (4).

1.2 Current patient management

Current clinical diagnosis and management of patients with suspected CAD utilizes a variety of noninvasive and invasive methods to assess for possible lesions in the coronary vessels and damages in the heart muscle (myocardium). For patients with stable conditions, guidelines recommend continuous monitoring in patients with low risk of CAD, noninvasive testing for patients with intermediate risk, and direct referral for invasive catheterization for patients with high risk (3-6).

Initial noninvasive methods include personal history, physical exams and functional or stress testing (electrocardiogram, ECG, changes), followed by imaging techniques such as single

photon emission computed tomography (SPECT) or positron emission tomography (PET), stress and rest echocardiography, or cardiac magnetic resonance (CMR) to assess myocardial perfusion defects or wall motion abnormalities. In addition, coronary computed tomography angiography (CTA) is also used to help detect the degree of coronary stenosis. If any combination of the noninvasive results suggest the patient has high-risk coronary lesion(s) in need of coronary revascularization, patient is then recommended for further diagnosis via invasive catheterization including invasive coronary angiography (ICA) and/or fractional flow reserve (FFR), else patient is recommended for medical therapy (4).

ICA is mostly used in the final steps of a diagnostic work-up in patients with suspected CAD with FFR as an emerging method to evaluate the patient's need for coronary revascularization (4,7). ICA is an anatomical diagnostic tool to visualize the degree of stenosis and FFR is a functional diagnostic tool to determine ischemia inducing coronary lesions based on pressure measurements across a coronary stenosis (8). For patients undergoing invasive cardiac catheterization, based on the American Heart Association (AHA) guidelines, a "significant" stenosis is defined as ≥ 70% diameter narrowing (≥ 50% for left main CAD) reported by ICA and/or a FFR index of ≤ 0.80. A recently developed invasive diagnostic method, similar to FFR, termed instantaneous wave-free ratio (iFR), has shown to be non-inferior to FFR as a guide for coronary revascularization (9,10). Although the technique is not yet included in the guidelines, an iFR cut-off of 0.89 has shown to be as good as a FFR cut-off of 0.80, suggesting the use of iFR in the future as an alternative invasive approach to shorten procedure time and decrease patient discomfort. If a stenosis is considered significant based on a ICA, FFR, and/or iFR, patient then undergoes coronary revascularization treatment using methods such as percutaneous coronary intervention (PCI) or coronary artery bypass graft (CABG).

1.3 Challenges of current patient management

Accurate identification of patients with suspected CAD who should undergo either medical therapy or coronary revascularization is very important in the practice of cardiovascular medicine. In current clinical practice, noninvasive diagnostic methods are utilized to help identify the severity the coronary disease and used as a gatekeeper to limit the number of unnecessary invasive procedures. However, with current techniques, a low diagnostic yield of invasive catheterization was observed among patients with suspected CAD (11).

In patients who were assessed by ICA, according to a retrospective study based on data from the American College of Cardiology National Cardiovascular Data Registry between 2004 and 2008 by Patel et al., among 398,978 patients at 663 hospitals, only a little more than 33% of patients had obstructive (≥50% diameter stenosis) CAD (12). This means that more than 50% of patients had non-obstructive (<50% diameter stenosis) CAD and didn't need to undergo invasive catheterization. Further, when assessed by FFR, more than 50% of patients with ≥ 50% stenosis have normal FFR (>0.80) (13). Specifically, in the FFR versus angiography in multi-vessel evaluation (FAME) study, 65% of coronary lesions with angiography severity of 50% to 70% were found functionally nonsignificant (FFR > 0.80), suggesting that these patients could be deferred from invasive catheterization procedures.

An emerging noninvasive technique based on coronary CTA in combination with computation fluid dynamics (CFD) simulations to derive pressure changes across a coronary lesion, FFR_{CT}, has shown promise for the diagnosis of patients with stable CAD. Recent results showed that care guided by coronary CTA and selective FFR_{CT} has equivalent clinical outcome and quality of life, lower rate of ICA, and lower costs when compared to usual care (11,14,15). However, the method requires the exposure to ionizing radiation, uses an anatomical model to

simulate the hemodynamic behaviors in the coronary arteries, and may be hindered by blooming artifacts caused by densely calcified plaques which could reduce the accuracy of detection of coronary stenosis, a necessary component of FFR_{CT} assessment.

1.4 Aims

The overall aim of this dissertation is to develop a noninvasive pressure gradient measurement technique, termed MR-iFR, for the prediction of the functional significance of coronary stenosis using phase-contrast magnetic resonance imaging (PC-MRI). The method is essentially a surrogate to FFR or iFR, and has the advantage of being noninvasive and comprising of no ionizing radiation. The success of the technique may serve as a complementary approach to current clinical diagnostic tools, providing added information to better risk-stratify and management of patients with stable CAD.

1.4.1 Aim 1: To develop a noninvasive pressure gradient measurement framework using PC-MRI and validate its feasibility in stenotic phantoms, using pressure transducer measurements as reference.

Chapter 3 presents a noninvasive pressure gradient measurement framework using PC-MRI and Navier-Stokes (NS) analysis. This chapter explores the feasibility of pressure gradient quantification in conditions of flowing liquid through small diameters. Validation studies of PC-MRI velocity measurements and NS derived pressure gradient measurements in a small-caliber stenotic flow phantom at different degrees of narrowing, mimicking the scenario of a various degrees of diseased coronary arteries, will be described. In addition, correlation analysis between

PC-MRI derived pressure gradient measurement and gold standard pressure gradient measurement using a pressure transducer is further evaluated.

1.4.2 Aim 2: To translate the noninvasive pressure gradient measurement framework in vivo and validate its feasibility in healthy and diseased coronary arteries.

Chapter 4 presents a noninvasive pressure gradient measurement framework in vivo. This chapter describes the implementation of PC-MRI for coronary artery applications. Repeatability of the velocity measurements in the coronary arteries will be analyzed. Further, pressure gradient measurements in the healthy coronary arteries will be evaluated to assess the feasibility of the proposed method and compared to a small group of stable CAD patients.

1.4.3 Aim 3: To evaluate the feasibility of the noninvasive pressure gradient measurement framework in a cohort of stable CAD patients, using invasive FFR and iFR as references.

Chapter 5 presents the initial feasibility of the proposed noninvasive pressure gradient measurement framework in a pilot study consists of a group of stable CAD patients. A noninvasive physiological index, termed MR-iFR, is obtained using the proposed PC-MRI method and compared to gold standard invasive FFR and iFR indices. In addition, the chapter further discusses the potential of MR-iFR as a noninvasive diagnostic tool for patients with stable CAD.

1.4.4 Aim 4: To further improve coronary PC-MRI using a stack-of-stars acquisition with compressed sensing reconstruction and validate its feasibility in stenotic phantoms and healthy subjects, using Cartesian PC-MRI as reference.

Chapter 6 presents the initial feasibility of a four-dimensional (4D) PC-MRI method using golden-angle stack-of-stars acquisition with compressed sensing reconstruction. This chapter will further discuss the feasibility of the method for potential scan time reduction, using 4D Cartesian PC-MRI as reference. Various undersampling factors correlated to reduced scan times will be explored in stenotic phantoms at different degrees of narrowing, and healthy subjects, to determine a feasible scan time for image acquisition.

CHAPTER 2 - Background

2.1. The coronary circulation

2.1.1. Introduction

The cardiovascular system is one of the many systems in our body that plays a major role in maintaining our body in a stable internal environment. The system consists of the heart, blood vessels, and blood, which all work together to deliver oxygen, nutrients, cells and waste products to the appropriate parts of the human body. The most important component in this system is the heart, which serves as a pump that circulates oxygenated blood to the entire body and deoxygenated blood to the lungs. The heart is composed of different types of cardiac muscle through special mechanisms to maintain a continuous rhythm for efficient pumping. Like all tissues in the body, the heart itself also needs oxygenate blood to maintain its function. This is achieved by the coronary circulation where coronary vessels (arteries and veins) lie on the surface of the heart muscle (myocardium) to provide sufficient amount of blood to the myocardium to maintain normal cardiac function (16).

2.1.2. The coronary tree

Error! Reference source not found. represents the general coronary anatomy. The coronary arteries originate from the root of the aorta and are separated into two major branches, left and right, to supply blood to different parts of the myocardium. The main coronary vessels on the epicardial surface of the heart range from 4 mm to 400 μm in diameter and then branch into small arteries and arterioles (<400 μm) penetrating into the myocardium (17).

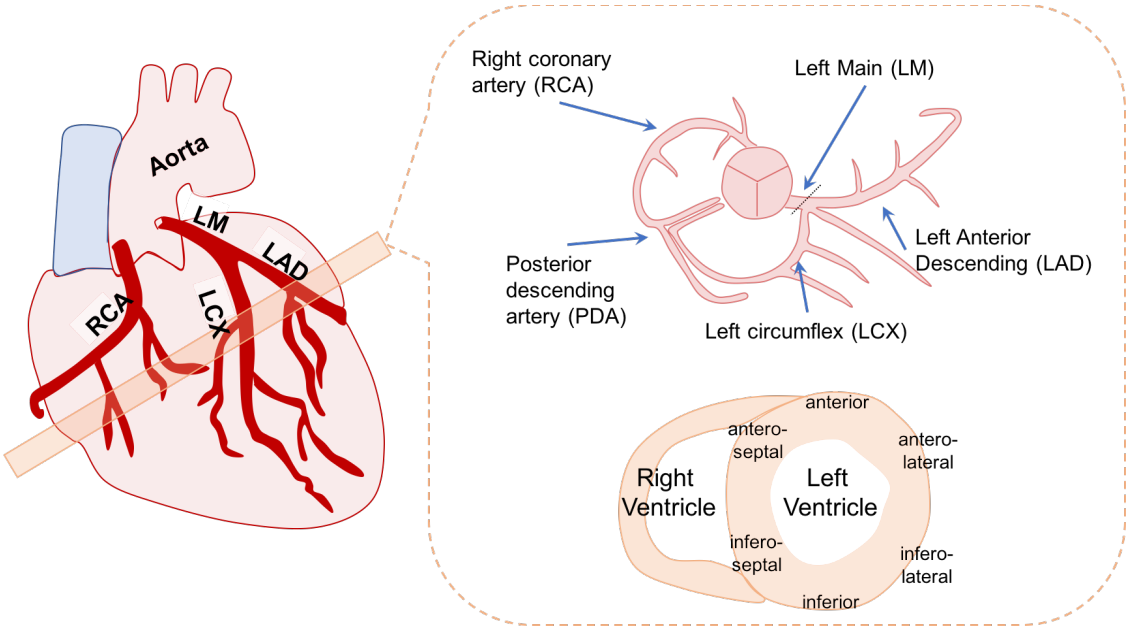

Figure 1. The coronary artery anatomy

Although coronary anatomy may differ depending on the individual, in general, for the epicardial vessels, the left coronary artery consists of the left main (LM), left anterior descending (LAD), and left circumflex (LCX) coronary arteries, supply blood primarily to the anterior and left lateral portions of the left ventricle; the right coronary artery supply blood primarily to the right ventricle and the posterior part of the left ventricle (12,13,16). **Figure 2** shows the general myocardium territory that's supplied by the different coronary vessels. In cases of coronary blockage due to build-up of plaque, the supply of blood to the appropriate myocardium territories may be decreased leading to insufficient oxygen supply to the myocardium and myocardial infarction or heart attack (*details are discussed in chapter 2.2*).

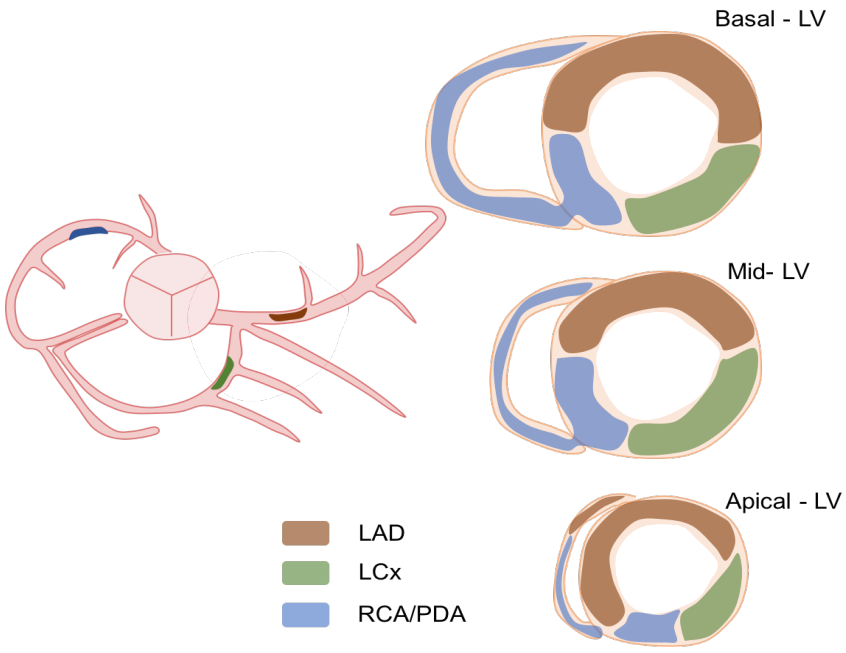

Figure 2. Myocardial perfusion territories in the basal, middle and apical slices of the left and right ventricles

2.1.3. Coronary blood flow

In contrast to the flow mechanics in other vessel locations, the arterial coronary blood flow is the highest during diastole and low during systole. On average, the resting coronary blood flow is around 225 mL/min and may increase 3-4 times during exercise to compensate for the increased oxygen demand in the myocardium and ensure that sufficient amount of nutrients is delivered. The increase in coronary flow is mostly achieved by vasodilation of the coronary vessels, mainly in the microvasculature (16,17). Eckenhoff et al. have shown in a previous study that cardiac oxygen consumption and coronary blood flow are linearly correlated and coronary blood flow adjusts itself to meet the demand of the heart for oxygen or the available supply in the arterial blood (18).

2.1.4. Coronary flow reserve

To assess if sufficient coronary blood flow is achieved to meet the myocardial metabolic demands, a concept of coronary flow reserve was introduced by Gould et al in 1974 (19). Coronary flow reserve is defined as the ratio of maximal hyperemic coronary blood flow to resting coronary blood flow. In healthy subjects, coronary blood flow could increase up to 4-6 folds from its resting conditions during exercise or pharmacological induced stress. In the presence of coronary stenosis, significant hyperemic flow reduction may occur depending on the level of stenosis measured (16,17,20). Based on Gould et al's study, during rest, coronary flow remained constant and did not decrease until approximately 80 to 85% reduction in coronary diameter, however, during stress, coronary flow progressively decreased starting from as small as 30% reduction in coronary diameter and a more severe decline was observed starting from 60 to 70% diameter stenosis (19). Current guidelines based on the American Heart Association (AHA) have suggested that a "significant" coronary stenosis is defined as ≥ 50% diameter narrowing for left main coronary artery and ≥ 70% diameter narrowing for other coronary vessels when assessed anatomically (4).

The assessment of the hemodynamics of a coronary stenosis or the assessment of coronary flow reserve could be classified into three types: 1) absolute flow reserve, 2) relative flow reserve, and 3) fractional flow reserve (17). The absolute flow reserve is the ratio of blood flow in a stenotic artery during maximal hyperemia to the blood flow in the same artery during resting conditions. Relative flow reserve is the ratio of blood flow in a stenotic artery during maximal hyperemia to the blood flow in an adjacent normal artery under the same maximal hyperemia condition. Both methods could be measured invasively using intracoronary Doppler ultrasound to directly measure velocity flow in the coronary arteries. Fractional flow reserve is

defined as the ratio of hyperemic flow in the stenotic coronary artery to the theoretical hyperemic flow if the same artery is normal. This is achieved by measuring pressure before and after the stenosis of interest. Due to the variability of normal values and inability to distinguish epicardial and microvascular disease when using intracoronary Doppler ultrasound methods, fractional flow reserve has slowly become the gold standard for hemodynamic assessment of coronary stenosis.

2.2. Coronary artery disease (CAD)

2.2.1 Pathophysiology

Coronary artery disease (CAD), or ischemic heart disease (IHD), is a result of atherosclerosis in the epicardial coronary arteries, or a build-up of plaque composed of fatty deposits along segments of the coronary lumen, which impedes blood flow to the myocardium. Patients with CAD may be symptomatic or asymptomatic and can present with stable angina pectoris (chest pain during exertion), unstable angina pectoris (unexpected chest pain at rest), or myocardial infarction (MI, heart attack).

There are two extreme phases of CAD, chronic or acute manifestations, leading to stable or unstable angina or MI. During the initial stages of plaque progression, atherosclerotic lesions start by growing outward, away from the lumen. In an acute phase, substantial outward remodeling occurs, resulting in plaque generally composed of thin fibrous caps and large lipid pools which may lead to thrombosis. These lesions are considered as high-risk plaques which are prone to rupture, leading to unstable angina or MI. In the chronic phase, lesions generally have smaller lipid cores, thicker fibrous caps, and calcification. These lesions are more stable, has less positive remodeling, and tend to protrude into the vessel lumen, leading to insufficient blood

flow to the myocardium or myocardial ischemia (16,18,21). Many atherosclerotic lesions may fall in-between these two extremes, resulting in a mixture of different types of atherosclerotic plaques and clinical manifestations.

2.2.2 Diagnosis

This dissertation will focus on the discussion of chronic stable CAD. In approximately 50% of all patients, chronic stable angina is the initial manifestation of CAD (22). Chronic stable angina, also called angina pectoris, is a common type of angina associated with chest discomfort brought on by exertion or emotional stress and could be relieved with rest or administration of nitroglycerin (19,22,23). In patients with chest pain, initial diagnosis of stable CAD includes history, physical examination, and observation of changes on the electrocardiogram (ECG) to assess the probability of CAD (24). It has been shown that severe angina, older age, female sex, history of smoking, and abnormal ECG has been correlated with clinically significant CAD assessed using invasive coronary angiography (ICA)
(4,19,23,25). Stress testing during ECG measurement, imaging techniques, and invasive catheterization assessments are common diagnostic tools for the assessment of stable CAD. This section briefly introduces a few anatomical and functional assessment tools used for the diagnosis of coronary lesions.

<u>Anatomical assessment:</u>

In current clinical routine and research, various methods have been used to assess the anatomical features of diseased coronary vessels to guide clinical management. Features such as percent diameter stenosis and plaque characteristics are commonly used in current clinical practice to help guide patient management and determine the need for coronary revascularization.

Quantifications of these features could be done invasively or noninvasively using various imaging methods. The sections below will briefly introduce a few existing methods and their advantage and disadvantages.

Invasive coronary angiography (ICA) is the most widely used diagnostic method for the assessment of luminal obstruction and location of coronary disease(26). Based on the American Heart Association (AHA) guidelines, a "significant" stenosis is defined as ≥ 70% diameter narrowing (≥ 50% for left main CAD)(4). Studies have shown the over use of ICA procedures in the past years, where over 50% of patients who undergo ICA were found to have non-obstructive (< 50% degree stenosis). In addition, the method requires exposure to radiation and it's inherently an invasive procedure which may lead to surgical complications.

Intravascular ultrasound (IVUS) and optical coherence tomography (OCT) are two invasive methods used for coronary plaque characterization. IVUS utilizes ultrasound waves to provide anatomical characterization of the coronary lesion in terms of vessel size and plaque composition. More recently, OCT has been broadly investigated in stable CAD patients with superior spatial resolution (<10μm) for the assessment of superficial components including the thickness of the fibrous cap, lipidic plaques and vulnerable plaques(26). Both methods have the potential to determine the risk of coronary plaque rupture, which could potentially improve the prognosis of the patient. However, the technique remains expensive and time-consuming(27).

Coronary computed tomography angiography (CTA) is a widely used noninvasive method for the assessment of lumen narrowing and recently has been used for the assessment of plaque characteristics using quantification of Hounsfield units (HU) associated with plaque. However, the method is stringent where only patients with adequate breath holding, without severe obesity, with relatively low calcium score (e.g. Agatston score < 400), and low heart rate,

could undergo a coronary CTA. In addition, although coronary CTA is a noninvasive diagnostic tool, the method still requires the exposure to radiation(26).

Coronary magnetic resonance imaging (MRI) is a noninvasive technique for the visualization of coronary arteries. Coronary MR angiography (MRA) could be used to assessed the degree of coronary stenosis. Recent studies have also shown the reliability of using MRI for the characterization of plaque composition denoted as coronary atherosclerosis T1-weighted characterization (CATCH)(28). MRI has the advantage of no ionizing radiation exposure to the patient and has the potential to assess both cardiac anatomy and function in one exam. However, the technique requires long imaging times, provides lower spatial resolution and require skilled technicians for data acquisition.

Functional assessment:

As anatomical assessments could provide important information, the functional information is also interesting as the overall CAD mechanism is due to the reduction of blood flow to the myocardium leading to a lack of oxygen delivery. Numerous studies have investigated the feasibility of using functional assessment to guide clinical management. This section will briefly introduce a few methods used to assess the hemodynamic significance of coronary stenosis.

Intracoronary Doppler ultrasound, as mentioned briefly in *chapter 2.1.4,* is an invasive method used to measure coronary flow velocity for the assessment of coronary flow velocity reserve (CFVR = ratio of maximum to baseline flow velocity). Clinical studies have shown that a CFVR of < 2.0 is associated with abnormal myocardial perfusion(29) and patients with CFVR of > 2.0 have shown favorable prognosis after deferred ICA(30). The method

accounts for both epicardial resistance and myocardial resistance which could be useful for studies of microvascular disease. However, the method is not lesion-specific and the normal values are not clearly defined(17).

Fractional Flow Reserve (FFR) is an invasively determined index of the functional severity of a coronary stenosis (31). The FFR index is obtained by measuring the pressure distal of a stenosis lesion and the aortic pressure simultaneously using a pressure guide-wire and guide-catheter, respectively. The theory behind FFR is that during maximum coronary and myocardial hyperemia, the myocardial resistance is minimal and coronary blood flow is proportional to coronary pressure. In the presence of stenosis, maximum achievable blood flow to the myocardium would be decreased, meaning the maximum perfusion pressure would also be decreased. This could be represented by the equations below:

$$Q^N = \frac{(P_a - P_v)}{R}$$

$$Q^S = \frac{(P_d - P_v)}{R} \qquad (2.2-1)$$

Where Q^N and Q^S are normal and stenotic maximum myocardial blood flow, R is the myocardial resistance at maximum vasodilation, P_a, P_d and P_v represents the mean aortic, distal coronary, and mean central venous pressure at maximum hyperemia, respectively. Since during hyperemia, coronary resistance (R) is negligible, flow (Q) therefore is correlated to pressure (P), hence FFR describing flow to the myocardium (Qs/QN) could be represented using pressure as:

$$FFR = \frac{(P_d - P_v)}{(P_a - P_v)} \qquad (2.2-2)$$

In general, since central venous pressure is negligible or close to zero, the equation could be simplified to the equation below where P_a and P_d could be measured invasively using pressure catheters(17).

$$FFR = \frac{P_d}{P_a} \qquad (2.2-3)$$

Studies have shown an index of ≤ 0.80 is identified as a functionally significant stenosis associated with cardiac death or MI, where patients may benefit from PCI, with an accuracy of greater than 90% (31-35). Although invasive FFR has been established as the gold standard, it remains an invasive procedure with radiation exposure, long procedural times, patient discomfort due to adenosine, and high surgical costs (36).

Instantaneous Wave-free Ratio (iFR) is also an invasive pressure measurement technique that's based on the concepts of FFR. The iFR ratio is, similar to FFR, pressure measured at distal of stenosis to the aortic pressure as shown below in the equation below:

$$iFR = \frac{Pd_{\,wave-free\ period}}{Pa_{\,wave-free\ period}} \qquad (2.2-4)$$

However, instead of measuring the average pressure over the entire cardiac cycle during maximum hyperemia, iFR measures the average pressure at a wave-free period (i.e. the beginning of diastole is defined at the dicrotic notch where the wave-free period is 25% of the way into diastole and ending 5 ms before the end of diastole) during resting conditions. It was shown by Sen et al. that during the wave-free period when patient is at rest, coronary resistance is naturally minimal, similar to the resistance level observed during maximum hyperemia for FFR measurements (37). Therefore, iFR is a method where no adenosine administration is needed to detect the functional significance of a coronary stenosis. Two recent studies, DEFINE-FLAIR(10) and iFR-SWEDHEART(9) have shown that an iFR cut-off value of 0.89 is non-

inferior to a FFR cut-off value of 0.80 with the advantage of a shorter operation time and less chest discomfort as no adenosine administration is needed during the time of operation.

Positron emission tomography (PET), single photon emission computed tomography (SPECT), and cardiac magnetic resonance (CMR) perfusion imaging techniques are noninvasive imaging methods for the assessment of myocardial perfusion defects to assess the extent of myocardial ischemia. Although PET and SPECT are noninvasive imaging methods, both techniques require injection of radionuclides, which involves ionizing radiation. Studies have shown that myocardial perfusion imaging methods are useful tools for patients with intermediate to high likelihood of having CAD(38). CMR perfusion imaging has the advantage of no ionizing radiation. A recent study using CMR myocardial perfusion imaging has shown promise as a noninvasive management strategy for patients with stable angina. Preliminary results showed that MR perfusion imaging is non-inferior to invasive catheterization supported by FFR in a 1-year outcome study, suggesting the potential of the technique for patient management (39).

Echocardiography and cine-CMR are two methods used to for the assessment of left ventricular function to evaluate myocardial wall motion abnormalities. Wall motion abnormalities have shown to be an indicative of CAD. In echocardiography, stress and rest induced wall motion abnormalities may represent ischemia and infarcted myocardium, respectively. Cine-CMR has the advantage of excellent soft-tissue contrast where patients with poor echocardiography may be recommended for cine-CMR.

CT-FFR utilizing CTA in combination with computational fluid dynamics (CFD) simulations to derive a noninvasive FFR value, denoted as FFR_{CT}, has shown an accuracy of 81% in the most recent clinical trial, using invasive FFR as a gold standard.(40). Recent studies have

looked into a machine-learning approach to derive FFR from coronary CTA images and results showed an accuracy of 83% in a small pilot study with substantial reduction in computation time(41) compared to the CFD approach. However, coronary CTA requires exposure to ionizing radiation and is more prone to blooming artifacts caused by heavy calcification.

2.2.3 Treatment

In current medical practice, two main treatment strategies for CAD patients are used, medical therapy or coronary revascularization. In high risk patients (annual mortality of > 3%) with myocardial ischemia of > 10% or high-risk angiographic findings based on ICA may benefit from revascularization techniques such as percutaneous coronary intervention (PCI) or coronary artery bypass graft (CABG) (26,42-44). In patient with myocardial ischemia of < 10% or stenotic lesions that do not induce ischemia, PCI may not be beneficial, whereas medical therapy (antianginal therapy or beta blockers) may be more or equally effective (26,35,45).

In general, for clinical noninvasive risk stratification, high risk patients are defined as severe resting and/or stress left ventricular (LV) dysfunction, resting and/or stress perfusion abnormalities >10% of the myocardium, stress ECG findings including ≥ 2 mm of ST-segment depression at low workload, wall motion abnormalities, and multi-vessel obstruction CAD (≥ 70% stenosis) or left main stenosis (≥ 50% stenosis) on coronary CTA(46). For clinical invasive risk stratification, ICA and FFR are normally used to determine the significance of stenosis as described in the previous section. Other measures such as IVUS, OCT or CFVR are used if the ICA and FFR weren't clear in defining the need for coronary revascularization (46).

2.3 Fundamentals of magnetic resonance imaging (MRI)

2.3.1 Introduction

Previous sections have briefly touched upon a variety of noninvasive medical imaging modalities for the diagnosis of stable coronary artery disease. These methods include coronary computed tomography angiography (CTA), positron emission tomography (PET), single photon emission tomography (SPECT), echocardiography, and magnetic resonance imaging (MRI). This section will dive deeper into the principles of MRI and further discuss the concepts of flow velocity quantification in cardiac magnetic resonance (CMR).

MRI is a powerful medical imaging tool used for the detection of both anatomical and physiological processes in the human body. Information generated by MRI is based on the interaction of certain atomic nuclei of interest (e.g. hydrogen) in different types of magnetic fields. Hence, it is relatively safe and a truly "noninvasive" method as it doesn't utilize any ionizing radiation. The noninvasive nature of the technique, thus, allows for repeated studies for monitoring of disease progression or regression at any age category. In addition, MRI offers great flexibility to image a broad range of tissue properties, metabolic processes, and functional information based on different variations of the magnetic fields and instrumental parameters. The following sections will further introduce the basic principles of MRI. The details of the concepts discussed in this section could be found in the following textbooks: (47-50)

2.3.2 Basics of MRI

The origin of MRI begins with nuclear magnetic resonance (NMR) where atoms containing an odd number of protons and/or neutrons have an intrinsic angular moment (or 'spins'). As the human body is composed largely of hydrogen (e.g. 50-65% water and 5-10% fat), the hydrogen atom (^{1}H) with a single proton is most commonly studied, which could be referred

to as hydrogen (proton) imaging. The overall concept of MRI is based on the interactions of these 'spins' (e.g. hydrogen) in three types of magnetic fields: main magnetic field (B_0), radiofrequency field (B_1), and linear gradient fields (G).

Main magnetic field (B_0):

In the presence of a static main magnetic field (B_0), the magnetic moment vector (e.g. hydrogen nucleus) will tend to align along the direction of the external static magnetic field when at equilibrium, which is generally denoted as the z-direction or the longitudinal direction. In the meantime, the nuclear spins are also precessing around the field direction at an angular frequency (f) known as the Larmor frequency represented by the equation below:

$$\omega = \gamma B$$

or

$$f = \frac{\gamma}{2\pi} B \qquad (2.3-1)$$

where γ is the gyromagnetic ratio. For hydrogen (^{1}H) specifically, $\gamma/2\pi$ = 42.58 MHz/Tesla. Therefore, in a 3.0 tesla MRI scanner (B_0 = 3.0 T), the Larmor frequency is 127.74 MHz which lies within the radiofrequency region.

Radiofrequency field (B_1):

To generate a MRI signal, a radiofrequency (RF) magnetic pulse (B_1) that's tuned to the resonance frequency (i.e. the Larmor frequency at 127.74 MHz to image hydrogen on a 3.0 tesla scanner) is applied in the xy-direction or the transverse direction, to excite the spins out of its equilibrium state (z-direction). Based on the prescribed strength and duration of B_1, which could be represented as an angle, the magnetization rotates away from the longitudinal direction (Mz) and towards the transverse plane (Mxy). Generally, the strength and duration of B_1 is on the

orders of a few micro-tesla and a few milliseconds, respectively. Once B_1 is off, the spins start to relax back to its equilibrium state at a rate of T1 (i.e. recovery of the magnetization vector along the longitudinal direction) and T2 (i.e. decay of the magnetization vector in the transverse plane). It is important to note that the rate of T1 recovery and T2 decay differs for different types of tissue and are not constant over time. Based on the Faraday's law of induction, As the spins are rotating back to its equilibrium state, the vectors induce a voltage or electromotive force (EMF), which could be detected by a receiver coil orientated to detect the magnetization signal in the transverse plane. The generated signal is denoted as a free induction decay (FID) and a set of FIDs is normally collected and used to reconstruct an MR image.

Linear gradient fields (G):

To distinguish the signals generated from different spatial locations, linear gradient magnetic fields in the x, y, and/or z directions are applied to the main B_0 field. Adding the gradient fields, the overall magnetic field could be expressed as:

$$\begin{aligned} \boldsymbol{B}(\boldsymbol{r},t) &= (B_0 + \boldsymbol{G}(t)\cdot\boldsymbol{r})\boldsymbol{k} \\ &= \left(B_0 + G_x(t)x + G_y(t)y + G_z(t)z\right)\boldsymbol{k} \end{aligned} \qquad (2.3-2)$$

This allows a linear change of the spins Larmor frequency in the direction of the applied gradient magnetic field. Thus, if a time-varying x-gradient is on, the Larmor frequency would vary with x-position and could be represented as:

$$\omega(x,t) = \omega_0 + \Delta w(\boldsymbol{r},t) = \gamma(B_0 + G_x(t)x) \qquad (2.3-3)$$

The magnetic gradient field is generally defined by the gradient amplitude (mT/m), the time it takes to reach the maximum gradient strength (i.e. the slew rate, mT/m/ms), the gradient duration (ms), and the applied gradient direction (x, y, and/or z).

To obtain an MRI image, the FID signal is encoded for each dimension using the magnetic field gradients. This is achieved by frequency encoding, phase encoding, and selective excitation to obtain the x, y, and z spatial information, respectively. **Figure 3**. shows a pulse sequence commonly used in MRI (i.e. Gradient echo imaging).

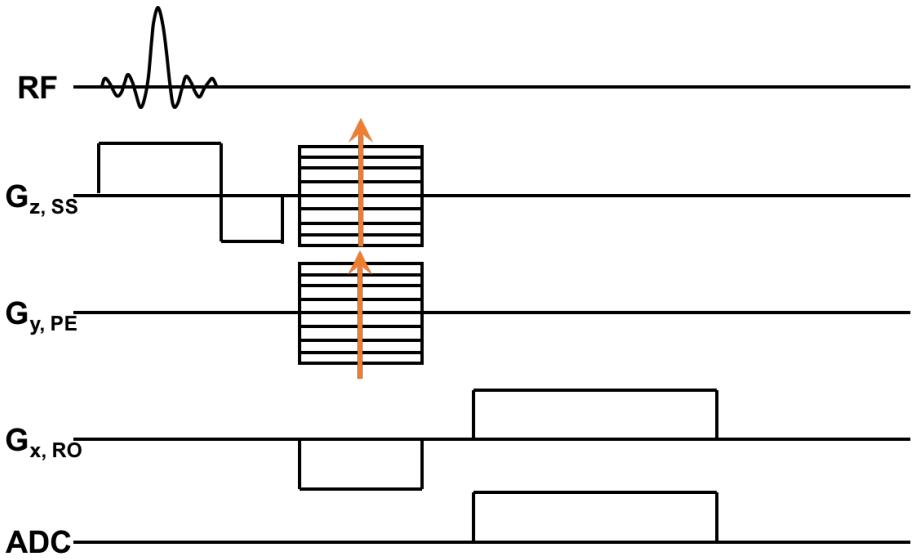

Figure 3. Example of a 3D gradient echo imaging sequence. As in the Gz direction, slice selective and phase encoding are both on, making it a slab selective excitation where within an imaging slab, multiple slices are collected. SS: slice selective, PE: phase encoding, RO: read-out; RF: radiofrequency;

1) Selective excitation serves as spatial localization in the z-direction, which could be used to excite an imaging slab for 3D acquisition or one imaging slice for 2D acquisition. Selective excitation is achieved by applying B_1 in the presence of B_0 and a linear gradient field, which results in a range of frequencies within the slice selective region only, allowing acquisition within only the desired imaging slice or volume of interest. 2) Phase encoding serves as spatial localization in the y-direction resulting in a change of the Larmor frequency of each tissue component along the y-axis. This phenomenon induces a phase where all spins are precessing in

the same frequency, however, with a variation in phase at different spatial locations along the y-axis. 3) Frequency encoding serves as a spatial localization in the x-direction resulting in a change of the Larmor frequency of each tissue component along the x-axis. The results of these three steps produces a spatially unique signal for each pixel or voxel. A 2D or 3D Fourier Transform is then used to transform the encoded signal to the spatial domain, giving the final 2D or 3D images.

2.3.3 Phase contrast MRI

Previous section has implicitly assumed that the object being imaged is static, however, this may not be the case as not all organs in the human body is stationary. Motion such as flow in the blood vessels may be captured in the phase of the MR images, which could provide functional information of the cardiovascular system. This section introduces the basic principles of MR flow velocity mapping using a technique denoted as phase-contrast MRI (PC-MRI).

As mentioned in the previous section, the MRI signal is a vector, therefore has a magnitude and phase component which could be shown in **Figure 4**.

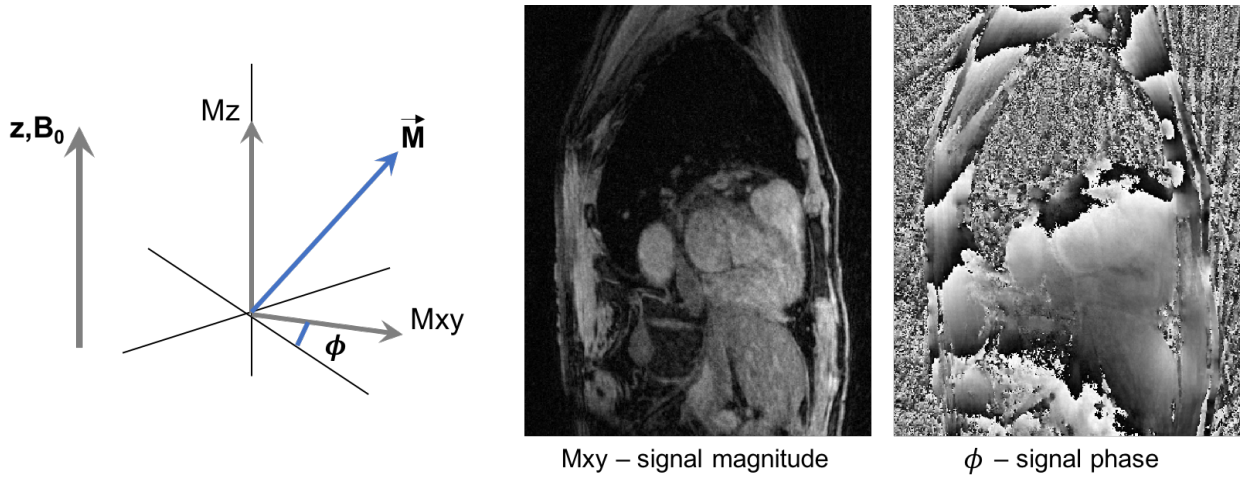

Figure 4. Example images of signal magnitude and phase. Mz is the longitudinal and Mxy is the transverse magnetization in the region of interest. The length of the transverse magnetization represents the magnitude and the orientation or angle of the vector represents the phase.

To expand upon *eq. 2.3-3*, the Larmor frequency of a static or moving spin could be represented as:

$$\omega(\boldsymbol{r},t) = \gamma B_z(\boldsymbol{r},t) = \gamma B_0 + \gamma \Delta B_0 + \gamma \boldsymbol{r}(t) \cdot \boldsymbol{G}(t) \qquad (2.3-4)$$

Where B_0 is the main static magnetic field, ΔB_0 is the local field inhomogeneity, $\boldsymbol{G}(t)$ is the time varying magnetic field gradient, and $\boldsymbol{r}(t)$ is the spin at a specified time and location. Integration of *eq. 2.3-4* results in the phase of the precessing magnetization, which could be represented as:

$$\begin{aligned} \emptyset(\boldsymbol{r},t) &= \emptyset(\boldsymbol{r},t_o) + \int_{t_o}^{t} \omega(\boldsymbol{r},t)dt \\ &= \emptyset(\boldsymbol{r},t_o) + \gamma \Delta B_0 (t-t_o) + \gamma \int_{t_o}^{t} \boldsymbol{G}(t)\, \boldsymbol{r}(t)dt \end{aligned} \qquad (2.3-5)$$

Using a Taylor series expansion of motion, the resultant phase of the spins could be represented as:

$$\emptyset(\boldsymbol{r},t) = \emptyset(\boldsymbol{r},t_0) + \gamma\Delta B_0(t-t_o) + \sum_{n=0}^{\infty}\emptyset_n\left(\boldsymbol{r}^{(n)},t\right)$$
$$= \emptyset_o + \sum_{n=0}^{\infty}\gamma\,\frac{\boldsymbol{r}^{(n)}}{n!}\int_{t_0}^{t}\boldsymbol{G}(t)(t-t_0)^n dt \qquad (2.3-6)$$

where $\boldsymbol{r}^{(n)}$ is the nth derivative of the time dependent spin position and $\emptyset_n$ is the corresponding nth order phase. $\emptyset_o$ represents the additional background phase due to its initial signal phase and field inhomogeneities. If the motion of the moving spins does not change drastically with respect to the imaging temporal resolution, then the velocities of the moving spins can be assumed constant during data acquisition. Hence, $\boldsymbol{r}(t)$ can be represented as $\boldsymbol{r}(t) = r_0 + v(t-t_0) + \cdots$ and *eq. 2.3-6* could be simplified as:

$$\emptyset(\boldsymbol{r},t) = \emptyset_o + \gamma\,\boldsymbol{r}_0\int_{t_o}^{t}\boldsymbol{G}(t)\,dt + \gamma\,\boldsymbol{v}\int_{t_o}^{t}\boldsymbol{G}(t)t\,dt$$
$$= \emptyset_o + \gamma\,\boldsymbol{r}_0 M_0 + \gamma\,\boldsymbol{v}\,M_1 \qquad (2.3-7)$$

Where M_n is the nth moments of the gradient waveform, where zero (M_0) and first (M_1) order gradient moments describe the influence of magnetic field gradients on the signal phase of the static spins at **r** and moving spins with velocities, **v**, respectively. M_o represents the area of the gradient waveform and M_1 represents the area of the gradient waveform and its duration.

$$M_0 = \int_{t_o}^{t}\boldsymbol{G}(t)\,dt \qquad (2.3-8a)$$

$$M_1 = \int_{t_o}^{t}\boldsymbol{G}(t)\,t\,dt \qquad (2.3-8b)$$

If $M_0 = 0$ where the static spins are refocused at the end of an echo, we could see from *eq. 2.3-9b* that the measured phase is then proportional to the velocity of the imaged area of interest. *Eq. 2.3-9a* shows the measured phase of the stationary spins (v = 0) and *eq. 2.3-9b* shows the measured phase of the moving spins (v ≠ 0).

$$\emptyset(\boldsymbol{r},t) = \emptyset_o \qquad (2.3-9a)$$

$$\emptyset(\boldsymbol{r},t) = \emptyset_o + \gamma\, \boldsymbol{v}\, M_1 \qquad (2.3-9b)$$

Unfortunately, the background phase ($\emptyset_o$) from magnetic field susceptibility and/or inhomogeneity is still present in the resultant phase measurement where only one image acquisition is not sufficient to achieve a pure velocity dependent phase measurement. As a result, typical PC-MRI experiments normally acquire an additional phase reference image that either has a gradient waveform with zero M_0 and an opposite M_1 component or a gradient waveform with zero M_1 and M_0. A zero M_1 and M_0 gradient waveform is also denoted as a flow compensated gradient waveform. The three gradient waveforms could be represented mathematically in *eq. 2.3-10* where *eq. 2.3-10a* has a flow compensated (FC) gradient waveform ($M_0 = 0$ and $M_1 = 0$), *eq. 2.3-10b* has a positive flow encoding (FE+) gradient waveform ($M_0 = 0$ and $+M_1$), and *eq. 2.3-10c* has a negative flow encoding (FE-) gradient waveform ($M_0 = 0$ and $-M_1$). T is represented as total duration of the flow compensated or flow encoded gradient waveforms. G is the gradient strength.

$$\emptyset(v)_{FC} = \emptyset_0 \qquad (2.3-10a)$$

$$\emptyset(v)_{FE+} = \emptyset_0 + \gamma \boldsymbol{G}(T/2)^2\, \boldsymbol{v} \qquad (2.3-10b)$$

$$\emptyset(v)_{FE-} = \emptyset_0 - \gamma \boldsymbol{G}(T/2)^2\, \boldsymbol{v} \qquad (2.3-10c)$$

Figure 5. shows the two types of gradients, flow encoding bipolar and flow compensated gradients. A bipolar gradient has a gradient moment of $M_0 = 0$ and M_1 (or velocity), where velocity induced phase shifts in arbitrary directions could be controlled in the MRI system by manipulating the amplitude, slew rate, total duration, and direction of the first gradient moment

(M_1). Flow compensated gradients has a gradient moment of $M_0 = 0$ and $M_1 = 0$, where the phase of both static and flowing spins is refocused back to zero at the end of the echo.

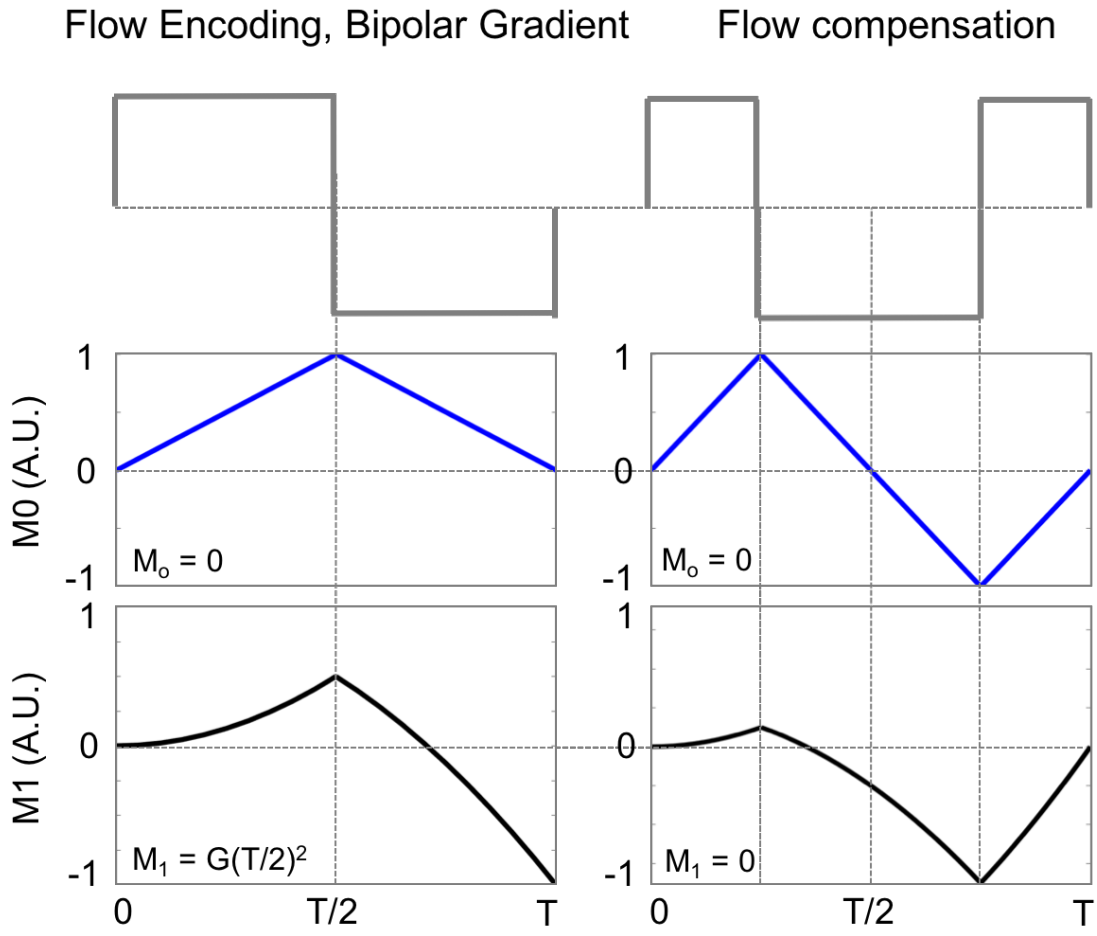

Figure 5. Example gradient waveforms commonly used for PC-MRI acquisition and their corresponding zero (M_0) and first (M_1) moments. Left: bipolar gradient, right: flow compensated gradients.

To isolate phase signal for the detection of moving spins only, a phase difference image could be formed. Two types of subtraction could be performed: 1) phase difference between flow encoding and flow compensated gradient waveforms (*eq. 2.3-11a*) or 2) phase difference of alternating flow encoding polarities (*eq. 2.3-11b*).

$$\Delta\emptyset = \pm\gamma G(T/2)^2 v \qquad (2.3-11a)$$

$$\Delta\emptyset = 2\gamma G(T/2)^2 v \qquad (2.3-11b)$$

The velocity can then be represented as:

$$v = \frac{\Delta\emptyset}{\gamma(\pm G(T/2)^2)} = \frac{\Delta\emptyset}{\gamma(\pm M_1)} \qquad (2.3-12a)$$

$$v = \frac{\Delta\emptyset}{\gamma(2G(T/2)^2)} = \frac{\Delta\emptyset}{\gamma(2M_1)} \qquad (2.3-12b)$$

Since phase is a periodic signal limited to –π to π, a maximum velocity, denoted as *VENC*, could be encoded for a given change in the first moment and any measured velocity that's higher than the prescribed *VENC* will alias as the lower velocity, which is one of the major disadvantages of PC-MRI. *VENC* could be defined as:

$$VENC = \frac{\pi}{\gamma(\Delta M_1)} \qquad (2.3-13)$$

where ΔM_1 is the difference between the first moment gradient waveforms. During PC-MRI acquisition, it is important to perform a *VENC*-scout or have prior knowledge of the maximum velocity in the imaging vessel of interest to avoid any phase wrap in the phase images.

Velocity encoding described above could be performed for each velocity direction by applying the flow encoding and flow compensated gradient waveforms in each gradient direction (x, y, and/or z-gradients). To ensure an optimum acquisition time for three-directional velocity encoding, various velocity encoding strategies have been studied. The most commonly used velocity encoding method is the simple four-point method, which will be the focus of this dissertation. The simple four-point method uses a phase reference $\emptyset_0$ (flow compensated gradient waveform), and different velocity encoded phases in each measured direction, providing $\emptyset_x$, $\emptyset_y$, and $\emptyset_z$. The velocity components are then computed by subtracting $\emptyset_0$ from $\emptyset_x$, $\emptyset_y$, and $\emptyset_z$, similar to *eq. 2.3-12a*.

$$v_x = \frac{\emptyset_x - \emptyset_0}{\gamma(\Delta M_1)}$$

$$v_y = \frac{\emptyset_y - \emptyset_0}{\gamma(\Delta M_1)} \qquad (2.3-14)$$

$$v_z = \frac{\emptyset_z - \emptyset_0}{\gamma(\Delta M_1)}$$

In PC-MRI imaging, several effects can introduce errors in the velocity measurements by affecting the first moments used for velocity encoding. The three major factors are eddy current effects, Maxwell terms, and gradient field distortions. Background phase errors from the Maxwell gradient terms and gradient field distortions are commonly applied within the image reconstruction framework of most vendors. Time-varying magnetic fields and changes in different gradient waveforms could lead to different eddy current effects, which results in phase changes in the resultant phase images. To eliminate the eddy current induced errors, additional post processing is required to regain the original velocity encoded phase. The most common correction method is based on the subtraction of the spatially varying eddy current induced phase changes estimated from static tissue. In common practice, static tissues such as the chest wall, liver and back are normally used for eddy current correction.

2.3.4 Cine phase contrast MRI

As flowing blood in the body is periodic, PC-MRI acquisitions are typically gated to the cardiac cycle. Image acquisition in areas such as the intracranial, carotid, and peripheral vessels, cardiac electrocardiogram (ECG) gating should be sufficient. However, in areas such as the heart or abdomen, additional gating or breath-hold may be necessary to minimize respiratory motion. To capture the variation of blood flow from systole to diastole, images are acquired in segments at different time points throughout the cardiac cycle where only a few imaging lines

could be collected per cardiac phase. Hence, depending on the desired temporal resolution per cardiac phase, the number of imaging lines per cardiac phase may vary. Imaging segments are collected throughout multiple cardiac cycles and combined together to generate a time resolved image set to depict the dynamics of blood flow in a cardiac cycle. This section will dive into the basic concepts of how to obtain a cine PC-MRI.

ECG is commonly used in healthcare to record the electrical activity of the heart throughout a period of time using electrodes placed on the surface of the skin. In MRI, depending on the vendor, 3-4 leads are used for detection of the cardiac rhythm. A normal cardiac rhythm produces four entities, a P wave, a QRS complex, a T wave, and a U wave where each wave has its unique pattern. Cardiac gating utilizes mainly the QRS complex, as it is most prominent and exhibits the highest amplitude in the ECG signal, for triggering data acquisition.

Cardiac gating could be performed prospectively or retrospectively. Prospective ECG triggering allows a user defined trigger delay time and data acquisition window, whereas retrospectively ECG triggering collects all data within the RR-wave and repeats the data acquisition scheme once it reaches to the next R-wave. **Figure 6** shows an example of ECG triggered segmented cine acquisition.

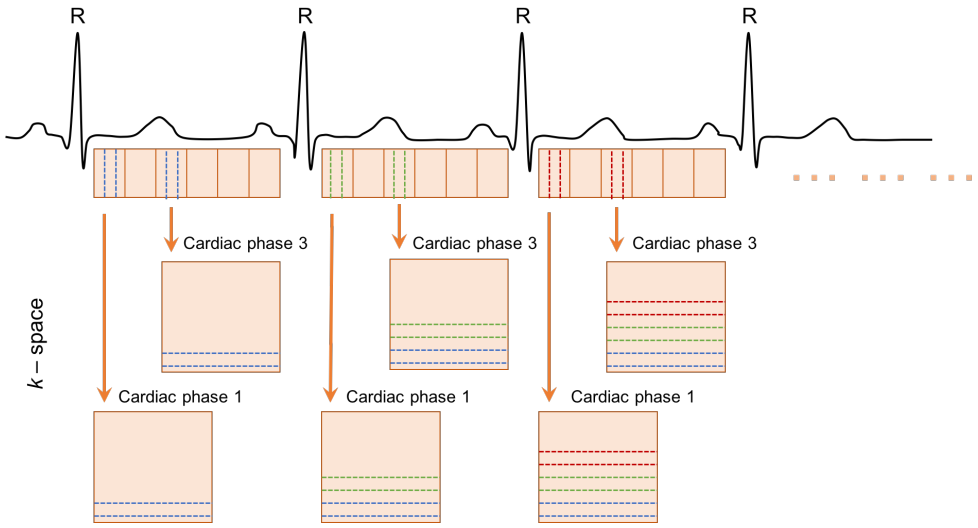

Figure 6. Example of an ECG triggered segmented cine acquisition. A set of imaging lines are collected within each cardiac phase per R-R wave (heart beat). Each set of imaging lines are then combined between different heart beats until a full set of k-space is collected.

To ensure sufficient temporal resolution, cardiac segmentation is used where a set of imaging lines are collected per cardiac phase, per heartbeat. As the number of imaging lines within a set increases, more lines of k-space are collected per cardiac phase, resulting in a shorter scan time with the expense of lower temporal resolution. Essentially, cine PC-MRI is phase (velocity) data across one cardiac cycle, "averaged" over N cardiac cycles.

2.4 Noninvasive pressure gradient measurement

2.4.1 Introduction

As mentioned in *Chapter 2.2*, pressure measurements play an important role in the diagnosis of coronary artery disease. Invasive pressure derived index, FFR, using catheter based methods to directly measure pressure in the coronary arteries, has shown great promise, with an accuracy of > 90%, as a diagnostic tool for PCI treatment (31-35). In addition, pressure is also an

important marker for other clinical applications such as aortic valve stenosis(51), aortic coarctation(52), and vessel stenosis in areas such as carotid, renal or iliac arteries. In current clinical routine, invasive catheterization procedures are considered as the gold standard for pressure measurement in vivo. Although invasive methods have shown promise for clinical diagnosis, it remains an invasive procedure with its inherent risks, severe side effects, radiation exposure, and high surgical costs (36). Ultimately, a noninvasive technique would be desired. Doppler echocardiography and PC-MRI are two noninvasive methods that could directly measure blood flow velocity in vivo. The velocity obtained from these techniques could then subsequently convert to pressure gradients.

Doppler echocardiography utilizes sound frequency shift of a moving target to determine blood flow velocity in the cardiac chambers and great vessels. The method allows measurement of flow velocity (speed), direction of flow (towards or away from transducer), and real-time signal with high temporal resolution throughout multiple cardiac cycles. This information could then be used with the Bernoulli's equation to subsequently calculate pressure (53,54). It is important to note that Doppler echocardiography, although uses similar concept as intracoronary Doppler ultrasound, differs in that it's a noninvasive method that's used externally on the surface of the skin.

PC-MRI is a noninvasive imaging technique that can directly quantify blood flow velocity in all orthogonal directions (V_x, V_y, V_z). The basic concepts of PC-MRI have been extensively explained in *Chapter 2.3*. The measured velocities can be utilized to derive pressure gradient across a vessel of interest, hence giving a noninvasive pressure gradient measurement. Velocities from PC-MRI could be used for both Bernoulli and Navier-stokes calculations as both spatial (V_x, V_y, V_z) and temporal (V_t) velocities are obtained. PC-MRI has the advantage of

measuring blood flow in almost all vessels (small or large) throughout the human vascular system (55-57). This dissertation will mainly focus on the work of using PC-MRI with the Navier-stokes approach as this approach has the advantage of estimating both temporal and spatial distribution of pressure gradients within various sized vessels. This section introduces the basic concepts of the Bernoulli's and Navier-stokes equations and some clinical applications.

2.4.2 Basics of fluid flow

Under conditions of laminar flow in a viscous fluid, the velocity profile tend to be radially symmetric with a parabolic shape. We could express the mean velocity across the diameter of the tube as:

$$V(r,t) = V_m(t)\left[1 - \left(\frac{r}{R}\right)^n\right] \qquad (2.4-1)$$

where $V_m(t)$ is the maximum velocity at time t. For a parabolic velocity profile, n = 2. By taking the integral of *eq. 2.4-1* we could find the mean velocity. In the case of a parabolic velocity profile, $V_{mean} = 1/2\, V_{max}$ (58). Below, definitions of a few fluid dynamic terms are introduced.

Compressibility is describing the phenomenon of changes in pressure or temperature in a fluid which causes changes in density overtime. Although all fluids are compressible in some way, in most cases the changes in pressure or temperature are small enough where the change in density is negligible. This is known as an incompressible fluid where it's assumed that density is constant and does not change as it moves through the flow field.

Laminar flow or non-turbulent flow occurs when fluid flows in parallel layers (along its own streamline) without mixing between the adjacent layers. Unlike turbulent flow, laminar flow is smooth, tend to travel in an orderly regime, and occur at lower velocities. In contrast, turbulent flow intertwines and crosses between the adjacent layers in an irregular manner resulting in

mixing of the fluid, especially in high velocities. A previous study by Nosovitsky et al. has studied the assumption of laminar flow in stenotic arteries for the calculations blood flow using computational fluid dynamic models. The study used a model with reference artery diameter (D) of 4 mm, blood density (ρ) of 1050 kg/m^3, blood viscosity (μ/ρ) of 3.6e-6 m^2/s, and an inflow coronary velocity of approximately -0.1 to 0.65 m/s (range of flow velocity over the cardiac cycle) and found that the results of velocity vectors between laminar and turbulent models for 25 and 75% stenosis levels were similar, leading to the conclusion that the effects of turbulence are small and can safely be neglected
(59,60).

Newtonian fluids are fluids whose viscosity does not change with the rate of flow. A non-Newtonian fluid, in contrast, experiences changes in viscosity due to increased shear stress. Johnston et al. studied the differences between Newtonian and non-Newtonian fluid blood flow in human right coronary arteries and found that when studying the wall shear stress for blood flow in arteries, the use of a Newtonian blood model for approximation is reasonably sufficient (24,60,61). As the calculation of shear stress is related to pressure different, it could be assumed that a Newtonian fluid for pressure difference calculations is sufficient.

2.4.3 Quantification of noninvasive pressure gradient

Bernoulli's equation:

The Bernoulli's equation is based on the principle of conservation of energy where the total amount of energy within an isolated system remains constant over time and it can only be transformed from one form to another and can be neither created nor destroyed. The Bernoulli equation can be expressed in *eq. 2.4-2*.

$$P_1 + \frac{1}{2}\rho v_1^2 + \rho g h_1 = P_2 + \frac{1}{2}\rho v_2^2 + \rho g h_2 \qquad (2.4-2)$$

where P = pressure, ρ = fluid density, v = fluid flow speed at a point on a streamline, g = acceleration due to gravity, and h = elevation above a reference plane. For in vivo applications, the difference of height between point 1 and point 2 are assumed negligible, therefore the pressure gradient calculation could be simplified to:

$$P_1 - P_2 = \frac{1}{2}\,\rho\,(v_2^2 - v_1^2) \qquad (2.4-3)$$

If P_1 and P_2 are in units of millimeters of mercury, v_1 and v_2 are in units of meters per second, and blood density is 1060 kg/m^3, *eq. 2.4-3* could be simplified to:

$$P_1 - P_2 = 4\,(v_2^2 - v_1^2) \qquad (2.4-4)$$

If velocity at point 2 is a lot greater than the velocity at point 1 meaning $v_2 \gg v_1$, the equation is then simplified to what is commonly used in the clinical routine for noninvasive pressure gradient measurements
(53,54,58,62):

$$\Delta P = 4\,v_2^2 \qquad (2.4-5)$$

Navier-stokes equations:

The Navier-stokes equations, similar to the Bernoulli's equation, are derived from the conservation of momentum in a controlled volume. It is essentially a momentum balance of the pressure force, transient and convective inertia, viscous resistance, and the body force, represented as:

$$Pressure\ Force = Transient\ Inertia + Convective\ Inertia$$
$$-Viscous\ Resistance - Body\ Force$$

The Navier-stokes equations expresses the relationship between pressure gradients (∇P) and velocities ($\boldsymbol{V}$) in a non-turbulent, incompressible, Newtonian fluid (63-65), which could be expressed as:

$$-\nabla P = \rho \frac{\partial \boldsymbol{V}}{\partial t} + \rho \boldsymbol{V} \cdot \nabla \boldsymbol{V} - \mu \nabla^2 \boldsymbol{V} - \boldsymbol{F} \qquad (2.4-6)$$

where P is the pressure, ρ is the fluid density, $\boldsymbol{V}$ is the three-directional velocity (V_x, V_y, and V_z), μ is the fluid dynamic viscosity, and $\boldsymbol{F}$ includes the body force terms such as the gravitational forces in its respective directions. The Navier-stokes could also be represented in its Cartesian form as:

$$-\frac{\partial P}{\partial x_i} = \rho \frac{\partial v_i}{\partial t} + \rho \left[v_1 \frac{\partial v_i}{\partial x_1} + v_2 \frac{\partial v_i}{\partial x_2} + v_3 \frac{\partial v_i}{\partial x_3} \right]$$

$$-\mu \left[\frac{\partial^2 v_i}{\partial x_1^2} + \frac{\partial^2 v_i}{\partial x_2^2} + \frac{\partial^2 v_i}{\partial x_3^2} \right] - F_i, \qquad i = x, y, z \qquad (2.4-7)$$

On the right-hand side of the equation, the terms from left to right represent the transient inertia (local acceleration), three convective inertia components, viscous friction terms, and the gravitational force. The x_i's are the x-, y-, and z-axes in the image frame and the v_i's are the corresponding velocity components. The temporal ($\partial v_i / \partial t$) and spatial first order ($\nabla \boldsymbol{V}$) and second order ($\nabla^2 \boldsymbol{V}$) velocity derivatives could be calculated with a central or forward difference approximation using velocity values of the nearest temporal and spatial neighbors (62). For in vivo estimations, viscosity and density could be set to blood properties, (3 ~ 4) x 10^{-3} Pa·s and 1060 kg/m^3, respectively.

From the derived pressure gradients $[\partial P / \partial x_i]$ where x_i = x, y, z in the image frame, pressure gradient (ΔP) could be calculated using integration along a path (63,66), as represented in the equation below:

$$\Delta P = \sum_i \left[\left(\frac{\partial P}{\partial x} \right)_i \Delta x_i + \left(\frac{\partial P}{\partial y} \right)_i \Delta y_i + \left(\frac{\partial P}{\partial z} \right)_i \Delta z_i \right]$$

$$i = slice\ number \qquad (2.4-8)$$

where Δx_i, Δy_i, and Δz_i are the vector length of each linear segment along a predefined path determined by connecting the velocity points of consecutive cross-sectional slices, assuming integration is not path dependent. The total pressure difference, ΔP, is then calculated as the sum of all segments.

2.4.4 Applications of noninvasive pressure gradient

Many clinical applications, especially in cardiovascular disease, have adopted the use of the Bernoulli principle. Doppler echocardiography has incorporated the Bernoulli principle in many of its hemodynamic evaluations of the heart such as transvalvular gradients, intracardiac pressures and shunts, valvular stenosis, etc(53). However, the method is highly dependent on the skills of the operator when placing the probes and measurements of certain blood vessels may be difficult to achieve due to the limited degree of freedom as the transducer is on the surface of the skin.

With the development of PC-MRI, measurement of flow velocities in vessels > 2mm in diameter throughout the human body could be achieved. Since PC-MRI has the advantage of measuring flow velocity in three orthogonal directions, the Navier-Stokes equations have been more widely used for PC-MRI implementations. Noninvasive pressure gradient measurement using PC-MRI and Navier-stokes has been studied in different sized vessels such as the cardiac chamber (63,67-69), aorta (62,65,70,71), carotid (72,73), renal (64) and intracranial (74,75) arteries. In studies by Lum et al and Bley et al, highly significant correlations ($r \approx 0.95$) between ΔP derived from PC-MRI velocity maps with spatial resolution of 0.78-1.0mm isotropic and temporal resolution of ~39.2 - 45.6ms and ΔP measured from invasive pressure wire was observed in the carotid and renal arteries (64,73) with ~50-60% diameter stenosis (mean reference diameter: ~3.5 - 5 mm). Similar results were seen in the intracranial arteries where high

correlation was observed (r = 0.82) between PC-MRI derived pressure gradient and invasively micro-catheter measured pressure gradient in patients with intracranial aneurysms (75).

2.5 Statistical analysis

This section briefly introduces the statistical analysis methods used throughout the chapters in this dissertation. Intra-class correlation coefficient (ICC) was calculated using SPSS v.16.0 (IBM SPSS Statistics, Armonk, NY, USA) to test the statistical significant of similarity. Bland-Altman plots and Pearson linear regression were obtained using GraphPad Prism (GraphPad Software Inc, La Jolla, CA, USA) to assess the agreement and correlation, respectively, between repeat of the same technique and/or between the proposed and gold-standard methods. Unpaired two-tailed Student's t-test was used to determine any statistically significant differences. In cases where needed, Wilcoxon signed rank test was also performed to determine any statistical significant differences using SPSS software. In all tests, statistical significance was defined as $p<0.05$ and all numerical data were presented as mean ± standard deviation.

CHAPTER 3 – Validation of noninvasive pressure gradient measurement framework in stenotic flow phantoms

3.1 Introduction

Noninvasive pressure gradient measurement using phase-contrast MRI (PC-MRI) and Navier-Stokes (NS) equations have been briefly discussed in *chapter 2.3*. Many applications of the method focused on large to medium sized vessels and have shown good correlation with pressure gradients measured from invasive pressure wire. This chapter introduces the validation work of a noninvasive pressure gradient measurement framework in a small caliber flow phantom at various degrees of narrowing, mimicking the scenario of a various degrees of diseased coronary arteries. PC-MRI velocity values and NS derived pressure gradient measurements were assessed for their repeatability. In addition, correlation between PC-MRI derived pressure gradients and pressure gradients measured using a pressure transducer were evaluated.

3.2 Methods

3.2.1. Sequence design

A 2D spoiled gradient recalled echo, PC-MRI, sequence with a conventional four-point velocity-encoding scheme (reference, x, y, z) was used for image acquisition on a 3.0 T MR system (Verio, Siemens) (76). The three-directional velocity vector field (V_x, V_y, V_z) from all cross-sectional imaging slices was used as input parameters for pressure gradient estimation using NS equations (31,33,34,63).

3.2.2. Pressure difference estimation

To obtain the pressure difference (ΔP) across a region of interest, the NS equations were used to investigate the relationship between velocity and pressure. The NS equations, as briefly discussed in *chapter 2.3* is shown below in its Cartesian form. The equation expresses the conservation of momentum of a non-turbulent, incompressible Newtonian fluid (26,42-44):

$$-\frac{\partial P}{\partial x_i} = \rho\frac{\partial v_i}{\partial t} + \rho\left[v_1\frac{\partial v_i}{\partial x_1} + v_2\frac{\partial v_i}{\partial x_2} + v_3\frac{\partial v_i}{\partial x_3}\right]$$

$$-\mu\left[\frac{\partial^2 v_i}{\partial x_1^2} + \frac{\partial^2 v_i}{\partial x_2^2} + \frac{\partial^2 v_i}{\partial x_3^2}\right] - F_i, \qquad i = x, y, z \qquad (3-1)$$

where P is pressure, ϱ is fluid density, μ is fluid dynamic viscosity and F includes the body force terms. On the right-hand side of the equation, the terms from left to right represent the transient inertia (local acceleration), three convective inertia components, viscous friction terms, and the gravitational force. The x_i's are the x-, y-, and z-axes in the image frame and the v_i's are the corresponding velocity components. To calculate the temporal $[\partial v_i/\partial t]$ and spatial $[\partial v_i/\partial x_{1,2,3}]$ first order velocity derivatives, a forward difference approximation at the pixel with maximum coronary velocity identified in each PC-MRI cross-sectional slice was used. Using the maximum velocity could avoid any partial volume errors caused by the limited spatial resolution at the stenotic regions of the phantom. Due to the narrowness of the phantom tubing, it is spatially limited to accurately calculate the spatial second order velocity derivatives $[\partial^2 v_i/\partial x_{1,2,3}^2]$, therefore, to prevent any unwanted error, the viscosity terms were ignored assuming inviscid flow. In addition, since the phantom was horizontally positioned in the scanner during MR acquisition with minimal influence from gravity, the body force terms (F_i),

which includes gravity, is also neglected. The simplified form of the NS equation (Euler's equation, neglecting gravity) is used for all calculations as shown below:

$$-\frac{\partial P}{\partial x_i} = \rho\left[\frac{\partial v_i}{\partial t} + v_1\frac{\partial v_i}{\partial x_1} + v_2\frac{\partial v_i}{\partial x_2} + v_3\frac{\partial v_i}{\partial x_3}\right] \quad , \quad i = x, y, z \qquad (3-2)$$

Two methods were explored to obtain the pressure gradients. Velocity gradients from all three directions was first analyzed. As the in-plane velocities are small and may have minimal contribution to the overall pressure gradient, velocity gradient from through-plane direction only was also analyzed to explore this phenomenon.

From the derived pressure gradients $[\partial P/\partial x_i]$ where $x_i = x, y, z$ in the image frame, pressure difference [ΔP] was then calculated using integration along a path (63,66), as represented in the equation below:

$$\Delta P = \sum_i \left[\left(\frac{\partial P}{\partial x}\right)_i \Delta x_i + \left(\frac{\partial P}{\partial y}\right)_i \Delta y_i + \left(\frac{\partial P}{\partial z}\right)_i \Delta z_i\right], \qquad i = slice\ number \qquad (3-3)$$

where Δx_i, Δy_i, and Δz_i are the vector length of each linear segment along a predefined path determined by connecting the maximum velocity points of consecutive cross-sectional slices, assuming integration is not path dependent (31,35). The total pressure difference, ΔP, is then calculated as the sum of all segments shown in *eq. 3-3*.

3.2.3. Experiments

The feasibility of the technique was demonstrated in a stenotic phantom with various degrees of narrowing. Scans were performed on a MAGNETOM Verio 3.0 T MRI system (Siemens Healthcare, Erlangen, Germany) equipped with a 32-channel (Invivo, Gainesville, FL).

A schematic of the phantom design is shown in **Figure 7a**. Twelve stenotic phantoms with reference inner diameter (ID) of 4.8 mm at a range of 0% - 60% diameter stenosis (DS) were individually connected to a flow pump (Masterflex, Cole-Parmer®, IL, USA) that pumped gadolinium-doped water (density of ~1000 kg/m^3) at a constant volume velocity of 250 mL/min while 2D PC-MRI images were acquired. Imaging parameters were: field of view (FOV) = (215 x 215 mm)^2; flip angle (FA) = 15^o; echo time (TE) = 3.86 - 4.51 ms; repetition time (TR) = 67.12 - 73.92 ms; in-plane spatial resolution = (0.50 - 0.58 x 0.50 - 0.58 mm)^2; slice thickness = 3.2 mm; V_{enc} = z (40 – 260 cm/s) and x, y (40 – 80 cm/s), depending on %DS. Repeat scans were performed in seven of the twelve phantoms to assess reproducibility. Immediately following the PC-MRI scans, pressure was measured using a pressure transducer (Invivo, FL, USA), as shown in **Figure 7a**, before and after the maximum narrowing. Examples of 2D PC-MRI images are shown in **Figure 7b.**

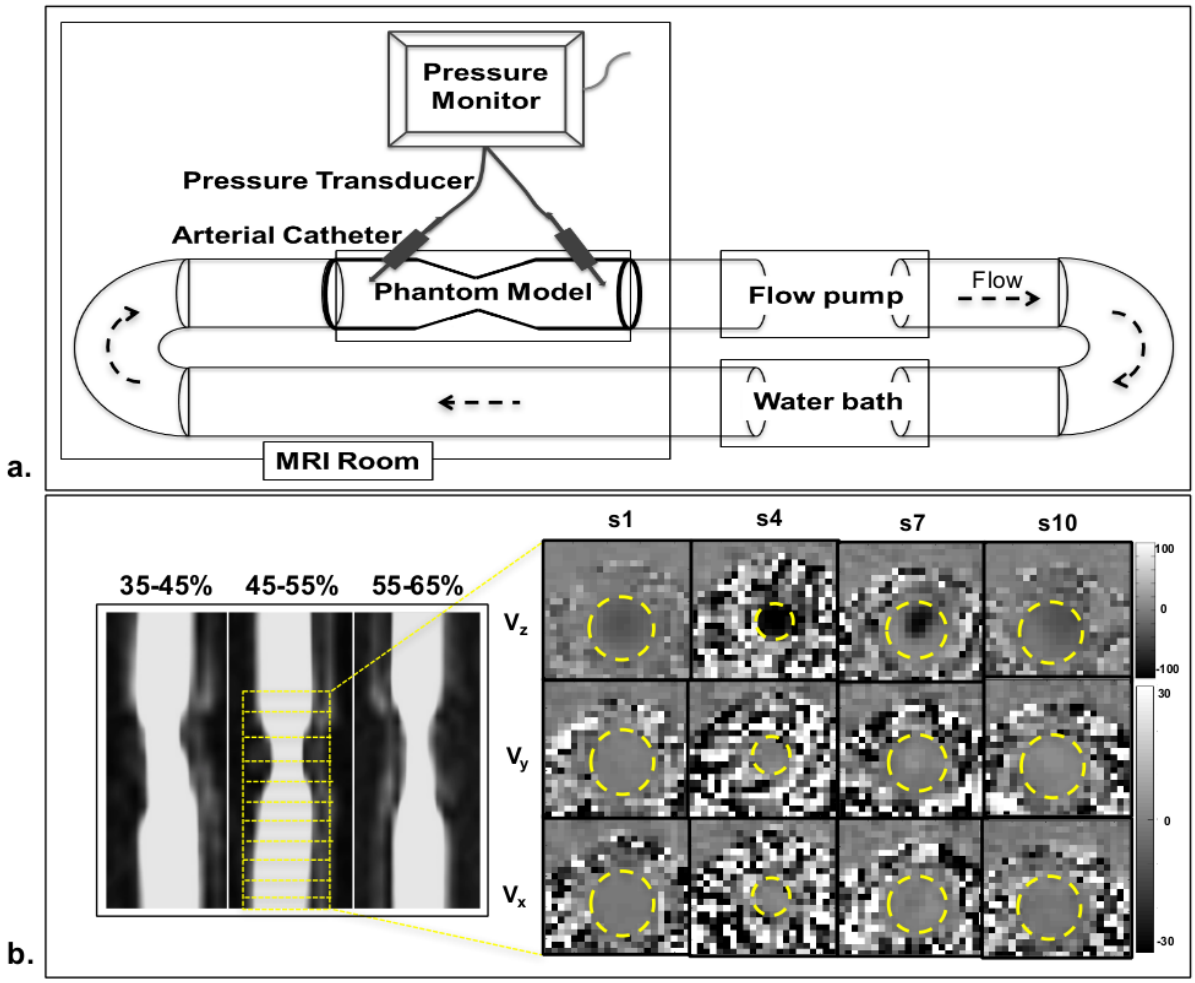

Figure 7. a. Schematic of the stenotic phantom model design. **b.** Stenotic phantom model examples at different ranges of % diameter stenosis and 2D PC-MRI images in the through-plane (V_z) and in-plane (V_y, V_x) directions (velocity maps, cm/s) for a 45-55% diameter stenosis phantom model. S=Slice number;

3.2.4. Data analysis

All PC-MRI images were directly reconstructed on the MRI scanner. PC-MRI image corrections and NS analysis were performed using a customized MATLAB program (Mathworks, Natick, MA). The resultant image dataset includes: one flow compensated image

and three magnitude image sets and three phase image sets in x, y and z directions, respectively. Image based eddy current corrections were performed in all PC-MRI images prior to NS analysis (77,78).

To calculate the pressure difference (ΔP_{MR}) from PC-MRI, region of interest (ROI)s were first drawn on the magnitude images and mapped onto its corresponding velocity maps to obtain the maximum velocities for NS analysis. Density of fluid and was 1000 kg/m^3 for in vitro ΔP_{MR} estimations. ΔP_{MR} derived using velocity gradients from all three directions (ΔP_{MR}) and from through-plane direction only ($\Delta P_{MR\text{-}Vz}$) were explored. Note that velocities used for $\Delta P_{MR\text{-}Vz}$ calculations were not acquired separately in this study.

To calculate the pressure difference from the pressure transducer (ΔP_{PT}), differences of the recorded pressure values at the two measurement locations (before and after maximum narrowing) were obtained. The %DS of each phantom model was calculated from 3D-FLASH, anatomical, images using the maximum and minimum diameters measured in OsiriX (Pixmeo, Bernex, Switzerland). Reproducibility of the peak velocity and ΔP_{MR} measurements were assessed and the correlation between ΔP_{MR} and ΔP_{PT} and $\Delta P_{MR\text{-}Vz}$ and ΔP_{PT} were evaluated.

3.3 Results

A total of 10-20 cross-sectional slices were acquired for each stenotic phantom. **Table 1** represents the reproducibility of peak velocity and ΔP_{MR} measurements in its %DS groups (1. 35-45%; 2. 45-55%; 3. 55-60%;) and all together.

Stenotic Phantoms (% diameter stenosis)	**Peak Velocity (ICC)**			**ΔP_{MR} (ICC)**
	V_z	**V_x**	**V_y**	
35 - 45 % (n=1)	0.998	0.839	0.868	0.976
45 - 55 % (n=2)	0.999 ± 0.00	0.857 ± 0.05	0.853 ± 0.12	0.964±0.01
55 - 60 % (n=3)	0.950 ± 0.07	0.558 ± 0.10	0.640 ± 0.24	0.859±0.12
All (n = 7)	0.948	0.724	0.731	0.867

Table 1. Intra-class correlation coefficient (ICC) of peak velocities and ΔP_{MR} measurement of the stenotic phantoms.

Overall, excellent ICC was observed in the V_z encoding direction and slightly lower in V_x and V_y. When comparing between %DS groups, peak velocity and ΔP_{MR} measurements showed higher ICCs in the lower %DS groups and relatively lower ICCs as %DS increased. Little bias was observed from the Bland-Altman plots of the peak velocities (**Figure 8a**) and the ΔP_{MR} measurements (**Figure 8b**). An exponential relationship was observed between ΔP_{MR} and %DS (**Figure 8c**). In addition, excellent correlations (R^2 = 0.938 and R^2 = 0.904) were observed between ΔP_{MR} and ΔP_{PT} and $\Delta P_{MR\text{-}Vz}$ and ΔP_{PT}, respectively (**Figure 8d**).

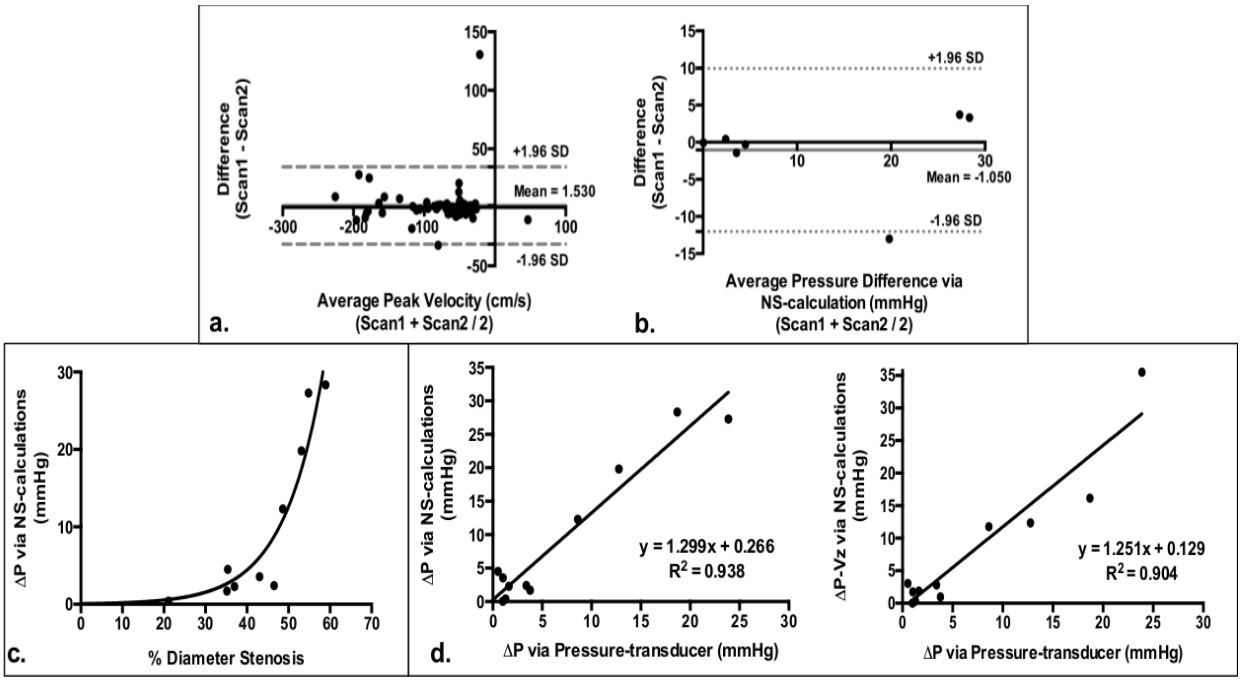

Figure 8. Bland-Altman plots of (**a**) peak velocities (bias of 1.530; 95% CI -31.49 to 34.55) at all cross-sectional slice from repeat PC-MRI scans and (**b**) ΔP_{MR} of the stenotic phantoms (bias of -1.050; 95% CI -12.03 to 9.934). Mean (bias) and 95% confidence interval limits are displayed. **c.** ΔP_{MR} measurement versus % diameter stenosis. An exponential increase in ΔP_{MR} was observed as % diameter stenosis increases. **d.** Comparison between ΔP calculated via NS-equations (ΔP_{MR}) and ΔP measured using pressure transducer (ΔP_{PT}). Excellent correlation (R^2 = 0.94) was observed between the two techniques. Good correlation (R^2 = 0.90) was also observed between ΔP calculated using through-plane velocity gradients only ($\Delta P_{MR\text{-}Vz}$) and ΔP_{PT}.

3.4 Discussion

The phantom analysis in this chapter shows that noninvasive pressure gradient measurement is feasible in a small-caliber flow phantom at various degrees of narrowing in a non-motion, static, case. Phantom results showed a high correlation between ΔP_{MR} and ΔP_{PT} with overall good reproducibility of the peak flow velocity and ΔP_{MR} measurements. ΔP_{MR} derived

using velocity gradients from all three directions (ΔP_{MR}) and from through-plane direction only ($\Delta P_{MR\text{-}Vz}$) were both explored and good correlation was observed in both methods when compared to ΔP_{PT} measured using a pressure transducer. As the phantom is straight, it is expected that in-plane velocities has minimal contribution to the overall pressure gradient estimations.

3.5 Conclusions

We can conclude from this initial phantom study that quantification of ΔP in a small caliber is feasible and pressure gradients estimated noninvasively using PC-MRI correlates well with pressure gradients measured using pressure transducers. This leads us to the next step of implementing the method for in vivo noninvasive pressure gradient estimations. Technical improvements to address both cardiac and respiratory motion in vivo will be further discussed in the next chapter.

CHAPTER 4 – Feasibility of noninvasive pressure gradient measurement in healthy and diseased coronary arteries

4.1 Introduction

Noninvasive pressure gradient measurement has been studied in different sized vessel such as the cardiac chamber (63,66,68,69), aorta (62,65,70,79), carotid (72,73), iliac (73), renal (64), and intracranial (74,75) arteries using PC-MRI in conjunction with the NS analysis. Highly significant correlations (R^2 = 0.91 and R^2 = 0.95) between ΔP derived from PC-MRI and that measured using a pressure wire were found in relatively small and semi-stationary vessels (carotid/iliac (73) and renal (64) arteries, respectively) with ~50-60% DS from previous studies. However, it has not been used in the coronary artery due to the small size and mobility of the vessel.

This chapter will introduce the technical improvements of PC-MRI for coronary artery applications and evaluate the initial feasibility of noninvasive pressure gradient measurement in healthy and diseased coronary arteries. A pilot study was performed in healthy controls and a small cohort of stable CAD patients to evaluate the feasibility of ΔP_{MR} in the coronary arteries. A MR-iFR index, similar to FFR or iFR, was estimated based on ΔP_{MR} to observe the trend of this index in different coronary artery stenosis.

4.2 Methods

4.2.1. Sequence Design

A 2D spoiled gradient recalled echo, PC-MRI sequence with four-point velocity encoding scheme, similar to the stenotic phantoms study in *chapter 3*, was used for image acquisition on a

3.0 T MR system. To minimize cardiac and respiratory motion effects, the acquisition window was limited to diastole and end-expiration using ECG triggering and navigator gating, respectively, as shown in **Figure 9**. To ensure the total acquisition time per cardiac cycle is within the quiescent phase, a view sharing (VS) technique where data were shared between different cardiac phases was implemented (80). Three-directional 2D cross-sectional coronary artery slices, V_x, V_y, V_z at each slice location, were acquired for pressure gradient estimation using NS equations.

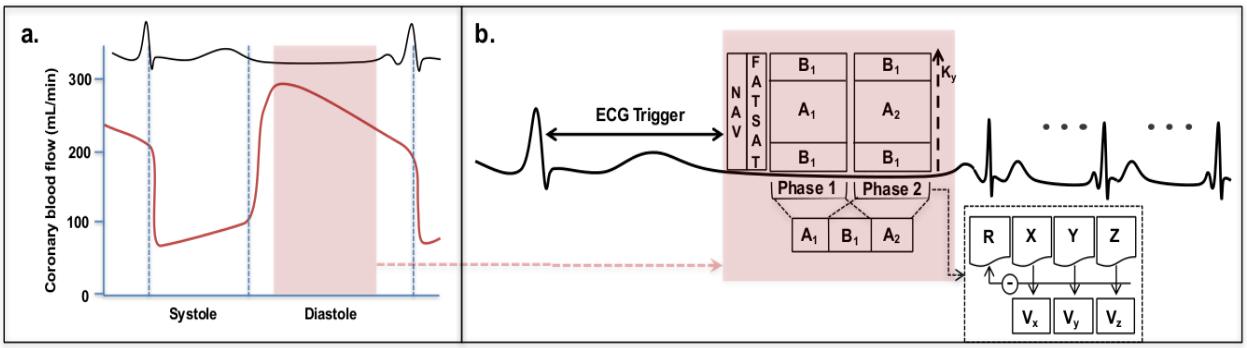

Figure 9. a. Coronary flow timing diagram. Graph from Arthur Guyton et al, *Textbook of Medical Physiology*, (Elsevier Inc. Copyright 2006). Phase-Contrast (PC)-MRI acquisition was obtained during diastole. **b. Sequence Design.** ECG-triggered, navigator-gated, 2D PC-MRI with three-directional velocity encoding (V_x, V_y, V_z). View-sharing was implemented to restrict the acquisition within the quiescent phase, two cardiac phases (phase 1 and phase 2) were obtained. NAV=navigator; FATSAT=fat suppression pre-pulse; B=peripheral k-space (B_1); A=center k-space (A_1 and A_2);

4.2.1. Experiments

To validate the reproducibility and feasibility in healthy coronary arteries, eleven healthy controls (2 females; average age 47.3±14.6 years, group A) were recruited and two repeat PC-

MRI scans were performed to assess reproducibility. Scans were performed on a MAGNETOM Verio 3.0 T MRI system (Siemens Healthcare, Erlangen, Germany) equipped with a 32-channel (Invivo, Gainesville, FL). The intervals between repeat acquisitions were approximately 5 minutes apart to avoid any physiological changes that could potentially alter the velocity measurements. Imaging protocols were: 1) targeted free-breathing contrast enhanced (0.20mmol/kg Gd-BOPTA (MultiHance, Bracco Imaging SpA, Milano, Italy) at 0.30mL/s) 3D-FLASH coronary magnetic resonance angiography (cMRA) for coronary localization, 2) cross-sectional image locations across the coronary segments of interest were obtained using 3D multiplanar reconstruction (MPR) and used for PC-MRI scans, 3) free-breathing 2D coronary PC-MRI with fat-suppression to avoid chemical shift effects and increase vessel contrast (81,82). Approximately 4-9 contiguous PC-MRI imaging slices were consecutively collected across the coronary segment of interest. Imaging parameters were: FOV = $(215 \times 215\ mm)^2$ with 10 - 50% oversampling in the phase-encode, depending on subject size; FA = 15^o; V_{enc} = 35 – 45 cm/s in all 3 orthogonal directions; cardiac phase = 2 (~70 ms/phase); in-plane spatial resolution = $(0.5 - 0.6 \times 0.5 - 0.6\ mm)^2$; slice thickness = 3.2 mm; and time of acquisition = 3-5 mins per image slice.

To test the initial feasibility in diseased coronary arteries, seven patients (3 females; average age 68±7.7 years) with new-onset or recurrent stable chest pain were enrolled. Patient inclusion criteria: patients with 1) known or suspected stable CAD, 2) at least one suspected left coronary artery stenosis at the proximal to middle region detected by CCTA and/or ICA. Patient exclusion criteria: patients with 1) acute coronary syndrome (acute myocardial infarction or unstable angina), 2) previous coronary revascularization (coronary bypass surgery and/or stenting), 3) contradiction to Gadolinium contrast, and 4) non-MRI compatible implants and/or

claustrophobia. One patient was excluded due to poor PC-MRI image quality (limited spatial resolution and minor motion artifact).

Imaging studies and analysis were performed in all six patients. Five of the six patients (group B) have non-obstructive coronary stenosis (3 patients with ICA of <50% DS and 2 patients without ICA has CCTA of <70% DS) and no invasive FFR. One out of six patients has an obstructive (diffused, 50% DS) and functionally significant (FFR = 0.56) coronary stenosis (group C) at the left anterior descending (LAD) coronary artery. CCTA, ICA and FFR (Volcano, CA, USA) measurements of all patients were obtained from their routine clinical records.

Similar imaging protocol and parameters as healthy controls were used. The difference between the two consists of 1) 0.20mmol/kg Gd-DOTA (Dotarem, Guerbet Group, Villepinte, France) at 0.20mL/s, 2) V_{enc} = 35–65 cm/s in 3 orthogonal directions, depending on %DS shown from CCTA and/or cMRA, and/or obtained from a V_{enc} scout, and 3) imaging slices were collected across the stenotic lesion of interest (location matched to invasive catheterization). Scans were performed on a MAGNETOM Trio 3.0 T MRI system (Siemens Healthcare, Erlangen, Germany) equipped with body-matrix coil. PC-MRI reproducibility was not tested, as scan time was limited.

All human studies where approved by the institutional review board (IRB) and written consent was obtained before imaging. All pressure difference estimation was done similarly as the stenotic phantom studies.

4.2.1. Data analysis

All pressure difference estimation was done similarly as the stenotic phantom studies. As coronary flow is phasic, the temporal $[\partial v_i/\partial t]$ component was incorporated. The resultant image dataset includes: one flow compensated image and three magnitude image sets and three

phase image sets in x, y and z directions, respectively, per cardiac phase. A total of two cardiac phases were collected, resulting in a total of 14 images per cross-sectional slice. Similar to stenotic phantom studies, ΔP_{MR} derived using velocity gradients from all three directions (ΔP_{MR}) and from through-plane direction only ($\Delta P_{MR\text{-}Vz}$) were explored. Since the proposed technique is a measure of the relative pressure difference ($\Delta P = P_a - P_d$), when comparing with invasive pressure measurements, a P_a of 74.2 mmHg (83) was used when calculating the MR-index: MR-iFR = $P_d / P_a = (P_a - \Delta P) / P_a$. It is important to note that the proposed technique was acquired at rest and during diastole only, thus more similar to the iFR technique.

Reproducibility of the peak flow velocities was assessed in healthy controls and ΔP_{MR} for both healthy controls and patients were then statistically compared. In addition, MR-iFR index was calculated in all patients. Example cases are described to show the feasibility of the proposed technique.

4.3 Results

A total of 4-9 cross-sectional slices across a coronary segment (healthy controls) or stenotic lesion (patients) were acquired for each subject. In healthy controls (group A), excellent ICCs were observed in the through-plane peak velocities (V_z) (0.94 and 0.95) for cardiac phase 1 and 2 and slightly lower in V_x (0.76 and 0.74) and V_y (0.80 and 0.77), respectively. Reproducibility of the ΔP_{MR} measurement in healthy controls was not assessed as the values were near zero. **Figure 10** shows example cross-sectional images across a total of five imaging slices of a healthy coronary.

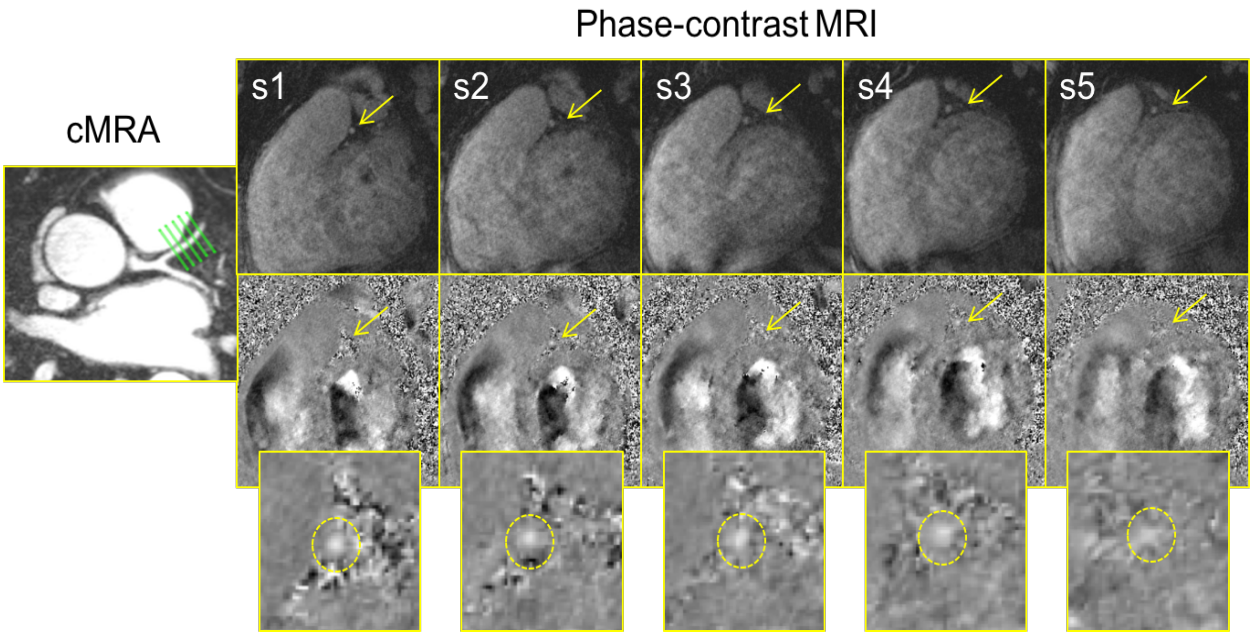

Figure 10. Example images of a healthy subject. Velocity maps in the through-plane direction across a healthy coronary vessel. S = slices; cMRA = coronary magnetic resonance angiography; MRI = magnetic resonance imaging;

When comparing between healthy and diseased coronary arteries, a significant (p=0.025) increase in ΔP_{MR} was seen in the diseased arteries: patient group (6.40±4.43 mmHg) vs. healthy controls (0.70±0.57 mmHg) (**Figure 11**). MR-iFR index of patients and healthy controls were 0.91±0.06 and 0.99±0.01, respectively.

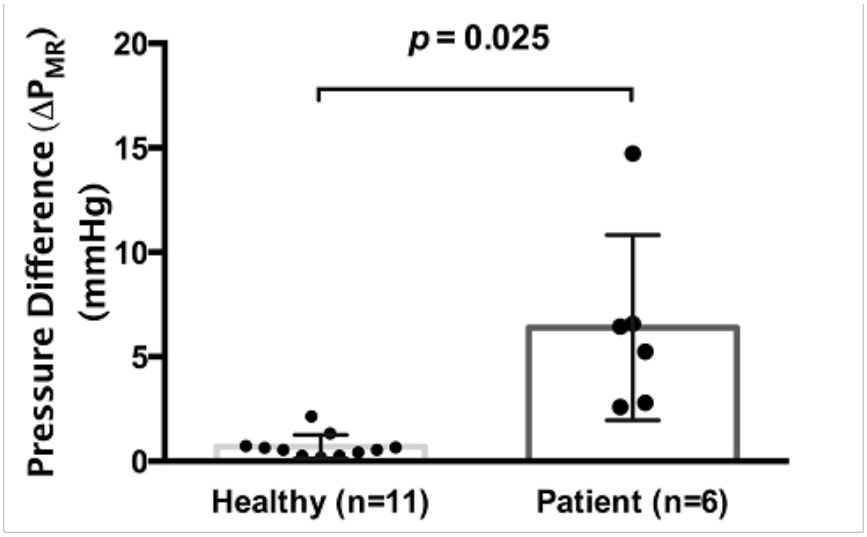

Figure 11. ΔP_{MR} of healthy control and patient groups. A significant (p=0.025) increase in ΔP_{MR} was seen in the patient group (6.40±4.43mmHg) compared against the healthy controls (0.70±0.57mmHg).

Five of the six patients (group B) had non-obstructive coronary stenosis found by CCTA and/or ICA. Relatively small pressure drops or higher MR-iFR index (ΔP_{MR} = 4.73±1.93mmHg or MR-iFR = 0.94±0.03) was observed using the proposed noninvasive pressure gradient measurement method, respectively. Example images from group B are shown in **Figure 12**.

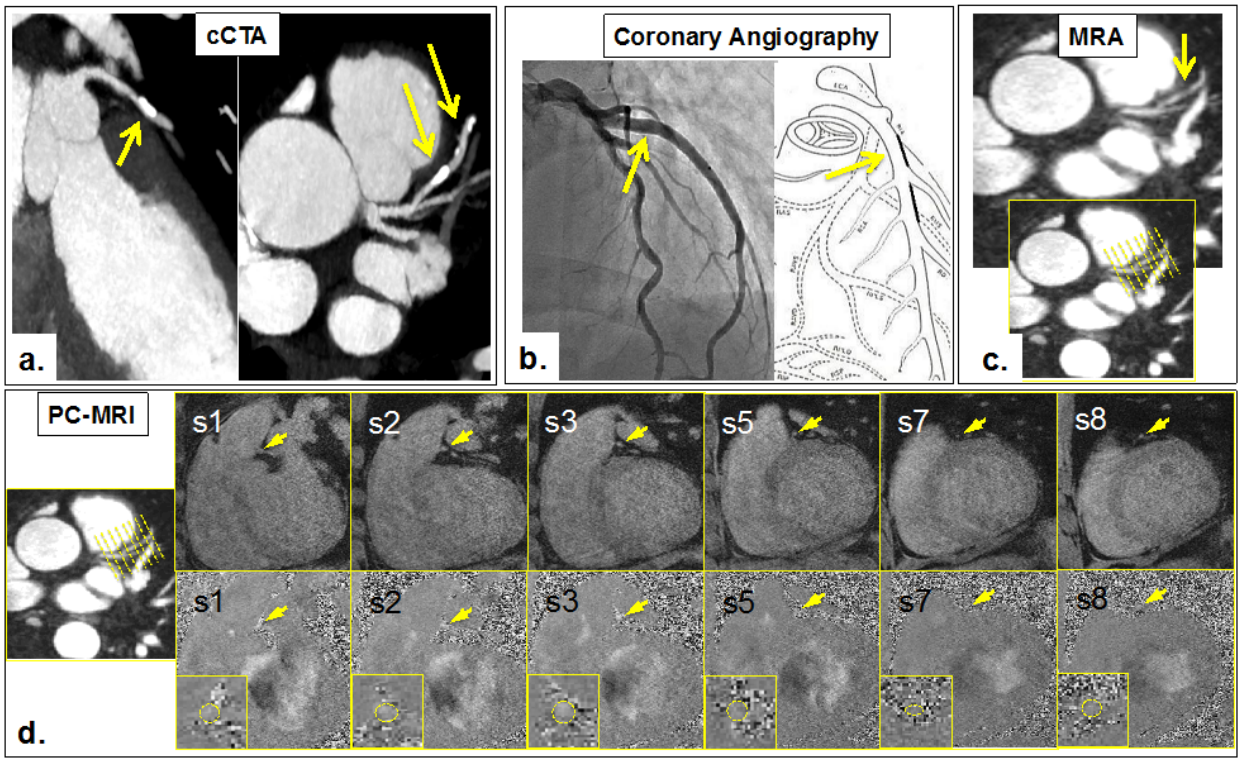

Figure 12. a) Coronary CTA of the proximal left anterior descending (*p*LAD) artery reported as >70% calcified stenosis. **b)** Invasive coronary angiography reported as minimum lumen narrowing (<30% stenosis), non-significant lesion. **c)** Magnetic resonance angiography (MRA) of the *p*LAD. **d)** PC-MRI (8 imaging slices) across the stenotic lesion at the *p*LAD artery. *top row:* flow compensated images, *bottom row:* PC-MRI (velocity map) images represented in the Vz-direction. ΔP_{MR} was approximately 3mmHg or MR-iFR ≈ 0.96. S=Slice number;

One of the six patients (group C) has an obstructive (diffused, 50% DS) and functionally significant (FFR = 0.56) coronary stenosis at pLAD by ICA and invasive FFR, respectively. Relatively high pressure drops or lower MR-iFR index (ΔP_{MR} ≈ 15 mmHg or MR-iFR ≈ 0.80) was observed using the proposed noninvasive pressure gradient measurement method. Example images from group C are shown in **Figure 13**.

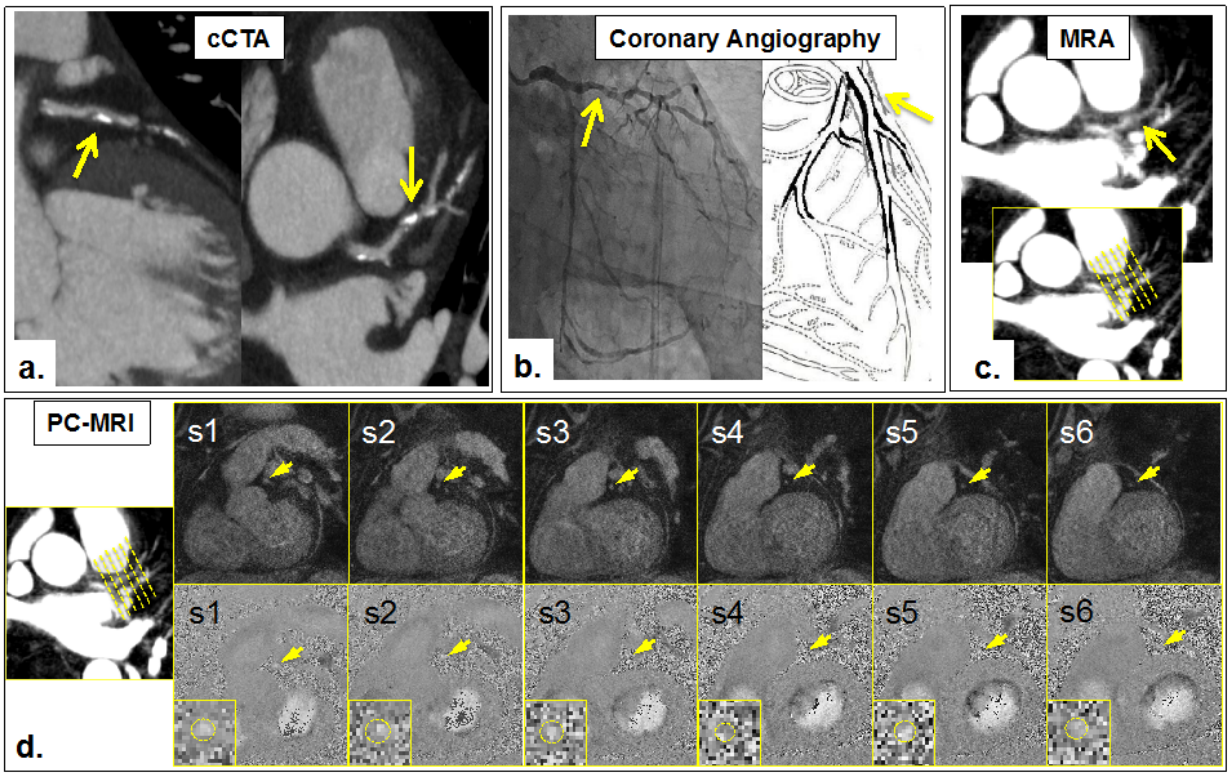

Figure 13. a) Coronary CTA of the proximal left anterior descending (*p*LAD) artery. b) Invasive coronary angiography showing diffused irregular lesion, with 50% lumen narrowing and FFR of 0.56 (functionally significant lesion). c) Magnetic resonance angiography (MRA) of the *p*LAD. d) PC-MRI (6 imaging slices) across the stenotic lesion at the *p*LAD. *top row:* flow compensated images, *bottom row:* PC-MRI (velocity map) images represented in the V_z-direction; ΔP_{MR} was approximately 15 mmHg or MR-iFR ≈ 0.80. S=Slice number;

ΔP_{MR} measurement derived using through-plane velocity gradients only was also explored in both patient groups. A $\Delta P_{MR\text{-}Vz}$ or MR-iFR_{Vz} index of 3.85±1.89mmHg or 0.95±0.03 and ~ 7 mmHg or 0.91 was observed in group B and group C, respectively.

4.4 Discussion

In this work, we have demonstrated the feasibility of a noninvasive blood pressure gradient measurement technique in the coronary arteries using PC-MRI. The proposed method has the advantage of being a noninvasive technique with no ionizing radiation. Human studies have demonstrated the feasibility of velocity and pressure gradient measurements in small sized vessel using PC-MRI and NS analysis, respectively. Human studies demonstrated the feasibility of coronary flow velocity and ΔP_{MR} measurements in both healthy and diseased coronary arteries. In addition, the MR-iFR results across the three groups studied (A: controls, B: patients with non-obstructive coronary stenosis, and C: patient with obstructive and functionally significant stenosis) have shown consistent trends with that of invasive FFR and iFR in literature.

Specifically, in vivo studies showed close to zero ΔP_{MR} or MR-iFR index close to 1 in healthy controls, slight pressure drop (higher ΔP_{MR}, ~4.73 mmHg) or lower MR-iFR index (~0.94) in patients with non-obstructive stenosis, and relatively high ΔP (~15 mmHg) or low MR-iFR index (~0.80) in patient with obstructive and functionally significant stenosis. This trend is consistent with the general tendency of invasive FFR and iFR where healthy coronaries have no significant decline of pressure, FFR or iFR close to 1 (close to zero ΔP) and as the %DS and functional significance of a coronary lesion increases, a lower FFR or iFR value was observed (higher ΔP) (32,37). The lesion is then considered an ischemia inducible stenosis if FFR is ≤ 0.80 (high ΔP) (84) or iFR ≤ 0.89 (9,55-57).

A recent noninvasive technique, FFR_{CT}, has shown promise in deferring patients from unnecessary invasive procedures. However, the technique exposes patients to ionizing radiation. In addition, a small subset of CCTA images suffer from poor image quality for FFR_{CT} analysis partially due to excessive calcium blooming (40), which could potentially be mitigated through

the use of MRI. In one patient case where obstructive coronary artery stenosis (heavy calcification, >70% DS) was initially reported by CCTA; the proposed technique subsequently showed $\Delta P_{MR} \approx 3$ mmHg or MR-iFR ≈ 0.96, suggestive of a low likelihood of a significant stenosis. The discrepancy was then later confirmed by ICA, showing a non-obstructive lesion (<30% DS), confirming the PC-MRI results. A major advantage of MRI is the ability to perform a comprehensive examination of CAD in the same setting. The proposed technique can be potentially combined with MR myocardial perfusion imaging for the assessment of reduced blood flow to myocardium and that caused by a specific coronary stenosis, which could be useful in making treatment decisions. In addition, MRI is a purely noninvasive technique that uses no ionizing radiation or invasive catheterization. This proposed technique could serve as an additional complementary noninvasive functional test that could potentially provide lesion specific diagnosis prior to invasive catheterization. Thus, potentially allow for a more effective risk stratification of patients, better differentiate the patients who would most likely benefit from invasive catheterization and reduce unnecessary invasive procedures (11,12).

In patients, in-plane velocity may have a higher contribution at higher stenotic levels as an approximately 50% underestimation was observed in group C compared to B. However, both in vitro (*chapter 3*) and in vivo (*chapter 4*) studies have demonstrated the potential of using through-plane velocities only, which may allow for shorter scan times. Although underestimation was observed in vivo, a new cut-off value could potentially be established to help determine the functionally severity of a stenosis.

4.5 Conclusions

Our preliminary studies demonstrated the feasibility of a noninvasive pressure gradient measurement in the coronary arteries using PC-MRI. Upon further validation, this approach has

the potential to serve as a gatekeeper to prevent unnecessary invasive catheterization procedures in patients with CAD.

CHAPTER 5 – Feasibility of noninvasive pressure gradient measurement in stable CAD patients using invasive FFR and iFR as references

5.1 Introduction

In patients with suspected or stable CAD undergoing ICA, studies have shown that approximately 50-60% of patients were found to have nonobstructive (<50% diameter stenosis) coronary lesions (11,12). Further, in patients with obstructive coronary lesions who were assessed using FFR, the currently accepted standard for the evaluation of functionally significant stenoses, more than 50% of patients with ≥50% stenosis had normal FFR (>0.80) (13). Such low diagnostic yields indicate poor selection of patients for invasive catheterization, and the unnecessary invasive procedures (ICA, FFR) may lead to potential complications and high costs. A recently developed physiological index for the evaluation of functionally significant stenoses, instantaneous wave-free ratio (iFR), derived from pressure measurements at rest has shown to be non-inferior to FFR as an adenosine-free guide for coronary revascularization (9,10). Although the technique may reduce the risks and costs associated with adenosine, the procedure remains invasive. Therefore, noninvasive tests for the assessment of patients with suspected CAD which could predict invasive FFR or iFR measurements would be useful in guiding patient management (26).

Noninvasive imaging techniques have been used extensively in the diagnosis of CAD. Techniques such as echocardiography, single photon emission computed tomography (SPECT) and positron emission tomography (PET), cardiac magnetic resonance (CMR), and coronary

computed tomographic angiography (CTA) have been used in routine clinical procedures to assess myocardial perfusion or wall motion abnormalities or directly detect coronary luminal narrowing (85). SPECT, PET, and CMR techniques mainly focus on myocardial perfusion defects to assess the extent of myocardial ischemia (86,87). However, identification of ischemia inducing coronary lesions on a per vessel basis, could provide added information to the overall diagnosis and management strategies of CAD (26). Recently, an emerging noninvasive imaging method using coronary computed tomographic angiography (CTA) in combination with computational fluid dynamics simulations, FFR_{CT}, has shown promise in the diagnosis of CAD by estimating the functional significance of coronary artery lesions on a per vessel basis (14). However, the method requires the exposure to ionizing radiation and may be hindered by blooming artifacts caused by densely calcified plaques that could reduce the accuracy of detection of coronary stenosis, a necessary component of FFR_{CT} assessment.

More recently, a novel noninvasive method using phase-contrast magnetic resonance imaging (PC-MRI) in conjunction with Navier-Stokes analysis to derive a physiological index (MR–Instantaneous wave Free Ratio, MR-iFR) for the assessment of the functional significance of coronary lesions has shown initial feasibility in phantoms, healthy subjects and a few stable CAD patients (88). The technique is a surrogate of iFR, where measurements were obtained during diastole without adenosine (37). The MR-iFR technique has the advantage of no ionizing radiation, allows longitudinal monitoring of patients, and could be utilized in conjunction with other CMR protocols to provide complimentary information to existing techniques such as MR perfusion imaging.

This chapter introduces the initial findings of the feasibility of the proposed noninvasive pressure gradient measurement method in a small cohort of stable CAD patients. The

noninvasive physiological index, MR-iFR, was obtained and compared to gold-standard invasive indices, FFR and iFR.

5.2 Methods

5.2.1. Study population

Patients with stable angina were screened for enrollment of this study. Inclusion criteria were 1) age ≥ 18 years, and 2) patients undergoing clinically indicated non-emergent ICA (4,7,64,73-75). Exclusion criteria included patients with: 1) known myocardial infarction, 2) previous coronary revascularization (percutaneous coronary intervention and/or coronary artery bypass graft), 3) contradiction to gadolinium-based contrast media, and 4) non-MRI compatible implants and/or claustrophobia. Coronary CTA and MR-iFR scans were performed < 60 days before invasive catheterization procedures (ICA, FFR, and/or revascularization) in enrolled patients. The study protocol was approved by the institutional review board and written consent was obtained before enrollment in the study.

5.2.1. Study design

This study aimed to evaluate the feasibility of the proposed MR-iFR technique in stable CAD patients and its association with invasive FFR and iFR measurements. Overall study flow was as described below. All patients had MR-iFR, coronary CTA, ICA, and invasive FFR and iFR assessments. First, coronary CTA images were obtained based on routine clinical protocol. Second, MR imaging was performed. Specifically, a three-dimensional (3D) coronary MR angiography (MRA) scan was first performed for coronary localization followed by multiple two-dimensional (2D) cross-sectional PC-MRI scans covering the coronary lesion of interest. Coronary velocity maps from PC-MRI were then used for MR-iFR calculation. Lastly, invasive catheterization (ICA and/or FFR) was performed within 60 days of the MR-iFR and coronary

CTA scans, based on routine clinical procedures by physicians blinded to the result of MR-iFR and coronary CTA.

All the above data were then filtered where patients with 1) ≥ 1 suspected left anterior descending (LAD) stenosis ≤ 70% in the proximal and/or middle coronary segment by visual assessment based on ICA and 2) MR imaging anatomically corresponding to the measured invasive FFR locations were included for analysis. Specific patient characteristics are summarized in **Table 2**.

	All patients (n=24)	FFR > 0.80 (n=21)	FFR ≤ 0.80 (n=3)	p value
Age, yrs	63 ± 9.4	63 ± 9.7	66 ± 7.2	1.00
Male, n (%)	17 (71%)	16 (76%)	1 (33%)	0.56
BMI, kg/m^2	25.5 ± 2.6	25.8 ± 2.7	23.5 ± 0.8	1.00
Diabetes Mellitus, n (%)	8 (33%)	6 (29%)	2 (67%)	0.16
Dyslipidemia, n (%)	4 (17%)	4 (19%)	0 (0%)	0.32
Hypertension, n (%)	15 (63%)	14 (67%)	1 (33%)	0.56
Past Tobacco use	8 (33%)	6 (29%)	2 (67%)	0.16
Current Tobacco use	2 (8.3%)	2 (9.5%)	0 (0%)	1.00
Heart rate, beats/min	69 ± 7.7	69.3 ± 7.3	67 ± 12.1	0.59
Medications, n (%)				
Aspirin	21 (88%)	18 (86%)	3 (100%)	1.00
Beta-blocker	11 (46%)	8 (38%)	3 (100%)	0.16
Statin	18 (75%)	16 (76%)	2 (67%)	0.32

Table 2. Patient Characteristics; Values are mean ± standard deviation or (%); BMI = body mass index; FFR = fractional flow reserve, iFR = instantaneous wave-free ratio; MR-iFR = magnetic resonance instantaneous wave-free ratio.

5.2.1. MR-iFR protocol

The proposed MR-iFR technique consists of the steps shown in **Figure 14**. Briefly, 3D coronary MRA was first obtained for coronary localization followed by consecutive cross-sectional 2D PC-MRI image acquisitions along a coronary lesion of interest. All PC-MRI images were reconstructed directly on the MR scanner. Total MR scan time was approximately one hour. Velocity maps (Vz, Vx, and Vy at two cardiac phases for all cross-sectional slices) obtained from PC-MRI were then used in the Navier-Stokes analysis to derive the pressure difference (ΔP) across the coronary lesion. In this study, aortic pressure (P_a) was obtained from invasive pressure measurements as the noninvasive pressure measurement device was not available at the time of the study. MR-iFR was then calculated as $(P_a - \Delta P) / P_a$. MR-iFR calculations were performed using a customized MATLAB program (The Mathworks, Inc., Natick, MA, USA), blinded to the results of invasive FFR and iFR measurements. In addition, a MR-iFR-vz measurement was also calculated using z-directional velocity maps only to assess the feasibility of the method to

potentially decrease MR image acquisition time.

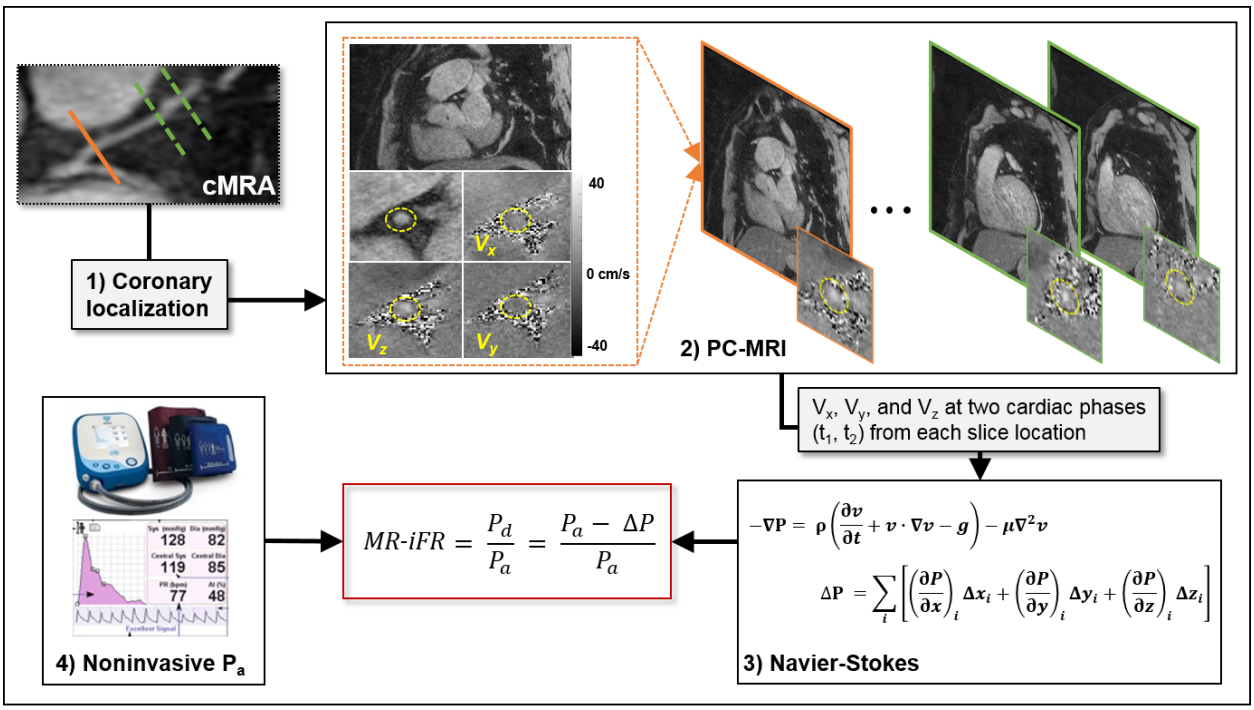

Figure 14. Simplified flow chart to obtain the MR-iFR index. 1) Coronary localization using images obtained from coronary MRA, followed by 2) 2D cross-sectional PC-MRI scans across the coronary segment of interest. Velocity maps in three orthogonal directions (Vx, Vy, Vz) at two cardiac phases was then used for 3) Navier-Stokes analysis to obtain the pressure difference (ΔP) across the vessel segment. Pa could then be obtained using an external aortic pressure device. ΔP and Pa could then be used for MR-iFR calculation. Orange and green lines in the cMRA images correspond to the slice locations of the PC-MRI scans. Yellow circles highlight the location of the coronary artery in the cross-sectional view. MRA = magnetic resonance angiography, PC-MRI = phase-contrast magnetic resonance imaging, Pa = aortic pressure.

5.2.1. Invasive catheterization (ICA, FFR, and iFR) protocol

Stenosis levels from ICA were determined by visual estimation at the time of the procedure by the interventionalists. FFR is defined as the ratio of distal coronary pressure (P_d)

over aortic pressure (P_a) measured under maximal hyperemia (46). iFR is defined as the resting pressure ratio between P_d and P_a measured during the part of diastole where microvascular resistance is low and stable (9,10,64,76). Pressure measurements were obtained using standard FFR (Volcano Inc., Rancho Cordova, CA, USA and St Jude Medical Inc., Little Canada, MN, USA) systems during ICA. Maximal hyperemia was induced by intravenously administered adenosine at the dose of 140 μg/kg/min. Rest and stress pressure curves were obtained. FFR values were obtained directly from the system console during maximal hyperemia. iFR values were calculated offline using the resting pressure curves obtained during the pressure measurement procedures. Calculations were done using a MATLAB program based on methods described by Sen et al. (37). FFR ≤ 0.80 or iFR ≤ 0.89 were used to define a hemodynamically significant stenosis (9,10,46).

5.3 Results

Among 28 patients who met the inclusion criteria, 4 patients (14.3%) were excluded from analysis due to poor image quality caused by cardiac and/or respiratory motion during the PC-MRI scans. Among the 24 patients, the interval between the proposed MR-iFR and invasive catheterization (ICA and/or FFR and iFR) was 4.08 ± 4.27 days (range between 0 to 20 days) and between the proposed MR-iFR and coronary CTA was 15.50 ± 13.22 days (range between 0 to 45 days). Coronary CTA of these patients showed lumen stenosis ranging from normal (no lumen stenosis) to severe (70-99% stenosis). 12 (50%) had obstructive (≥50%) stenosis based on ICA, 19 (79.2%) had obstructive stenosis based on coronary CTA, three (12.5%) had functionally significant stenosis (FFR ≤ 0.80) based on FFR, and five (20.8%) had functionally significant stenosis (iFR ≤ 0.89) based on iFR.

Figure 15 shows a representative case of a patient with suspected CAD and lesion-specific ischemia. Coronary CTA showed a severe stenosis (70-99%) of the proximal LAD and moderate stenosis (40-69%) at the middle LAD. Invasive catheterization showed a diffuse (65% lumen narrowing) and functionally significant (FFR = 0.75) lesion across the proximal to middle LAD. The proposed MR technique showed a pressure difference (ΔP) of approximately 12 mmHg, MR-iFR of 0.82 and MR-iFR-vz of 0.85 across the lesion.

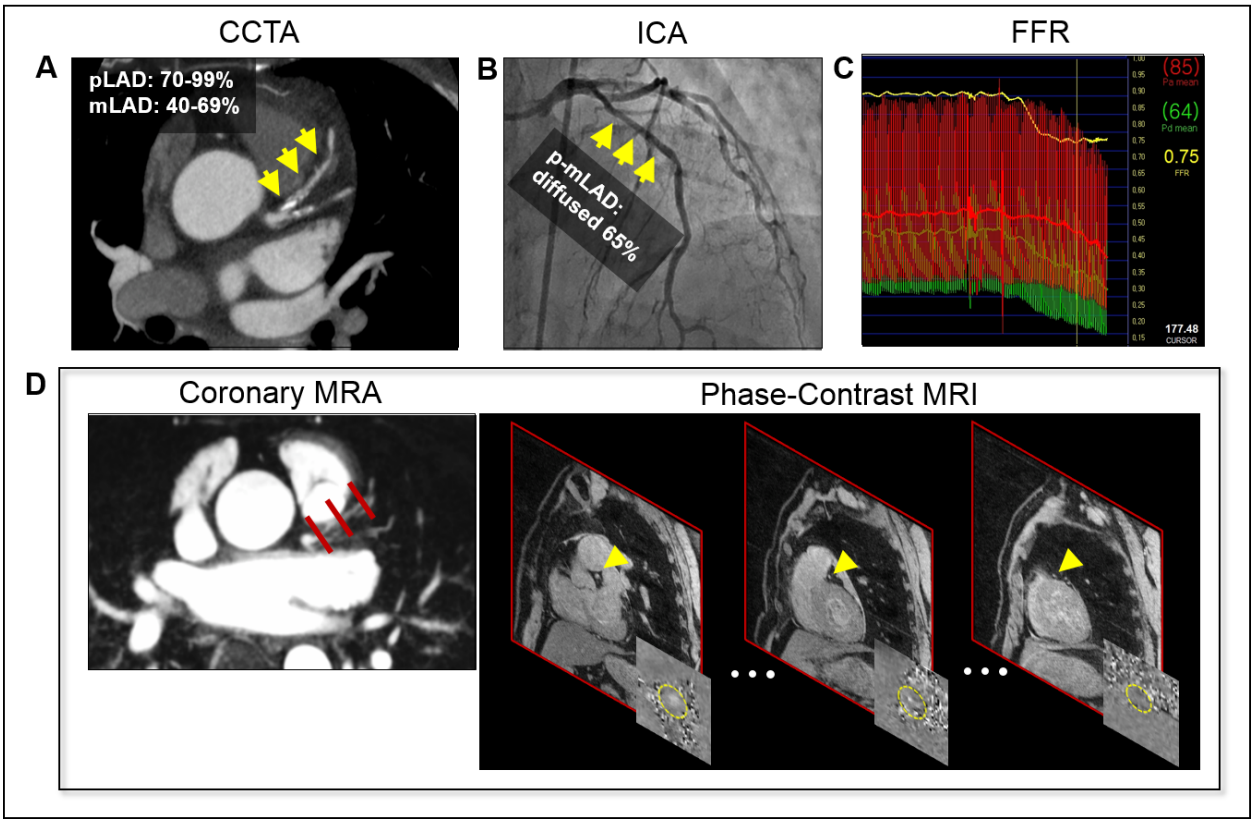

Figure 15. Example results of a 71-year-old woman with suspected CAD and lesion-specific ischemia. (A) Coronary computed tomography angiography. (B) Invasive coronary angiography. (C) Fractional flow reserve. (D) Coronary MRA and phase-contrast MRI images of the same LAD segment. Arrows are pointed to the stenotic lesion, which corresponds between different imaging techniques. CAD = coronary artery disease, LAD = left anterior descending, MRI =

magnetic resonance imaging, MRA = magnetic resonance angiography, mLAD = middle left anterior descending, pLAD = proximal left anterior descending.

Figure 16 shows the correlation between MR-iFR and invasive FFR and invasive iFR. Good correlation was found between MR-iFR and invasive FFR (r=0.701, *p=0.0001*), as well as MR-iFR and invasive iFR (r=0.698, *p=0.0001*). Similarly, good correlation was observed when comparing between MR-iFR-vz and invasive FFR (r=0.832, *p<0.0001*) and MR-iFR-vz and invasive iFR (r=0.680, *p=0.0003*).

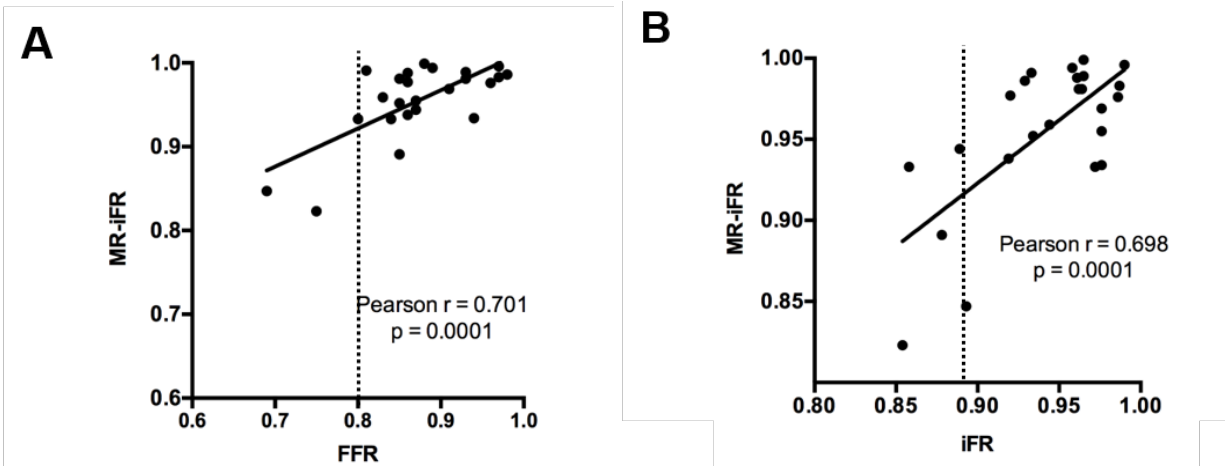

Figure 16. Analysis of correlation between FFR and iFR and MR-iFR. (A) Correlation between invasive FFR and MR-iFR. (B) Correlation between invasive iFR and MR-iFR; FFR = fractional flow reserve, iFR = instantaneous wave-free ratio, MR-iFR = magnetic resonance instantaneous wave-free ratio

Figure 17. shows the Bland-Altman analysis between MR-iFR and invasive FFR and iFR. Small bias was observed when comparing between MR-iFR and invasive FFR (bias = 0.08±0.05), as well as between MR-iFR and invasive iFR (bias: 0.01±0.03). Similar results were found when

comparing between MR-iFR-vz and invasive FFR (bias = 0.09±0.05) and MR-iFR-vz and invasive iFR (bias = 0.02±0.03).

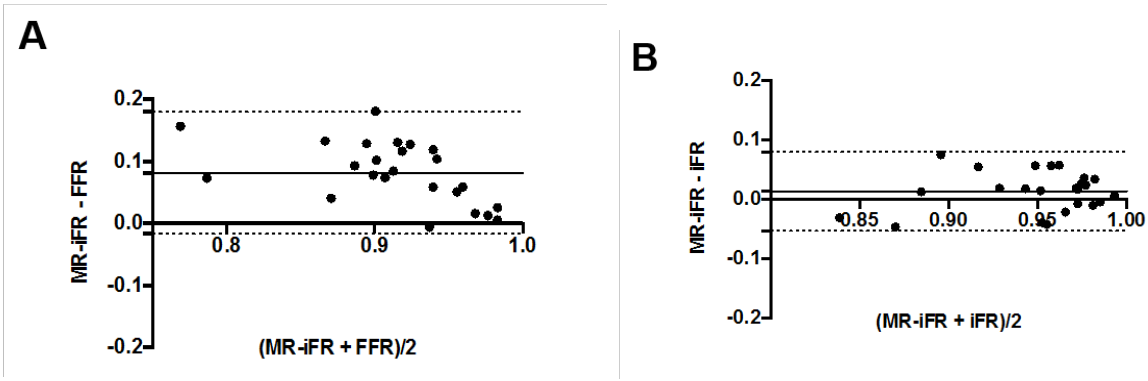

Figure 17. Bland-Altman analysis of FFR and iFR and MR-iFR. Bland-Altman plots of differences against the means of (A) MR-iFR versus invasive FFR and (B) MR-iFR versus invasive iFR. The mean bias is represented by the solid line (with 95% confidence interval represented by the dashed lines); FFR = fractional flow reserve, iFR = instantaneous wave-free ratio, MR-iFR = magnetic resonance instantaneous wave-free ratio

Using invasive FFR cut-off of 0.80 as reference, various MR-iFR cut-off values could be obtained. To optimize sensitivity, a MR-iFR cut-off of 0.93 results in a sensitivity, specificity, positive predictive value (PPV), and negative predictive value (NPV) of 100%, 85.71%, 50%, and 100%, respectively. To optimize specificity, a MR-iFR cut-off of 0.87 results in a sensitivity, specificity, PPV, and NPV of 66.67%, 100%, 100%, and 95.45%, respectively. If a MR-iFR cut-off of 0.89 (similar cutoff as invasive iFR) was used, the sensitivity, specificity, PPV, and NPV were 66.67%, 95.24%, 66.67%, and 95.24%, respectively.

Using invasive iFR cut-off of 0.89 as a reference, similarly, various MR-iFR cut-off values could be obtained. To optimize sensitivity, a MR-iFR cut-off of 0.95 results in a sensitivity, specificity, PPV, NPV of 100%, 78.95%, 55.56%, and 100%, respectively. To

optimize specificity, a MR-iFR cut-off of 0.91 results in a sensitivity, specificity, PPV, NPV of 60%, 100%, 100%, and 90.48%, respectively. If a MR-iFR cut-off of 0.89 was used, sensitivity, specificity, PPV, NPV of 40%, 100%, 100%, and 86.36% was observed, respectively.

5.4 Discussion

In this initial patient study, we have demonstrated the feasibility of a noninvasive imaging technique, MR-iFR, in patients with stable CAD. Preliminary comparison with invasive FFR and iFR has shown good correlation, high specificity and high NPV, suggesting the potential of the technique to serve as a gatekeeper for unnecessary invasive catheterization in patients with stable CAD. The proposed technique has the advantage of being noninvasive, comprising of no ionizing radiation, and could potentially serve as a complementary approach to current clinical diagnostic tools, providing added information to potentially allow for better risk-stratify and triage patients. To best of the authors' knowledge, this is the first patient study demonstrating the feasibility of MR-iFR in diseased coronary arteries.

FFR is the current accepted standard to assess the functional severity of coronary stenosis and guide coronary revascularization in patients with CAD. Many clinical studies have shown the advantage of the technique in identifying lesion-specific ischemia and in improving clinical outcomes (89,90). Recently, studies by Davies et al. (10) and Gotberg et al. demonstrated the potential of an adenosine-free technique, iFR, in the diagnosis of coronary hemodynamics and showed that iFR-guided coronary revascularization was non-inferior to FFR-guided revascularization. This suggests that the use of iFR may result in outcomes similar to those associated with FFR. However, both FFR and iFR techniques are invasive procedures associated with potential complications (91) A noninvasive FFR or iFR technique could help defer patients who would most likely not benefit from revascularization. For example, the Fractional flow

reserve versus Angiography in Multivessel Evaluation (FAME) study has showed that 65% of stenosis with angiography severity of 50% to 70% were found functionally nonsignificant (FFR>0.80) (13), suggesting that these patients could potentially be deferred from invasive procedures. This MR-iFR study focused on patients with angiography severity of ≤70% with approximately half of the patients with intermediate (50-70%) stenosis. The high specificity and NPV observed in this study demonstrates the potential of the MR-iFR technique in identifying patients with functionally nonsignificant stenosis, which may allow for better stratification of patients who wouldn't benefit from invasive catheterization because of a low likelihood of needing revascularization.

An emerging noninvasive technique, FFR_{CT}, has shown promise for the diagnosis of patients with stable angina. Recent results showed that care guided by coronary CTA and selective FFR_{CT} has equivalent clinical outcome and quality of life, lower rate of ICA, and lower costs when compared to usual care (14,40,92). However, the technique involves ionizing radiation and is susceptible to calcification-related blooming artifacts. The proposed MR-iFR could potentially be performed in patients, in whom FFR_{CT} could be inaccurate due to blooming artifacts, and provide added value to overall patient management.

PC-MRI directly measures blood flow velocity and its usage for pressure difference (ΔP) calculations has been studied in applications such as atherosclerosis in the renal (64) and carotid (73) arteries. Studies have shown highly significant correlations (renal: r=0.98; carotid: r=0.89) between ΔP derived noninvasively using MRI and invasively using pressure transducers. In this study, we used a similar technique to demonstrate the feasibility of measuring pressure gradients in patients with coronary artery disease. MR-iFR derived using velocity maps from all three directions (MR-iFR) and from through-plane direction only (MR-iFR-vz) were respectively

compared to invasive FFR and iFR. Good correlation was observed between MR-iFR, and invasive FFR (r=0.701), and invasive iFR (r=0.698). Similar correlation was observed when comparing between MR-iFR-vz and invasive iFR (r=0.680). Interestingly, slightly higher correlation was observed when comparing between MR-iFR-vz and invasive FFR (r=0.832), suggesting the potential of using through-plane velocity (Vz) derived MR-iFR for estimating FFR. The success of using only Vz may allow for up to approximately 50% reduction of scan time or higher spatial or temporal resolution, which could improve image quality or scan success rate.

Furthermore, the proposed MR-iFR technique could be combined with other noninvasive MR tests where cardiac anatomy, function and myocardial structure could be obtained in one single imaging session, achieving a one-stop-shop cardiac examination. A recent study using MR myocardial perfusion imaging has shown promise as a noninvasive management strategy for patients with stable angina. Preliminary results showed that MR perfusion imaging is non-inferior to invasive angiography supported by FFR in a 1-year outcome study, suggesting the potential of the technique to guide patient management
(39,93). The proposed MR-iFR technique has the potential of identifying lesion-specific ischemia, thus could especially be beneficial to serve as an integrated approach with MR myocardial perfusion imaging. A combined approach could potentially help identify ischemia both from the vessel lesion itself and the reduced flow to the myocardium. In addition, recent studies have shown that coronary plaque characteristics observed using T1-weighted (T1w) CMR may be associated with high risk of coronary events (72,73,94). An integrated anatomical (T1w CMR) and functional (MR-iFR) assessment of vessel-specific ischemia could also be valuable for the diagnostics of CAD.

5.5 Conclusions

In this work, we have demonstrated the feasibility of the noninvasive imaging technique, MR-iFR, in a small cohort of stable CAD patients. The preliminary comparison with invasive FFR and iFR showed the potential of the proposed technique to serve as a gatekeeper for more effective risk stratification of patients who would most likely benefit from invasive catheterization.

CHAPTER 6 – Accelerated coronary 4D-Flow using stack-of-stars sampling and compressed sensing reconstruction

6.1 Introduction

Chapters 3-5 introduced an overall noninvasive pressure gradient measurement framework and showed the feasibility of the method in stenotic flow phantoms, healthy subjects and a small cohort of stable CAD patients. One major drawback of the technique is its long scan times. The previously introduced Cartesian method requires approximately 30-40 minutes to obtain the necessary number of cross-sectional images for Navier-Stokes analysis, which hinders the translation of the method into a clinical setting. This chapter introduces an accelerated imaging approach using stack-of-stars (radial in-plane and Cartesian through-plane) sampling and compressed sensing reconstruction to potentially achieve accelerated PC-MRI acquisition in the overall framework of noninvasive pressure gradient measurements.

Radial sampling methods such as stack-of-stars acquisition and 3D radial acquisitions have shown promise in decreasing scan time for large to medium sized motion-induced vessels and various types of stationary vessels
(64,74,75,95,96). As the proposed framework focuses only on the coronary vessel, a stack-of-stars approach was chosen where it has the freedom to choose any arbitrary vessel segments of interest for image acquisition. Imaging reconstruction methods such as parallel imaging (SENSE, SENSitivity Encoding, and GRAPPA, GeneRalized Autocalibrating Partially Parallel Acquisitions), compressed sensing, and low-rank modeling has also shown promise to achieve accelerated imaging(97-101). The proposed approach explores a combined SENSE and

compressed sensing approach for image reconstruction to potentially achieve accelerated imaging.

The initial feasibility of the proposed method is evaluated in stenotic flow phantoms at various degrees of narrowing and in the healthy coronary arteries, using Cartesian acquisition as reference. The goal was to develop a more clinically feasible noninvasive pressure gradient measurement method for the assessment of CAD.

6.2 Methods

6.2.1. Sequence Design

A spoiled gradient recalled echo, PC-MRI, sequence with stack-of-stars sampling (i.e. radial in the k_x-k_y plane and Cartesian in the k_z plane) was implemented on a 3.0 T MR system (SKYRA, Siemens) with a conventional four-point velocity-encoding scheme (reference, x, y, z) (76). In-plane *k*-space was filled using radial golden angle trajectories(102) as it's more suited for arbitrary retrospective data sorting, able to combine with sparse MRI reconstruction methods due to incoherent aliasing artifacts(103), and it has relatively low sensitivity to motion(104). Each velocity-encoding set (reference, x, y, z) was acquired with the same sampling angle. In the partition, *kz*, direction, a random Cartesian sampling pattern was achieved to further induce an incoherent undersampling artifact pattern. Water-excitation pulse was implemented to suppress fat surrounding the coronary arteries to avoid chemical shift effects and increase vessel contrast (81,82). In addition, fat suppression could also allow for less streaking artifacts from the contribution of fat signals in the back and chest-wall regions in the overall image. To ensure minimal cardiac and respiratory motion in the coronary arteries, ECG-triggering to diastole and navigator-gating to end-expiration was implemented, respectively.

6.2.2. Image Reconstruction

Image reconstruction was done individually for each velocity encoding direction (reference, x, y, and z) and each cardiac phase. Gradient delay correction was first performed by determining the shift between the closest two opposite trajectories. Coil compression was performed by combining the receiver channels into eigenmodes, removing higher-order modes such that 99% RMS signal was preserved (105). Coil sensitivity maps were computed from flow compensated (reference) encoding dataset only and applied to other encoding directions. Fast Fourier transform (FFT) was applied along the k_z dimension. Compressed sensing reconstruction is solved using the equation below(106):

$$d = \arg\min \{\|FSd - m\|_2^2 + \lambda \|Td\|_1\} \qquad (6-1)$$

where d contains the images, F is the non-uniform fast Fourier Transform (NUFFT) operator, S is the coil sensitivity operator, m is the measured k-space data, λ is the regularization term. T could be any sparsity transform, in this case, a 4-level 3D Daubechies-4 wavelet transform was used. λ was chosen empirically as 5e-11 for all reconstructions. Phase maps of the reconstructed images were then converted to velocity maps based on the prescribed velocity encoding (VENC).

6.2.3. Experiments

Stack-of-stars and Cartesian PC-MRI methods were first compared in a stenotic flow phantom with a constant volume velocity of 250 mL/min and reference diameter of 4.8 mm. Various stenotic narrowing was assessed, spanning from approximately 0% to 50% diameter stenosis. Specifically, a total of 5 stenotic flow phantoms were assessed: 0% (n=1) 30-40% (n=2), and 40-50% (n=2).

The imaging work flow include: 1) a 3D-FLASH coronary magnetic resonance angiography (cMRA) was first obtained for anatomic localization and for determining the stenotic level of the phantoms. 2) stack-of-stars PC-MRI and Cartesian PC-MRI data were then acquired in arbitrary order. Shared imaging parameters between stack-of-stars and Cartesian PC-MRI were: FA = 15°; spatial resolution = 0.5 x 0.5 x 3.2 mm^3; FOV = 220 x 220 mm^2; Matrix = 448 x 448; VENC = 70 - 110 cm/s depending on the degree of narrowing; Partitions = 10 imaging slices; Slice oversampling = 25%; For Cartesian acquisition, an iPAT factor of 2 was used, giving a 3D image set with approximately 2500 total imaging lines per velocity encoding, per cardiac phase. For stack-of-stars acquisition, 2500 radial projections were used as the maximally sampled reference, matching to the similar number of imaging lines as Cartesian acquisition, for comparison. **Figure 18** shows an example phantom set up for a ~50% stenotic phantom.

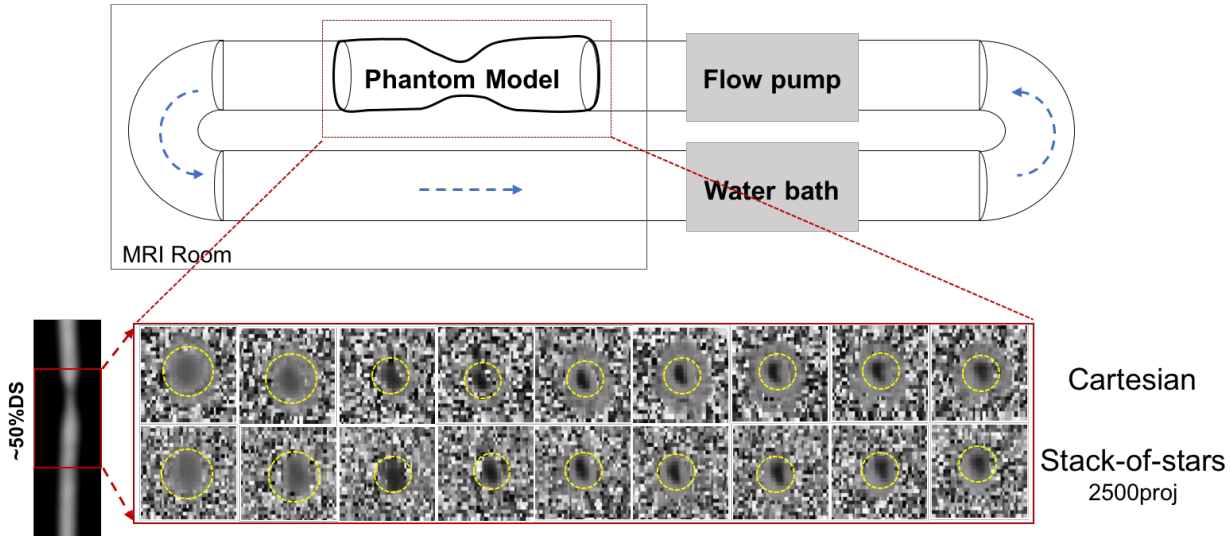

Figure 18. Example phantom set-up for a ~50% diameter narrowing. A flow pump was used to circulate flowing water at a constant flow rate of 250mL/min in a 4.8-mm reference diameter

tubing. Coronary MRA was first obtained followed by Cartesian and stack-of-stars 4D-flow in arbitrary order.

To simulate an *in vivo* environment, a simulated ECG with 60 beats per minute (bpm) was used during acquisition. Data acquisition was triggered to diastole where 2 segments were collected per cardiac phase for both Cartesian and stack-of-stars methods, resulting in an approximately 22-minute scan time for each imaging acquisition. To evaluate the effect of the number of projections on the stack-of-stars image quality, retrospective undersampling was achieved by discarding the sampled data after N_i number of projections. As an initial test, retrospective undersampled images for N_i of 2000, 1500, 1000, and 500 imaging lines from a total of 2500 imaging lines were performed and compared to the Cartesian images.

Stack-of-stars and Cartesian PC-MRI methods were also compared in three healthy subjects (average age of 40.7±17.9 yrs, 2 females). Similar imaging parameters were used as *in vitro* studies. Some differences may include: spatial resolution = 0.6 x 0.6 x 3.2 mm^3; Matrix = 368 x 368; Partition = 8 imaging slices; VENC = 45 cm/s in all three orthogonal directions; Cardiac phase = 2 (~ 70.4 ms / cardiac phase); 3D-FLASH cMRA was performed prior to PC-MRI for coronary localization. An abdominal belt was used in all subjects to ensure minimal respiratory motion, therefore giving a higher navigator acceptance rate. For Cartesian acquisition, an iPAT factor of 2 was used, resulting in approximately 1800 imaging lines per 3D image set. Due to limited scan time for *in vivo* studies, a total of approximately 1200 imaging lines (~1.5x undersampling compared to Cartesian) were collected per velocity encoding, per cardiac phase for stack-of-stars acquisition. Similar retrospective undersampling experiment as *in vitro* studies was performed where retrospective undersampled images for N_i of 1000 and 800

imaging lines from a total of 1200 imaging lines were performed and compared to the Cartesian images.

6.2.4. Data Analysis

SENSE and compressed sensing image reconstruction was implemented offline using MATLAB (Mathworks, Natick, MA). All parameters for image reconstruction were kept constant for all *in vitro* and *in vivo* studies. Eddy current correction was performed in all stack-of-stars and Cartesian PC-MRI images prior to image analysis (77,78). Region of interest (ROI)s were first drawn on the magnitude images and mapped onto its corresponding velocity images to obtain the maximum and mean velocities. In cases where ROIs weren't clear on the magnitude images, velocity maps where used for direct analysis.

For the stack-of-stars PC-MRI method, retrospective undersampling of 2500, 2000, 1500, 1000, and 500 imaging lines were assessed for *in vitro* studies and 1200, 1000, and 800 imaging lines were assessed for *in vivo* studies. All reconstructed images were compared to the collected Cartesian PC-MRI images to assess the feasibility of the stack-of-stars method.

Peak and mean velocities across all imaging slices were compared between stack-of-stars and Cartesian PC-MRI methods in both *in vitro* and *in vivo* experiments. Cross-correlation and Bland-Altman analysis in the maximum velocities across all imaging slices was performed for a range of stack-of-stars projections versus Cartesian.

6.3 Results

Good cross-correlation of up to 2.5x undersampling, 0.95 and 0.93, was preserved in the peak and average velocities, respectively, as stack-of-stars projection number decreased (

Table 3 and **Table 4**).

Figure 19 shows the peak velocity values from data acquired using various stack-of-stars undersampling factors and Cartesian across each imaging slice in various degrees of stenotic phantoms. Similar maximum velocities across each imaging slice were observed between the stack-of-stars and Cartesian methods.

Peak velocities (z-direction) Cross-correlation (CC)	**Projections (undersampling factor)**				
	2500	2000 (1.25x)	1500 (1.7x)	1000 (2.5x)	500 (5x)
30-40% narrowing (n=2)	0.95±0.02	0.95±0.01	0.95±0.01	0.93±0.03	0.83±0.03
40-50% narrowing (n=2)	0.94±0.05	0.93±0.03	0.93±0.03	0.91±±0.04	0.82±0.07
All (n=5)	0.966	0.959	0.958	0.951	0.898
nRMSE (n=5)	8.2%	9.0%	10%	12.4%	18.8%

Table 3. Cross-correlation between the maximum velocities of stack-of-stars and Cartesian 4D-Flow methods for 30-40% and 40-50% diameter narrowing phantoms. Good cross-correlation and reasonable nRMSE (normalized root-mean-square error) was observed for up to 2.5x undersampling.

Average velocities (z-direction) Cross-correlation (CC)	**Projections (undersampling factor)**				
	2500	2000 (1.25x)	1500 (1.7x)	1000 (2.5x)	500 (5x)
30-40% narrowing (n=2)	0.93±0.01	0.92±0.00	0.91±0.00	0.90±0.01	0.83±0.02
40-50% narrowing (n=2)	0.93±0.02	0.92±0.04	0.91±0.05	0.89±0.02	0.80±0.02
All (n=5)	0.949	0.938	0.936	0.928	0.858
nRMSE (n-5)	15.6%	15.3%	14.1%	13.9%	18.5%

Table 4. Cross-correlation between the average velocities of stack-of-stars and Cartesian 4D-Flow methods for 30-40% and 40-50% diameter narrowing phantoms. Good cross-correlation and reasonable nRMSE (normalized root-mean-square error) was observed for up to 2.5x undersampling.

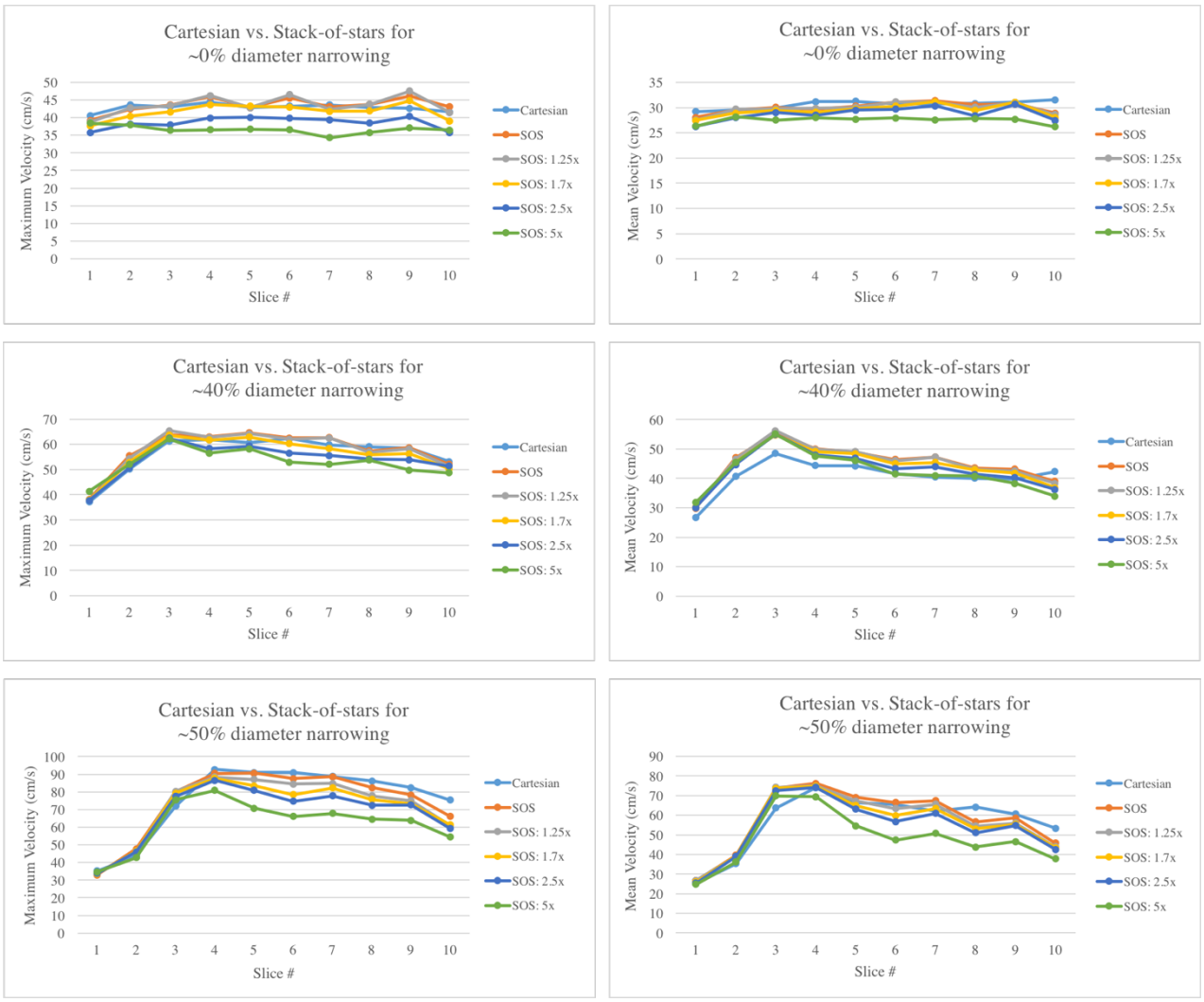

Figure 19. Example comparisons of Cartesian versus stack-of-stars peak and mean through-plane velocities 0%, ~40%, and ~50% diameter narrowing phantoms.

In the *in vivo* studies, total average Cartesian scan time was 35.46 ± 0.3 minutes. For stack-of-stars, 1200, 1000, and 800 imaging projections are equivalent to 1.5x, 1.8x, and 2.3x undersampling factors using Cartesian as a reference or approximately 23, 20, and 15 minutes scan time. **Figure 20** shows the example images of Cartesian and stack-of-stars methods in a

healthy subject. Average maximum through-plane velocity in all healthy volunteers was 15.6±3.6 cm/s, 14.7±4.1 cm/s, 16.2±6.2 cm/s and 16.2±5.4 cm/s for Cartesian, stack-of-stars with 1200, 1000, and 800 imaging projections, respectively. Cross-correlation of the peak through-plane velocities between Cartesian and stack-of-stars with 1200, 1000, and 800 imaging projections are 0.80, 0.77, and 0.70, respectively. **Figure 21** shows the Bland-Altman plots of the maximum through-plane velocities across all subjects between various stack-of-stars undersampling factors and Cartesian acquisition. A bias of 0.86, -0.66, and -0.63 was observed for 1200, 1000, and 800 projections, respectively

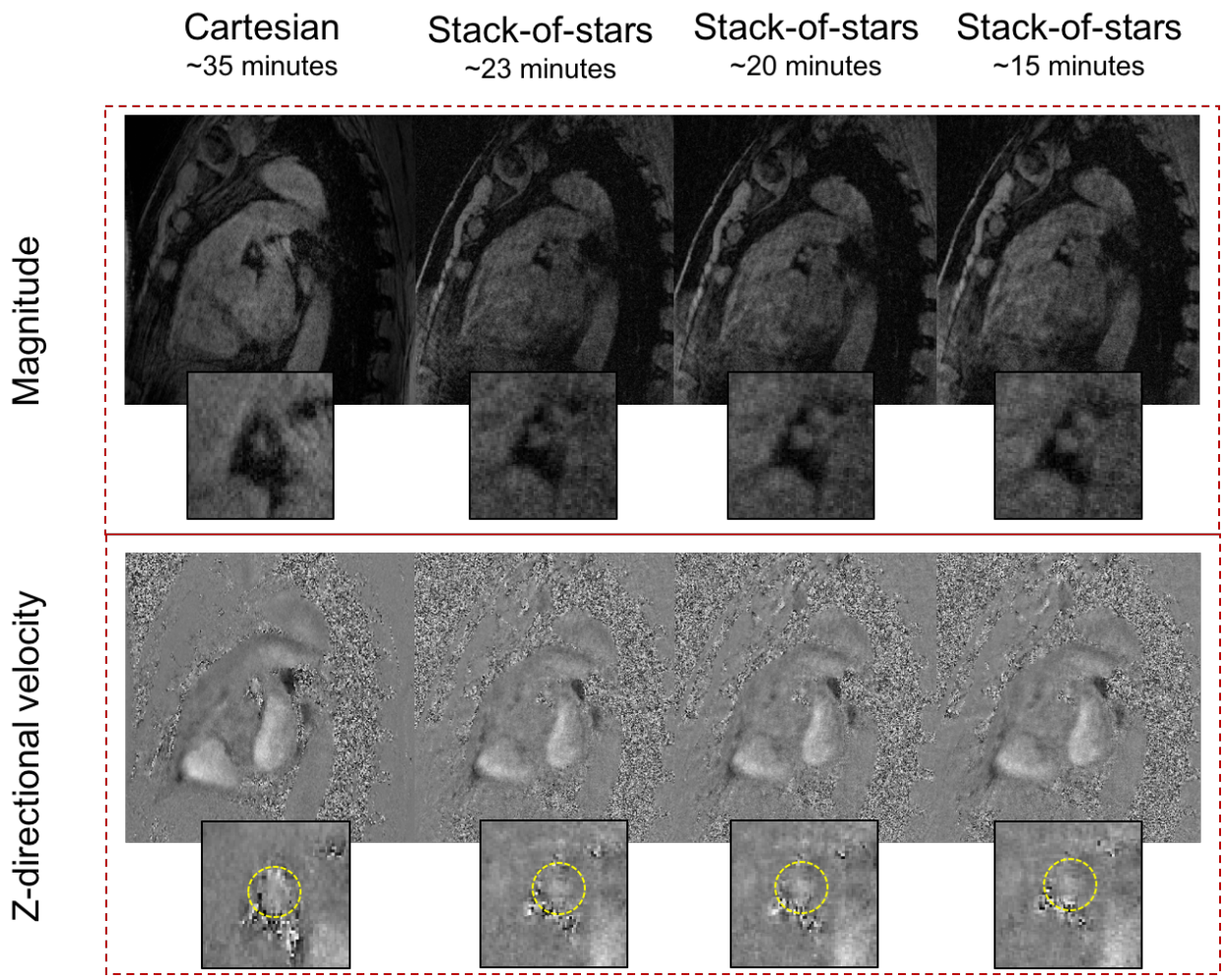

Figure 20. Example images comparing Cartesian versus various undersampled Stack-of-stars acquisitions in a healthy subject. Images with approximately 23, 20, and 15 minutes scan time are equivalent to 1.5x, 1.8x, and 2.3x undersampling, using a Cartesian acquisition with parallel imaging acceleration of 2 (~35 minutes scan time) as a reference. Good delineation of the coronary vessel was observed in the undersampled stack-of-stars magnitude images.

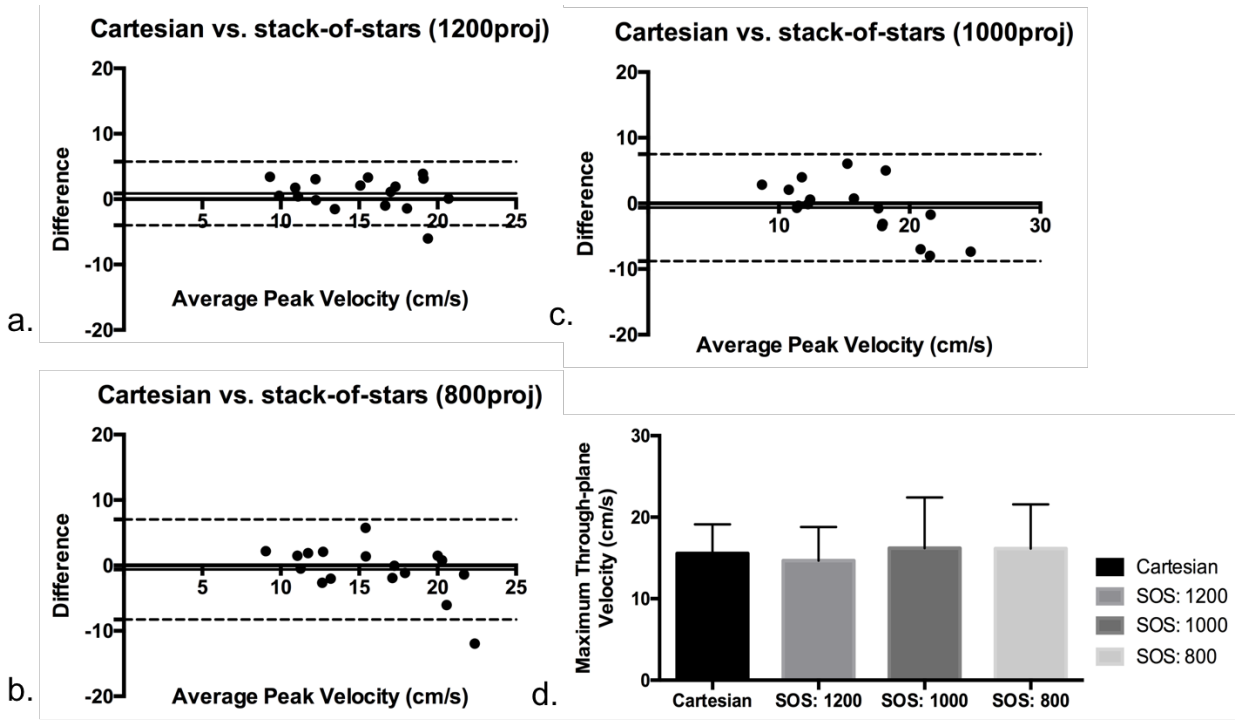

Figure 21. (a-c) Bland-Altman plots of peak through-plane velocities in all healthy subjects for Cartesian versus various undersampled stack-of-stars acquisitions. 1200, 1000, and 800 projections are equivalent to 1.5x, 1.8x, and 2.3x undersampling, or approximately 23, 20, and 15 minutes acquisition time for the stack-of-stars method, using a Cartesian acquisition (~35 minutes) as a reference. d. Peak through-plane velocity of Cartesian and various stack-of-stars undersampling factors. All p-values between Cartesian and various stack-of-stars undersampling factors were not significantly different ($p>0.05$).

6.4 Discussion

In this work, we have demonstrated the feasibility of a stack-of-stars 4D flow sequence with SENSE and compressed sensing reconstruction in the coronary arteries. The proposed method has the advantage of up to approximately 2-3 times undersampling (~10-20 mins)

compared to Cartesian acquisition (30-40 mins). The shorter scan time may allow for an easier adoption in the routine clinical procedures. In addition, could also be implemented as an add-on scan to other existing CMR protocols as a complementary diagnostic tool for the diagnosis of stable CAD. In the *in vitro* studies, the changes in velocity across various degrees of stenosis was observed in both stack-of-stars and Cartesian methods. Good peak velocity correlation was observed in both *in vitro* and *in vivo* studies between various undersampled stack-of-stars acquisitions and Cartesian acquisition.

More *in vivo* experiments in healthy coronary arteries are needed to further evaluate the performance of the method. Radial sampling is known to be robust to motion as each imaging line crosses the center of *k*-space during acquisition. A larger sample size could help further evaluate the potential advantage of radial sampling to motion. For 3D imaging, drastic changes in heart rate or breathing pattern within the 10 to 20 minutes acquisition time may corrupt the overall image quality. 2D radial acquisitions could be explored in the future to evaluate its robustness to motion and the feasible undersampling factor.

6.5 Conclusions

Our preliminary results showed the feasibility of stack-of-stars 4D Flow measurement in the coronary arteries. It has the potential to reduce scan time (2-3x) as compared to conventional Cartesian imaging. Larger healthy volunteer studies and *in vivo* studies involving patients with coronary artery disease are underway to evaluate the performance of the method.

CHAPTER 7 – Conclusions & Future directions

In this dissertation work, a new noninvasive diagnostic tool for the assessment of stable CAD was developed. The developed technique has the potential to serve as a complementary approach to current clinical noninvasive diagnostic tools, providing added information for better risk stratification and management of patients with stable CAD. Specifically, *chapter 3-6* described the noninvasive pressure gradient measurement framework using PC-MRI and Navier-stokes analysis, termed MR-iFR, and its potential for prediction of FFR or iFR in the coronary arteries. As the coronary arteries are relatively small, approximately 3 to 4 mm, a high spatial resolution PC-MRI sequence was used to ensure that adequate number of pixels were obtained for analysis. Due to cardiac and respiratory motion in the heart, coronary arteries tend to be difficult to image. To minimize motion, ECG-triggering to diastole and navigator-gating to end expiration were implemented in the PC-MRI data acquisition. With high spatial resolution comes the tradeoff of lower temporal resolution. To ensure minimal motion in each acquired cardiac phase, a view-sharing technique was implemented to share the k-space data between the neighboring cardiac phases. The resultant coronary velocity maps were then used in the Navier-stokes equations to obtain the pressure gradient across the vessel segment of interest.

The developed framework described in this dissertation was first evaluated for its feasibility in vitro (stenotic flow phantoms at various degrees of narrowing), using pressure transducer measured pressure gradient as a reference. The technique was then implemented and evaluated in healthy and diseased coronary arteries. For the in vitro studies, good repeatability of both velocity and pressure gradient measurements was observed. In addition, good correlation was observed using PC-MRI derived and pressure transducer measured pressure gradients. For the in vivo studies, good repeatability of coronary velocity maps was observed. In addition, good correlation was observed between the proposed noninvasive pressure gradient measurement

framework, MR-iFR, and the invasive FFR and iFR methods. The patient studies also showed high specificity and high negative predictive value, suggesting the potential of the proposed technique to serve as a gatekeeper for unnecessary invasive catheterization in patients with stable CAD.

To eventually translate the proposed technique for routine clinical use, further reduction in scan time and improvement in scan success rate is needed. In *chapter 3-5*, data collected in the in vitro and in vivo studies were also analyzed using z-directional coronary velocity maps only for Navier-stokes analysis. Good correlation was observed in the in vitro studies and in vivo patient studies, suggesting the possibility of using z-directional coronary velocity maps only in the overall framework. The use of z-directional coronary velocity may allow for an overall 50% scan time reduction; however, the method may not apply to all coronary vessels as some vessels are more tortuous than others. In addition, in *chapter 6,* an improved PC-MRI acquisition approach using stack-of-stars sampling and compressed sensing reconstruction was implemented. The proposed stack-of-stars approach showed good correlation to reference Cartesian acquisition with two to three times scan time reduction, allowing a decrease in scan time from approximately 40 minutes to 15 minutes.

In short, this dissertation demonstrated the feasibility of the proposed noninvasive pressure gradient measurement framework in stenotic phantoms, healthy subjects and a small cohort of stable CAD patients. The preliminary comparison with invasive FFR and iFR in patients showed the potential of the proposed technique to serve as a gatekeeper for more effective risk stratification and management of patients who would most likely benefit from invasive catheterization.

The emerging noninvasive pressure measurement method using coronary CTA and computational fluid dynamics, FFR_{CT}, has shown to decrease the rate of invasive catheterization and overall cost when compared to usual care, suggesting that it's a promising technique for the noninvasive diagnosis of patients with stable angina(14,15,92). However, the technique requires exposure to ionizing radiation, uses an anatomical model to simulate the hemodynamic behaviors in the coronary arteries, and is prone to blooming artifacts caused by densely calcified plaques which could reduce the accuracy of the overall technique. In the FFT_{CT} NXT (analysis of coronary blood flow using CT angiography: next steps) trial, approximately 13% of coronary CTA data were discarded due to image artifacts such as motion and misregistration, image noise, calcium blooming, and low contrast to noise ratio (107). As shown in a patient case in *chapter 4,* MR-iFR correctly identified the severity of the coronary lesion in a patient with heavy calcification, which was wrongly determined by coronary CTA. The proposed MR-iFR method could potentially be performed in patients, in whom FFR_{CT} could be inaccurate due to blooming artifacts, and provide added value to overall patient management. In addition, MRI has the advantage of no ionizing radiation where longitudinal monitoring of patients with potential risk of CAD could be performed. Furthermore, in coronary CTA, injection of iodine contrast is required during the scan to ensure sufficient blood to tissue contrast of the coronary tree. Recent studies have reported that a significant portion of patients with chronic kidney disease suffers from cardiovascular disease (1 in 3 CKD patients has CVD)(108), requiring a contrast-free approach. It was mentioned by Briasoulis et al. that the risk of CAD increases exponentially with declining kidney function where CKD patients are more likely to die of CVD than to progress to end stage kidney disease(109,110). The proposed framework although used Gadolinium contrast for coronary MRA image acquisition, a non-contrast coronary MRA protocol could be achieved

for coronary localization where no exogenous contrast agents are needed. The non-contrast approach could be especially advantageous for patients with chronic kidney disease or patients who are allergic to the contrast agents or patients who simply prefer no contrast injection.

The proposed MR-iFR technique could be combined with other noninvasive MR tests where cardiac anatomy and function could be obtained in one single imaging session, achieving a one-stop-shop cardiac examination. On a per vessel analysis, MR-iFR could be added to MR plaque characterization (28,81-83,94) and MRA where the degree of coronary stenosis severity, various coronary plaque composition, and the coronary hemodynamic factors could be obtained in one imaging session for a noninvasive comprehensive coronary exam. On a vessel to myocardium analysis, the proposed MR-iFR method could be especially beneficial to serve as an integrated approach with MR myocardial perfusion imaging. MR myocardial perfusion imaging has shown to be non-inferior to invasive angiography supported by FFR as a noninvasive management strategy for patients with stable CAD (39,84,93). A combined approach could potentially help identify ischemia from both the vessel lesion itself and the reduced flow to the myocardium.

In the pilot patient study presented in this dissertation, the functionally nonsignificant patient group had coronary stenosis range from 30% to 70% shown in ICA, where treatment was deferred in this patient group. The proposed framework was able to detect the functionally nonsignificant patients with high specificity using either FFR or iFR as the reference, showing the feasibility of the proposed method in potentially limiting the number of unnecessary invasive procedures. The current study is limited by the small sample size of the functionally significant coronary lesions. A larger patient study with more positive invasive FFR and iFR values are needed to further investigate the accuracy of the approach. More patient studies could also allow

for the identification of an optimal MR-iFR cut-off value based on the tradeoffs of sensitivity and specificity.

In current clinical practice, coronary lesions with ≥ 70% diameter stenosis (≥ 50% in the left main) are treated with either PCI or CABG. In coronary lesions with < 70% diameter stenosis (< 50% in the left main), medical therapy and continuous monitoring is suggested for the patient. This dissertation focused on the patient group with ≤ 70% diameter stenosis, however, in patients with smaller reference coronary diameter, the proposed method may not have sufficient spatial resolution to accurately assess the pressure gradient. For example, if we consider an average of 50% diameter stenosis in a 3-4mm diameter coronary segment, approximately 3-4 residual pixels remain if a 0.5x0.5 mm^2 in-plane resolution is used. Studies by Casas et al have shown that a ΔP underestimation of up to 5.8% average difference may occur with an approximately 3 voxels remain in the x and y directions (111). Therefore, > 50% diameter stenosis in smaller reference coronary diameters may lead to pressure gradient errors due to the limited number of pixels across the remaining coronary lumen and a higher spatial resolution is necessary. However, since ΔP_{MR} was shown to increase exponentially with increase in % DS, in a clinical setting, the estimated ΔP_{MR} for a functionally significant stenotic lesion may still remain above the prescribed cut-off threshold despite the potential errors. In addition, in current clinical practice with existing non-invasive methods, approximately 45% of patients who undergo invasive catheterization has a < 50% diameter stenosis, who didn't need the invasive procedures. The proposed method could potentially defer that 45% of patients from the invasive catheterization lab, which is still valuable in clinical practice. Nevertheless, to better understand the accuracy and robustness of the technique, future technical development in higher spatial resolution needs to be explored.

With improvement in spatial resolution, techniques such as iterative refinement could be implemented to obtain a pressure difference map (62) across the coronary artery and viscosity terms that were ignored in this study could be incorporated. In addition, in the current study, the integration path was defined by connecting the maximum velocity pixels in consecutive cross-sections to exploit high velocity to noise ratio. However, integration along a streamline (path parallel to the velocity field at a single instant in time) or pathline (path of particles as they move through space over time) and its effect on the accuracy of the MR-iFR measurements need to be explored. In addition, in situations of higher orders of fluid motion such as turbulence, higher spatial resolution may help better determine the non-turbulent flow stream (i.e. velocity jet) to avoid potential error caused by the dephased pixels due to turbulence. As the focus of the proposed technique is in stenosis with < 70% diameter, the effect of turbulence should be small as discussed by Nosovitsky et al. in a simulation study that the effect of turbulence in the velocity vectors is small for up to 75% stenosis in the coronary arteries (59). Furthermore, higher spatial resolution may allow for imaging of the more distal coronary segment to achieve imaging of the entire coronary tree.

To achieve higher spatial resolution, further technical improvements could be explored. As in MRI, there's a direct tradeoff between spatial resolution and scan time. If one could achieve a higher undersampling factor with sufficient image quality, a higher resolution could be achieved within a reasonable scan time. Smith et al. have explored the concept of reduced filed-of-view (rFOV) MRI with outer volume suppression (OVS) to improve sampling efficiency and reduce scan time(112). OVS is a magnetization preparation method used to suppress the signal outside of a region of interest. In case of a radial acquisition as discussed in *chapter 6*, the implementation of OVS could suppress the signal from peripheral regions (i.e. chest wall and

back). These signals would otherwise contribute to streaking artifacts in the FOV if drastic k-space undersampling is used. By using OVS, a higher undersampling rate may be achieved with sufficient image quality. In addition, rFOV could also be used to achieve shorter scan time or increase spatial resolution since the main region of interest is the coronary arteries which contributes only to a small portion of the overall FOV. In MRI, an increase in spatial resolution comes with a tradeoff of decreased SNR. In case where insufficient SNR is observed, an alternative approach is to use contrast enhanced imaging to achieve sufficient SNR for analysis.

In cardiac imaging, especially in the coronary arteries where vessel size is relatively small, any unexpected cardiac and respiratory motion may affect the overall image quality. In the proposed approach, two imaging lines per velocity encoding were collected per cardiac phase, giving a temporal resolution of approximately 70 ms, resulting in a total acquisition of approximately 140 ms within diastole per heartbeat. Although previous study in coronary flow velocity by Keegan et al. have shown that coronary velocity in diastole is relatively constant within a 150ms window (82), minor cardiac motion may occur within diastole for subjects with short quiescent periods. Future technical developments could further explore a MR reconstruction method such as highly constrained projection reconstruction (HYPR) technique to decrease the temporal resolution, hence, restrict acquisition to a smaller window to possibly achieve reduced cardiac motion. The HYPR reconstruction is based on two components, a weighting image at each time frame and a composite image formed by all time frames. HYPR has the advantage of preserving the SNR and spatial resolution from the fully sampled composite image at each time frame, therefore, provides adequate image quality for each temporal dynamic information. Increase in temporal resolution also has the advantage to allow acquisition during the iFR wave-free period only instead of the entire diastolic period or may allow acquisition

under stress conditions where FFR could potentially be calculated. In addition, higher temporal resolution may allow us to better capture the peak flow velocity period in diastole.

In summary, the development of a truly noninvasive method for the assessment of the functional significance of a coronary lesion is extremely impactful in the current clinical management of stable CAD patients. Current noninvasive clinical diagnostic tools tend to have poor diagnostic yield of invasive catheterization, where approximately 50% of patients undergo unnecessary invasive procedures. The unnecessary invasive procedures may lead to additional risks for patients, higher overall costs, and patient discomfort. These patients should be more carefully assessed during their noninvasive diagnostic work-up for the need of invasive catheterization. The proposed framework in this dissertation showed the feasibility of using an MR derived functional index, MR-iFR, for the assessment of stable CAD. This method may potentially help improve the diagnostic yield of invasive catheterization and help clinicians better identify patients with or without suspected stable CAD and consequently determine the optimal patient management.

REFERENCES

1. Calderon P Heart Disease and Stroke Statistics 2017 At-a-Glance 2017:1–5.

2. Benjamin EJ, Blaha MJ, Chiuve SE, et al. Heart Disease and Stroke Statistics—2017 Update: A Report From the American Heart Association. Circulation 2017;135(10):e146–e603. Doi: 10.1161/CIR.0000000000000485.

3. Lloyd-Jones D, Adams RJ, Brown TM, et al. Heart Disease and Stroke Statistics--2010 Update: A Report From the American Heart Association. Circulation 2010;121(7):e46–e215. Doi: 10.1161/CIRCULATIONAHA.109.192667.

4. Fihn SD, Gardin JM, Abrams J, et al. 2012 ACCF/AHA/ACP/AATS/PCNA/SCAI/STS Guideline for the Diagnosis and Management of Patients With Stable Ischemic Heart Disease: A Report of the American College of Cardiology Foundation/American Heart Association Task Force on Practice Guidelines, and the American College of Physicians, American Association for Thoracic Surgery, Preventive Cardiovascular Nurses Association, Society for Cardiovascular Angiography and Interventions, and Society of Thoracic Surgeons. Circulation 2012;126(25):e354–e471. Doi: 10.1161/CIR.0b013e318277d6a0.

5. Gibbons RJ ACC/AHA 2002 Guideline Update for the Management of Patients With Chronic Stable Angina--Summary Article: A Report of the American College of Cardiology/American Heart Association Task Force on Practice Guidelines (Committee on the Management of Patients With Chronic Stable Angina). Circulation 2003;107(1):149–58. Doi: 10.1161/01.CIR.0000047041.66447.29.

6. Cheitlin MD ACC/AHA/ASE 2003 Guideline Update for the Clinical Application of Echocardiography: Summary Article: A Report of the American College of Cardiology/American Heart Association Task Force on Practice Guidelines (ACC/AHA/ASE Committee to Update the 1997 Guidelines for the Clinical Application of Echocardiography). Circulation 2003;108(9):1146–62. Doi: 10.1161/01.CIR.0000073597.57414.A9.

7. Fihn SD, Blankenship JC, Alexander KP, et al. 2014 ACC/AHA/AATS/PCNA/SCAI/STS focused update of the guideline for the diagnosis and management of patients with stable ischemic heart disease: a report of the American College of Cardiology/American Heart Association Task Force on Practice Guidelines, and the American Association for Thoracic Surgery, Preventive Cardiovascular Nurses Association, Society for Cardiovascular Angiography and Interventions, and Society of Thoracic Surgeons. Circulation 2014:1749–67. Doi: 10.1161/CIR.0000000000000095/-/DC1.

8. Tonino PAL, De Bruyne B, Pijls NHJ, et al. Fractional Flow Reserve versus Angiography for Guiding Percutaneous Coronary Intervention 2009:1–12.

9. Götberg M, Christiansen EH, Gudmundsdottir IJ, et al. Instantaneous Wave-free Ratio versus Fractional Flow Reserve to Guide PCI. N Engl J Med 2017:NEJMoa1616540. Doi: 10.1056/NEJMoa1616540.

10. Davies JE, Sen S, Dehbi H-M, et al. Use of the Instantaneous Wave-free Ratio or Fractional Flow Reserve in PCI. N Engl J Med 2017:NEJMoa1700445. Doi: 10.1056/NEJMoa1700445.

11. Patel MR, Peterson ED, Dai D, et al. Low Diagnostic Yield of Elective Coronary Angiography. N Engl J Med 2010;362(10):886–95. Doi: 10.1056/NEJMoa0907272.

12. Patel MR, Dai D, Hernandez AF, et al. Prevalence and predictors of nonobstructive coronaryartery disease identified with coronary angiography incontemporary clinical practice 2014;167(6):846–852.e2. Doi: 10.1016/j.ahj.2014.03.001.

13. Tonino PAL, Fearon WF, De Bruyne B, et al. Angiographic Versus Functional Severity ofCoronary Artery Stenoses in the FAME Study. Jacc 2010;55(25):2816–21. Doi: 10.1016/j.jacc.2009.11.096.

14. Douglas PS, De Bruyne B, Pontone G, et al. 1-Year Outcomes of FFR_{CT}-Guided Care in Patients With Suspected Coronary Disease: The PLATFORM Study. Jacc 2016;68(5):435–45. Doi: 10.1016/j.jacc.2016.05.057.

15. Pontone G, Patel MR, Hlatky MA, et al. Rationale and design of the Prospective LongitudinAl Trial of FFR. American Heart Journal 2015;170(3):438–44. Doi: 10.1016/j.ahj.2015.06.002.

16. Guyton AC textbook of medical physiology (a c guyton - elsevier, 2006 11th ed) 2005:1–1150.

17. Pijls NH, De Bruyne B Coronary Pressure. vol. 195. 2nd ed. Springer Netherlands; 2013.

18. ECKENHOFF JE, HAFKENSCHIEL JH Cardiac oxygen metabolism and control of the coronary circulation. Am J Physiol 1947;149(3):634–49.

19. Gould KL, Lipscomb K, Hamilton GW Physiologic basis for assessing critical coronary stenosis. Instantaneous flow response and regional distribution during coronary hyperemia as measures of coronary flow reserve. Am J Cardiol 1974;33(1):87–94.

20. Collins P Coronary flow reserve. Br Heart J 1993;69(4):279–81.

21. Libby P Pathophysiology of Coronary Artery Disease. Circulation 2005;111(25):3481–8. Doi: 10.1161/CIRCULATIONAHA.105.537878.

22. Cassar A, Holmes DR Jr, Rihal CS, Gersh BJ Chronic Coronary Artery Disease: Diagnosis and Management. Mayo Clinic Proceedings 2009;84(12):1130–46. Doi:

10.4065/mcp.2009.0391.

23. Ohman EM Chronic Stable Angina. N Engl J Med 2016;374(12):1167–76. Doi: 10.1056/NEJMcp1502240.

24. Fihn SD, Gardin JM, Abrams J, et al. 2012 ACCF/AHA/ACP/AATS/PCNA/SCAI/STS Guideline for the Diagnosis and Management of Patients With Stable Ischemic Heart Disease: Executive Summary. J Am Coll Cardiol 2012;60(24):2564–603. Doi: 10.1016/j.jacc.2012.07.012.

25. Pryor DB, Shaw L, McCants CB, et al. Value of the history and physical in identifying patients at increased risk for coronary artery disease. Ann Intern Med 1993;118(2):81–90.

26. France GMC, Germany USC, Germany SA, et al. 2013 ESC guidelines on the management of stable coronary artery disease. Eur Heart J 2013;34(38):2949–3003. Doi: 10.1093/eurheartj/eht296.

27. Mintz GS, Pichard AD, Kovach JA, et al. Impact of preintervention intravascular ultrasound imaging on transcatheter treatment strategies in coronary artery disease. Am J Cardiol 1994;73(7):423–30.

28. Xie Y, Kim Y-J, pang J, et al. Coronary Atherosclerosis T1-Weighed Characterization With Integrated Anatomical Reference. JACC: Cardiovascular Imaging 2016. Doi: 10.1016/j.jcmg.2016.06.014.

29. Miller DD, Donohue TJ, Younis LT, et al. Correlation of Pharmacological 99mTc-Sestamibi Myocardial Perfusion Imaging with Poststenotic Coronary Flow Reserve in Patients with Angiographically Intermediate Coronary Artery Stenoses. Circulation 1994;89(5):2150–60. Doi: 10.1161/01.CIR.89.5.2150.

30. Kern MJ, Donohue TJ, Aguirre FV, et al. Clinical Outcome of Deferring Angioplasty in Patients With Normal Translesional Pressure-Flow Velocity Measurements. Jacc 1995;25(1):178–87. Doi: 10.1016/0735-1097(94)00328-N.

31. Pijls NH, De Bruyne B, Peels K, et al. Measurement of fractional flow reserve to assess the functional severity of coronary-artery stenoses. N Engl J Med 1996;334(26):1703–8. Doi: 10.1056/NEJM199606273342604.

32. Pijls NH, Van Gelder B, Van der Voort P, et al. Fractional flow reserve. A useful index to evaluate the influence of an epicardial coronary stenosis on myocardial blood flow. Circulation 1995;92(11):3183–93.

33. De Bruyne B, Pijls NH, Bartunek J, et al. Fractional flow reserve in patients with prior myocardial infarction. Circulation 2001;104(2):157–62.

34. Bech GJ, De Bruyne B, Pijls NH, et al. Fractional flow reserve to determine the appropriateness of angioplasty in moderate coronary stenosis: a randomized trial. Circulation 2001;103(24):2928–34.

35. Pijls NHJ, van Schaardenburgh P, Manoharan G, et al. Percutaneous Coronary Intervention of Functionally Nonsignificant Stenosis. J Am Coll Cardiol 2007;49(21):2105–11. Doi: 10.1016/j.jacc.2007.01.087.

36. Economic evaluation of fractional flow reserve-guided percutaneous coronary intervention in patients with multivessel disease. 2010;122(24):2545–50. Doi: 10.1161/CIRCULATIONAHA.109.925396.

37. Sen S, Escaned J, Malik IS, et al. Development and validation of a new adenosine-independent index of stenosis severity from coronary wave-intensity analysis: results of the ADVISE (ADenosine Vasodilator Independent Stenosis Evaluation) study. J Am Coll Cardiol 2012;59(15):1392–402. Doi: 10.1016/j.jacc.2011.11.003.

38. Klocke FJ ACC/AHA/ASNC Guidelines for the Clinical Use of Cardiac Radionuclide Imaging--Executive Summary: A Report of the American College of Cardiology/American Heart Association Task Force on Practice Guidelines (ACC/AHA/ASNC Committee to Revise the 1995 Guidelines for the Clinical Use of Cardiac Radionuclide Imaging). Circulation 2003;108(11):1404–18. Doi: 10.1161/01.CIR.0000080946.42225.4D.

39. Nagel E MR-INFORM: Stress Perfusion Imaging to Guide the Management of Patients with Stable Coronary Artery Disease. American College of Cardiology Annual Scientific Session (ACC 2017) 2017:1–20.

40. Douglas PS, Pontone G, Hlatky MA, et al. Clinical outcomes of fractional flow reserve by computed tomographic angiography-guided diagnostic strategies vs. usual care in patients with suspected coronary artery disease: the prospective longitudinal trial of FFR CT: outcome and resource impacts study. Eur Heart J 2015;36(47):3359–67. Doi: 10.1093/eurheartj/ehv444.

41. Itu L, Rapaka S, Passerini T, et al. A machine-learning approach for computation of fractional flow reserve from coronary computed tomography. J Appl Physiol 2016;121(1):42–52. Doi: 10.1152/japplphysiol.00752.2015.

42. Impact of ischaemia and scar on the therapeutic benefit derived from myocardial revascularization vs. medical therapy among patients undergoing stress-rest myocardial perfusion scintigraphy 2011;32(8):1012–24. Doi: 10.1093/eurheartj/ehq500.

43. Comparison of the Short-Term Survival Benefit Associated With Revascularization Compared With Medical Therapy in Patients With No Prior Coronary Artery Disease Undergoing Stress Myocardial Perfusion Single Photon Emission Computed Tomography 2003;107(23):2900–7. Doi: 10.1161/01.CIR.0000072790.23090.41.

44. Continuing evolution of therapy for coronary artery disease. Initial results from the era of coronary angioplasty. 1994;89(5):2015–25. Doi: 10.1161/01.CIR.89.5.2015.

45. Optimal medical therapy with or without PCI for stable coronary disease 2007;356(15):1503–16. Doi: 10.1056/NEJMoa070829).

46. MD MRP, Calhoon JH, MACC GJDM, et al. ACC/AATS/AHA/ASE/ASNC/SCAI/SCCT/ STS 2017 Appropriate Use Criteria for Coronary Revascularization in Patients With Stable Ischemic Heart Disease. Jacc 2017:1–30. Doi: 10.1016/j.jacc.2017.02.001.

47. Bernstein MA, King KF, Zhou XJ Handbook of MRI Pulse Sequences. Elsevier; 2004.

48. Brown RW, Haacke EM, Cheng YCN, Thompson MR, Venkatesan R Magnetic Resonance Imaging. John Wiley & Sons; 2014.

49. Nishimura DG Principles of magnetic resonance imaging. 1996.

50. Liang Z-P, Lauterbur PC Principles of Magnetic Resonance Imaging. Wiley-IEEE Press; 1999.

51. Currie PJ, Seward JB, Reeder GS, et al. Continuous-wave Doppler echocardiographic assessment of severity of calcific aortic stenosis: a simultaneous Doppler-catheter correlative study in 100 adult patients. Circulation 1985;71(6):1162–9.

52. Cohn JN Surrogate Markers for Cardiovascular Disease: Functional Markers. Circulation 2004;109(25_suppl_1):IV–31–IV–46. Doi: 10.1161/01.CIR.0000133442.99186.39.

53. Anavekar NS, Oh JK Doppler echocardiography: A contemporary review. Journal of Cardiology 2009;54(3):347–58. Doi: 10.1016/j.jjcc.2009.10.001.

54. Heys JJ, Holyoak N, Calleja AM, Belohlavek M, Chaliki HP Revisiting the simplified bernoulli equation. Open Biomed Eng J 2010;4:123–8. Doi: 10.2174/1874120701004010123.

55. Assessment of coronary flow reserve with fast cine phase contrast magnetic resonance imaging: Comparison with measurement by Doppler guide wire 1999;10(4):563–8. Doi: 10.1002/(SICI)1522-2586(199910)10:4<563::AID-JMRI9>3.0.CO;2-H.

56. Assessment of coronary flow reserve using fast velocity-encoded cine MR imaging: validation study using positron emission tomography. 2000;175(4):1029–33. Doi: 10.2214/ajr.175.4.1751029.

57. 4D flow MRI 2012;36(5):1015–36. Doi: 10.1002/jmri.23632.

58. Yoganathan AP, Cape EG, Sung HW, Williams FP, Jimoh A Review of hydrodynamic principles for the cardiologist: applications to the study of blood flow and jets by imaging techniques. Jacc 1988;12(5):1344–53.

59. Nosovitsky VA, Ilegbusi OJ, Jiang J, Stone PH, Feldman CL Effects of curvature and stenosis-like narrowing on wall shear stress in a coronary artery model with phasic flow. Comput Biomed Res 1997;30(1):61–82.

60. Liu B, Tang D Computer simulations of atherosclerotic plaque growth in coronary arteries. Mol Cell Biomech 2010;7(4):193–202.

61. Johnston BM, Johnston PR, Corney S, Kilpatrick D Non-Newtonian blood flow in human right coronary arteries: transient simulations. J Biomech 2006;39(6):1116–28. Doi: 10.1016/j.jbiomech.2005.01.034.

62. Bock J, Frydrychowicz A, Lorenz R, et al. In vivo noninvasive 4D pressure difference mapping in the human aorta: phantom comparison and application in healthy volunteers and patients. Magn Reson Med 2011;66(4):1079–88. Doi: 10.1002/mrm.22907.

63. Thompson RB, McVeigh ER Fast measurement of intracardiac pressure differences with 2D breath-hold phase-contrast MRI. Magn Reson Med 2003;49(6):1056–66. Doi: 10.1002/mrm.10486.

64. Bley TA, Johnson KM, François CJ, et al. Noninvasive assessment of transstenotic pressure gradients in porcine renal artery stenoses by using vastly undersampled phase-contrast MR angiography. Radiology 2011;261(1):266–73. Doi: 10.1148/radiol.11101175.

65. Yang GZ, Kilner PJ, Wood NB, Underwood SR, Firmin DN Computation of flow pressure fields from magnetic resonance velocity mapping. Magn Reson Med 1996;36(4):520–6.

66. Ebbers T, Wigström L, Bolger AF, Engvall J, Karlsson M Estimation of relative cardiovascular pressures using time-resolved three-dimensional phase contrast MRI. Magn Reson Med 2001;45(5):872–9.

67. Estimation of relative cardiovascular pressures using time-resolved three-dimensional phase contrast MRI 2001;45(5):872–9. Doi: 10.1002/mrm.1116.

68. Ebbers T, Wigström L, Bolger AF, Wranne B, Karlsson M Noninvasive measurement of time-varying three-dimensional relative pressure fields within the human heart. J Biomech Eng 2002;124(3):288–93.

69. Nagao T, Yoshida K, Okada K, Miyazaki S, Ueguchi T, Murase K Development of a noninvasive method to measure intravascular and intracardiac pressure differences using magnetic resonance imaging. Magn Reson Med Sci 2008;7(3):113–22.

70. Tasu JP, Mousseaux E, Delouche A, Oddou C, Jolivet O, Bittoun J Estimation of pressure gradients in pulsatile flow from magnetic resonance acceleration measurements. Magn Reson Med 2000;44(1):66–72.

71. Three-dimensional, time-resolved (4D) relative pressure mapping using magnetic resonance imaging 2000;12(2):321–9. Doi: 10.1002/1522-2586(200008)12:2<321::AID-JMRI15>3.0.CO;2-2.

72. Turk AS, Johnson KM, Lum D, et al. Physiologic and anatomic assessment of a canine carotid artery stenosis model utilizing phase contrast with vastly undersampled isotropic projection imaging. AJNR Am J Neuroradiol 2007;28(1):111–5.

73. Lum DP, Johnson KM, Paul RK, et al. Transstenotic Pressure Gradients: Measurement in Swine—Retrospectively ECG-gated 3D Phase-Contrast MR Angiography versus Endovascular Pressure-sensing Guidewires 1. Radiology 2007;245(3):751–60. Doi: 10.1148/radiol.2453061946.

74. Miyati T, Mase M, Kasai H, et al. Noninvasive MRI assessment of intracranial compliance in idiopathic normal pressure hydrocephalus. J Magn Reson Imaging 2007;26(2):274–8. Doi: 10.1002/jmri.20999.

75. Moftakhar R, Aagaard-Kienitz B, Johnson K, et al. Noninvasive measurement of intra-aneurysmal pressure and flow pattern using phase contrast with vastly undersampled isotropic projection imaging. AJNR Am J Neuroradiol 2007;28(9):1710–4. Doi: 10.3174/ajnr.A0648.

76. Pelc NJ, Bernstein MA, Shimakawa A, Glover GH Encoding strategies for three-direction phase-contrast MR imaging of flow. J Magn Reson Imaging 1991;1(4):405–13.

77. Lorenz R, Bock J, Snyder J, Korvink JG, Jung BA, Markl M Influence of eddy current, Maxwell and gradient field corrections on 3D flow visualization of 3D CINE PC-MRI data. Magn Reson Med 2014;72(1):33–40. Doi: 10.1002/mrm.24885.

78. Bock J, Kreher BW, Hennig J, Markl M Optimized pre-processing of time-resolved 2D and 3D phase contrast MRI data. 2007.

79. Tyszka JM, Laidlaw DH, Asa JW, Silverman JM Three-dimensional, time-resolved (4D) relative pressure mapping using magnetic resonance imaging. J Magn Reson Imaging 2000;12(2):321–9.

80. Deng Z, Xie G, He Y, et al. Pressure Gradient Measurement in the Coronary Artery Using View-Sharing (VS) 4D PC-MRI: Towards Noninvaisve Quantification of Fractional Flow Reserve. International Society of Magnetic Resonance Imaging in Medicine (ISMRM Annual Meeting) 2014;(22):1–1.

81. Middione MJ, Ennis DB Chemical shift-induced phase errors in phase-contrast MRI. Magn Reson Med 2013;69(2):391–401. Doi: 10.1002/mrm.24262.

82. Keegan J, Raphael CE, Parker K, et al. Validation of high temporal resolution spiral phase velocity mapping of temporal patterns of left and right coronary artery blood flow against Doppler guidewire. Journal of Cardiovascular Magnetic Resonance : Official Journal of the Society for Cardiovascular Magnetic Resonance 2015;17(1):85. Doi: 10.1186/s12968-015-0189-y.

83. Williams B, Lacy PS, Yan P, Hwee CN, Liang C, Ting CM Development and Validation of aNovel Method to Derive Central AorticSystolic Pressure From the Radial Pressure Waveform Using an N-Point Moving Average Method. Jacc 2011;57(8):951–61. Doi: 10.1016/j.jacc.2010.09.054.

84. Pijls NHJ, Fearon WF, Tonino PAL, et al. Fractional flow reserve versus angiography for guiding percutaneous coronary intervention in patients with multivessel coronary artery disease: 2-year follow-up of the FAME (Fractional Flow Reserve Versus Angiography for Multivessel Evaluation) study. J Am Coll Cardiol 2010;56(3):177–84. Doi: 10.1016/j.jacc.2010.04.012.

85. Schuijf JD, Shaw LJ, Wijns W, et al. Cardiac imaging in coronary artery disease: differing modalities. Heart 2005;91(8):1110–7. Doi: 10.1136/hrt.2005.061408.

86. Kim C, Kwok YS, Heagerty P, Redberg R Pharmacologic stress testing for coronary disease diagnosis: A meta-analysis. American Heart Journal 2001;142(6):934–44. Doi: 10.1067/mhj.2001.119761.

87. Klocke FJ ACC/AHA/ASNC Guidelines for the Clinical Use of Cardiac Radionuclide Imaging--Executive Summary: A Report of the American College of Cardiology/American Heart Association Task Force on Practice Guidelines (ACC/AHA/ASNC Committee to Revise the 1995 Guidelines for the Clinical Use of Cardiac Radionuclide Imaging). Circulation 2003;108(11):1404–18. Doi: 10.1161/01.CIR.0000080946.42225.4D.

88. Deng Z, pang J, Yang W, et al. Four-dimensional MRI using three-dimensional radial sampling with respiratory self-gating to characterize temporal phase-resolved respiratory motion in the abdomen. Magn Reson Med 2015;75(4):1574–85. Doi: 10.1002/mrm.25753.

89. Tonino PAL, De Bruyne B, Pijls NHJ, et al. Fractional flow reserve versus angiography for guiding percutaneous coronary intervention. N Engl J Med 2009;360(3):213–24. Doi: 10.1056/NEJMoa0807611.

90. Fearon WF, Shilane D, Pijls NHJ, et al. Cost-Effectiveness of Percutaneous Coronary Intervention in Patients With Stable Coronary Artery Disease and Abnormal Fractional Flow Reserve. Circulation 2013;128(12):1335–40. Doi:

10.1161/CIRCULATIONAHA.113.003059.

91. West R Complications of diagnostic cardiac catheterisation: results from a confidential inquiry into cardiac catheter complications. Heart 2005;92(6):810–4. Doi: 10.1136/hrt.2005.073890.

92. Hlatky MA, De Bruyne B, Pontone G, et al. Quality-of-Life and Economic Outcomes of Assessing Fractional Flow Reserve With Computed Tomography Angiography. Jacc 2015;66(21):2315–23. Doi: 10.1016/j.jacc.2015.09.051.

93. Hussain ST, Paul M, Plein S, et al. Design and rationale of the MR-INFORM study: stress perfusion cardiovascular magnetic resonance imaging to guide the management of patients with stable coronary artery disease. Journal of Cardiovascular Magnetic Resonance : Official Journal of the Society for Cardiovascular Magnetic Resonance 2012;14:65. Doi: 10.1186/1532-429X-14-65.

94. Noguchi T, Kawasaki T, Tanaka A, et al. High-Intensity Signals in Coronary Plaques on Noncontrast T1-WeightedMagnetic Resonance Imaging as aNovel Determinant of Coronary Events. Jacc 2014;63(10):989–99. Doi: 10.1016/j.jacc.2013.11.034.

95. Gu T, Korosec FR, Block WF, et al. PC VIPR: a high-speed 3D phase-contrast method for flow quantification and high-resolution angiography. AJNR Am J Neuroradiol 2005;26(4):743–9.

96. Kecskemeti S, Johnson K, Wu Y, Mistretta C, Turski P, Wieben O High resolution three-dimensional cine phase contrast MRI of small intracranial aneurysms using a stack of stars k-space trajectory. J Magn Reson Imaging 2011;35(3):518–27. Doi: 10.1002/jmri.23501.

97. Thunberg P, Karlsson M, Wigström L Accuracy and reproducibility in phase contrast imaging using SENSE. Magn Reson Med 2003;50(5):1061–8. Doi: 10.1007/BF02668182.

98. Baltes C, Kozerke S, Hansen MS, Pruessmann KP, Tsao J, Boesiger P Accelerating cine phase-contrast flow measurements usingk-t BLAST andk-t SENSE. Magn Reson Med 2005;54(6):1430–8. Doi: 10.1002/mrm.20730.

99. Schnell S, Markl M, Entezari P, et al. k-tGRAPPA accelerated four-dimensional flow MRI in the aorta: Effect on scan time, image quality, and quantification of flow and wall shear stress. Magn Reson Med 2013;72(2):522–33. Doi: 10.1002/mrm.21477.

100. Knobloch V, Boesiger P, Kozerke S Sparsity transform k-t principal component analysis for accelerating cine three-dimensional flow measurements. Magn Reson Med 2012;70(1):53–63. Doi: 10.1002/mrm.20734.

101. Hsiao A, Lustig M, Alley MT, et al. Rapid Pediatric Cardiac Assessment of Flow and

Ventricular Volume With Compressed Sensing Parallel Imaging Volumetric Cine Phase-Contrast MRI. AJR Am J Roentgenol 2012;198(3):W250–9. Doi: 10.2214/AJR.11.6969.

102. Winkelmann S, Schaeffter T, Koehler T, Eggers H, Doessel O An Optimal Radial Profile Order Based on the Golden Ratio for Time-Resolved MRI. IEEE Trans Med Imaging n.d.;26(1):68–76. Doi: 10.1109/TMI.2006.885337.

103. Chan RW, Ramsay EA, Cheung EY, Plewes DB The influence of radial undersampling schemes on compressed sensing reconstruction in breast MRI. Magn Reson Med 2011;67(2):363–77. Doi: 10.1073/pnas.1733835100.

104. Rasche V, de Boer RW, Holz D, Proksa R Continuous radial data acquisition for dynamic MRI. Magn Reson Med 1995;34(5):754–61.

105. Buehrer M, Pruessmann KP, Boesiger P, Kozerke S Array compression for MRI with large coil arrays. Magn Reson Med 2007;57(6):1131–9. Doi: 10.1002/mrm.21237.

106. Feng L, Grimm R, Block KT, et al. Golden-angle radial sparse parallel MRI: Combination of compressed sensing, parallel imaging, and golden-angle radial sampling for fast and flexible dynamic volumetric MRI. Magn Reson Med 2013;72(3):707–17. Doi: 10.1002/mrm.24980.

107. Nørgaard BL, Leipsic J, Gaur S, et al. Diagnostic performance of noninvasive fractional flow reserve derived from coronary computed tomography angiography in suspected coronary artery disease: the NXT trial (Analysis of Coronary Blood Flow Using CT Angiography: Next Steps). J Am Coll Cardiol 2014;63(12):1145–55. Doi: 10.1016/j.jacc.2013.11.043.

108. Levin A Clinical Epidemiology of Cardiovascular Disease in Chronic Kidney Disease Prior to Dialysis 2003:1–5.

109. Subbiah AK, Chhabra YK, Mahajan S Cardiovascular disease in patients with chronic kidney disease: a neglected subgroup. Heart Asia 2016;8(2):56–61. Doi: 10.1136/heartasia-2016-010809.

110. Briasoulis A, Bakris GL Chronic Kidney Disease as a Coronary Artery Disease Risk Equivalent. Curr Cardiol Rep 2013;15(3):1296. Doi: 10.2174/157016112799304996.

111. Casas B, Lantz J, Dyverfeldt P, Ebbers T 4D Flow MRI-based pressure loss estimation in stenotic flows: Evaluation using numerical simulations. Magn Reson Med 2015;75(4):1808–21. Doi: 10.1002/mrm.25772.

112. Smith TB, Nayak KS Reduced field of view MRI with rapid, B1-robust outer volume suppression. Magn Reson Med 2011;67(5):1316–23. Doi: 10.1002/mrm.23116.